Title
Multiscale Modeling of Cardiac Arrhythmogenesis: Beyond the Trigger-Substrate Paradigm

Author
Liu, Michael B

Publication Date
2019

UNIVERSITY OF CALIFORNIA

Los Angeles

Multiscale Modeling of Cardiac Arrhythmogenesis:
Beyond the Trigger-Substrate Paradigm

A dissertation submitted in partial satisfaction of the
requirements for the degree of Doctor of Philosophy in
Molecular, Cellular, and Integrative Physiology

by

Michael Bon-Hao Liu

2019

ABSTRACT OF THE DISSERTATION

Multiscale Modeling of Cardiac Arrhythmogenesis:
Beyond the Trigger-Substrate Paradigm

by

Michael Bon-Hao Liu
Doctor of Philosophy in Molecular, Cellular, and Integrative Physiology
University of California, Los Angeles, 2019
Professor Zhilin Qu, Chair

Arrhythmias and sudden cardiac death (SCD) represent a leading cause of mortality in the US and worldwide. Currently, the most effective therapy for preventing SCD is the implantable cardioverter-defibrillator (ICD). ICDs however can only terminate arrhythmias after they have already occurred and have numerous severe side effects and poor cost-effectiveness. Therefore, the ideal anti-arrhythmic strategy is the prevention of arrhythmia initiation, or arrhythmogenesis, in the first place. Unfortunately, multiple clinical trials have demonstrated that many of the currently available anti-arrhythmic drugs are not generally effective in the prevention of ventricular arrhythmias, and in some cases may even be pro-arrhythmic unintuitively causing increased mortality. Thus, improved anti-arrhythmic strategies are needed which require improved mechanistic understanding of the arrhythmogenesis process.

Computational modeling is a powerful research tool, complementary to experimental and clinical studies, to study the underlying mechanisms of arrhythmias. In this dissertation, we use computer modeling and patch clamp experiments to investigate the spontaneous initiation of triggered and reentrant ventricular arrhythmias as related to delayed afterdepolarizations (DADs) and long QT syndrome (LQTS). We first describe a dynamical threshold for DAD-mediated triggered activity which is lower than the sodium channel threshold and manifests under conditions of hypokalemia and slow spontaneous calcium release. Next, we investigate the critical factors that determine DAD-mediated triggered activity formation in cardiac tissue. Thirdly, we study whether sub-threshold DADs can act as an arrhythmogenic trigger and find that DADs can generate both triggers and a reentry substrate simultaneously. And finally, we detail a novel common mechanism of arrhythmia initiation across different genotypes of LQTS called "R-from-T", which blurs the usual notions between arrhythmia trigger and substrate beyond the traditional paradigm. The mechanistic insights gained from these studies help inform the development of new arrhythmia prevention strategies.

The dissertation of Michael Bon-Hao Liu is approved.

James N. Weiss

Alan Garfinkel

Riccardo Olcese

Zhilin Qu, Committee Chair

University of California, Los Angeles

2019

This dissertation is dedicated to my loving parents

June & Duncan Liu

Table of Contents

Chapter 6: Conclusion **181**

Table of Figures

Acknowledgements

The PhD program can be a long winding journey and I could not have made it through without the support of many people in my life. The following acknowledgements are only a subset of these influential individuals.

First, I cannot have asked for a more nurturing and inspirational lab environment which all stems from the mentorship of my advisor Zhilin Qu. Zhilin's philosophy toward science and research have shaped my own. Zhilin is brilliant but humble, rigorous but visionary, and I cannot wait to someday follow in his footsteps.

The Qu lab wouldn't have been the same without my labmates Song Zhen and Julian Landaw as well, who were always there to bounce ideas off of each other, build our computer clusters together, and especially provide their critical thoughts on my work. Most enjoyable however, were our long discussions about life and science philosophy, often in Song's Tesla as he drove me home. Thank you both for making the Qu lab such a comfortable and stimulating place.

I'd also like to thank my wonderful committee members, James Weiss, Alan Garfinkel, and Riccardo Olcese, as well as all the other members of the UCLA Arrhythmia group for our lively discussions and weekly post-meeting lunches. We had such a unique interdisciplinary group and Wednesdays were never dull.

A special thank you to Kelsey Martin and Jim Tidball who at one of the most stressful times in my life encouraged me to keep going and supported me when I doubted myself. This PhD would not have even gotten off the ground without you and for that I am eternally grateful.

Thank you to all my UCLA MSTP classmates who’ve been along for these last wild 7 years. Our other medical school friends have graduated, matched, matched again, while we’ve still been in PhD-land and I couldn’t have stayed sane without your friendships. I’d especially like to thank Kate Masiuk and Shivani Thaker for always being available for our lunch time hangouts at Court of Sciences. No matter how things were going it was always comforting to have a familiar face to rant to or celebrate with. A special thank you also to Xavier Gaeta who has been my *de facto* mentor throughout my entire higher education. Always a couple years ahead, from undergrad at Stanford to UCLA MSTP, you’ve always been a comforting beacon of hope and advice, reminding me that people do make it through! I look forward to more future advice sessions over Pandemic Legacy 7.

Thank you to my fellow MCIP graduate school classmates. Even though I was one of those “weird dual-degree students” and you never saw me in any of the first year classes, you welcomed me to the MCIP family with open arms and it was only then when I finally felt part of the graduate school community. Special thanks to Saemi Park and Shuin Park for our tennis rallies, Sawtelle dinners, gummy bear breaks, and even Epik High concerts. I am so honored to have had friends like you to count on.

Science does not happen in a vacuum but instead is done by real people across the world. Throughout my PhD I’ve been blessed with numerous opportunities to travel and participate in many conferences. From Boston to Italy to Ventura to Korea, seeing science come alive not only as words on a page but as people having genuine discussions over coffee has been a transformative experience. As such, I need to thank the many scientific colleagues and friends I’ve met throughout my travels including Nele Vandersickel, Jenny Wang, Axel Loewe, Francis

Ortega, Bonnie Kit, and many others. I can't wait to continue seeing you at many Gordon conferences to come.

One of my committee members James Weiss once told me that everyone needs something for the mind, the body, and the soul. I'd like to thank my many friends who keep my life balanced with equally many hobbies. Whether we're flying airplanes, camping, traveling the world, or at a Stanford football game, thank you to Eric Lin, Ed Schmerling, Nathan Hobbs, Jane LePham, Marisa Landicho, Maxine Tang, Alex Ji, Kim Souza, Sita Sawyer, Emma Trotter, Kevin Cheng, Sophia Tsai, Devin Banerjee, Katie Ho, Christine Liang, Sean Chen, and many others. You've all enriched my life in more ways than I can count.

Thank you to my extended family members, from Taiwan to Utah to Chicago and the east coast. Thank you to my grandparents who are no longer with us, you are dearly missed. And a special thank you to my grandma Fongmei who celebrated her 90th birthday shortly after my thesis defense. You are an amazing woman and have shown me what true family love looks like. You have the most happy attitude to life and we couldn't be happier when we watch Jeopardy! and Wheel of Fortune with you. 謝謝奶奶!

Thank you to my amazing sister Lisa Liu. You've put up with my teasing and big brother antics for decades but I couldn't have imagined growing up without your company. From "Amagalala" to our Wii Sports music dance, we've always had our weird special connection. I am so proud of your own accomplishments and you finally get to be the "big sister" now as I look to your advice for the clinical years!

Thank you to the love of my life Rachel Liaw who has made my life more colorful than I ever thought possible. Whether it’s entrepreneurship or scientific research, I never tire of our passionate conversations as we navigate this world together. You inspire me to be the best person possible and I the thing I look forward to most every day is coming home to our happy home together.

Finally, thank you to my parents June and Duncan Liu. I consider myself to have had an amazingly loving and enriching childhood and I owe that all to my parents. The countless opportunities they provided me to explore my numerous interests made me the person I am today. Despite the stresses of modern day education, my parents allowed us to form our own passions and instilled in us a deep sense to pursue learning for learning’s sake and to always seek to improve oneself, which in large part is what led me to pursue a career in science. My parents have been an ever-present beacon of support and are my biggest role models in life.

Chapter 2 is a version of **Liu MB**, Ko CY, Song Z, Garfinkel A, Weiss JN, Qu Z. *A Dynamical Threshold for Cardiac Delayed Afterdepolarization-Mediated Triggered Activity.* Biophys J. 2016;111(11):2523-2533. (DOI: 10.1016/j.bpj.2016.10.009). This work was supported by National Heart, Lung and Blood Institute grant P01 HL078931, UCLA MCIP institutional training grant T32 GM065823, T32 HL07895, American Heart Association pre-doctoral fellowship 16PRE27610040, and the Laubisch and Kawata endowments.

Chapter 3 is a version of Ko CY, **Liu MB***, Song Z, Qu Z, Weiss JN. *Multiscale Determinants of Delayed Afterdepolarization Amplitude in Cardiac Tissue*. Biophys J. 2017;112(9):1949-1961. (DOI: 10.1016/j.bpj.2017.03.006). We thank Guillaume Calmettes, PhD and Alan Garfinkel, PhD for their help with the statistical analysis. We also thank Pauline Morand for myocyte preparation. This work was supported by NIH/NHLBI grants P01 HL078931 (to J.N.W.) and T32 GM065823 and T32 HL07895, American Heart Association Western States Affiliate Predoctoral Research Fellowship 10 PRE3030052, UCLA MSTP grant T32 GM008042, and the Laubisch and Kawata endowments.

Chapter 4 is a version of **Liu MB**, de Lange E, Garfinkel A, Weiss JN, Qu Z. *Delayed afterdepolarizations generate both triggers and a vulnerable substrate promoting reentry in cardiac tissue*. Heart Rhythm. 2015;12(10):2115-24. (DOI: 10.1016/j.hrthm.2015.06.019). This work was supported by NIH/National Heart, Lung and Blood Institute grants P01 HL078931, R01 HL110791, the UCLA MSTP grant T32 GM008042, the Swiss Foundation for Grants in Biology and Medicine grant PASMP3-127312, and the Laubisch and Kawata endowments.

Chapter 5 is unpublished work performed by Michael Liu, Nele Vandersickel, Alexander Panfilov, and Zhilin Qu. This work was supported by grants from National Institute of Health R01 HL134709, UCLA MSTP training grant T32 GM008042 and F30 HL132449.

Vita

Education

2007 – 2011	Bachelor of Science, Physics with Honors and Distinction Stanford University, Stanford, CA, USA
2011 – 2012	Master of Science, Bioengineering Stanford University, Stanford, CA, USA
2012 – present	Medical Scientist Training Program (MSTP) University of California, Los Angeles, CA, USA

Publications

Song Z, **Liu MB**, Qu Z. ***Transverse tubular network structures in the genesis of intracellular calcium alternans and triggered activity in cardiac cells.*** J Mol Cell Cardiol. 2018;114:288-299.

Liu W, Kim TY, Huang X, **Liu MB**, Koren G, Choi BR, Qu Z. ***Mechanisms linking T-wave alternans to spontaneous initiation of ventricular arrhythmias in rabbit models of long QT syndrome.*** J Physiol (Lond). 2018;

Ko CY, **Liu MB***, Song Z, Qu Z, Weiss JN. ***Multiscale Determinants of Delayed Afterdepolarization Amplitude in Cardiac Tissue.*** Biophys J. 2017;112(9):1949-1961.

Liu MB, Ko CY, Song Z, Garfinkel A, Weiss JN, Qu Z. ***A Dynamical Threshold for Cardiac Delayed Afterdepolarization-Mediated Triggered Activity.*** Biophys J. 2016;111(11):2523-2533.

Qu Z, **Liu MB,** Nivala M. ***A unified theory of calcium alternans in ventricular myocytes.*** Sci Rep. 2016;6:35625.

Liu MB, de Lange E, Garfinkel A, Weiss JN, Qu Z. ***Delayed afterdepolarizations generate both triggers and a vulnerable substrate promoting reentry in cardiac tissue***. Heart Rhythm. 2015;12(10):2115-24.

Bazalova-Carter M, **Liu M**, Palma B, Dunning M, McCormick D, Hemsing E, Nelson J, Jobe K, Colby E, Koong AC, Tantawi S, Dolgashev V, Maxim PG, Loo BW Jr. ***Comparison of film measurements and Monte Carlo simulations of dose delivered with very high-energy electron beams in a polystyrene phantom***. Med Phys. 2015;42(4):1606-13.

Liu MB, Eclov NC, Trakul N, Murphy J, Diehn M, Le QT, Dieterich S, Maxim PG, Loo BW. ***Clinical impact of dose overestimation by effective path length calculation in stereotactic ablative radiation therapy of lung tumors.*** Pract Radiat Oncol. 2013;3(4):294-300.

Selected Presentations

Liu MB. ***Arrhythmogensis in Long QT Syndromes: Mechanism of Initiation and Therapeutic Insight from an in silico Human Model*.** The Heart by Numbers: Integrating Theory, Computation, and Experiment to Advance Cardiology. 2018. (Invited Talk)

Song Z, **Liu MB**, Qu Z. ***Transverse Tubular Network Structures in the Genesis of Intracellular Calcium Alternans and Triggered Activity in Cardiac Cells.*** Circulation: Electrophysiology and Arrhythmias: AHA Scientific sessions. 2017 (Poster)

Liu MB. ***T-wave Alternans and Lability in the Initiation of Ventricular Arrhythmias under QT prolongation.*** Gordon Conference on Cardiac Arrhythmia Mechanisms. 2017. (Invited talk)

Liu MB, Ko C, Song Z, Garfinkel A, Weiss JN, Qu Z. **Determinants of the Diastolic Calcium-Voltage Coupling Gain for Delayed Afterdepolarization Mediated Triggered Activity**. Biophysical Journal. 2016;110(3)S1:586a. (Poster)

Liu MB, de Lange E, Garfinkel, A, Weiss JN, Qu Z. ***Delayed Afterdepolarizations Simultaneously Generate Triggers and Substrates to Initiate Reentrant Arrhythmias*.** Proceedings of the 36th Heart Rhythm Society Annual Scientific Sessions. 2015. (Poster)

Liu MB, Ko CY, Song Z, Garfinkel A, Weiss, JN, Qu Z. ***Hypokalemia Lowers the Threshold for a Delayed Afterdepolarization to Trigger an Action Potential Despite a Hyperpolarized Resting Potential*.** Proceedings of the 36th Heart Rhythm Society Scientific Sessions. 2015. (Poster)

Liu MB, Eclov NC, Trakul N, Diehn M, Maxim PG, Dieterich S, Loo BW. ***Ray-trace Calculation Significantly Overestimates Dose Compared To Monte Carlo Calculation In Cyberknife Stereotactic Ablative Radiotherapy Of Lung Tumors*.** Proceedings of the 53rd Annual ASTRO Meeting, International Journal of Radiation Oncology. 2011;81(2):S853. (Poster)

Awards

Poster Award – Gordon Conference on Cardiac Arrhythmia Mechanisms (2019)
Poster Award – Cardiac Physiome Society Annual Meeting (2016)
Poster Award – Gordon Conference on Cardiac Arrhythmia Mechanisms (2015)
Poster Award – Molecular Cellular & Integrative Physiology Retreat (2014)

Funding

NIH F30 MD/PhD Predoctoral Fellowship (2016-present)
American Heart Association Predoctoral Fellowship (2015-2016)
NIH T32 UCLA Molecular Cellular & Integrative Physiology Training Grant Fellow (2014-2015)

Chapter 1: Introduction

The cardiac conduction system

The human heart typically beats around once per second, about 100,000 times in a day, and 3 billion times in total over the course of an entire lifespan. This regular beating ensures that blood constantly circulates throughout the lungs and body. The synchronized contraction of first the two atria and then the two ventricles is controlled by the orderly electrical excitation of the cardiac tissue (Figure 1-1). During each heartbeat, these electrical signals originate from a natural pacemaker region in the right atrium called the sino-atrial node (SAN) and propagate throughout the atrial tissue until reaching the atrio-ventricular node (AVN) [3]. At the AVN, the electrical signals encounter a region of slowed conduction, which corresponds to the delay

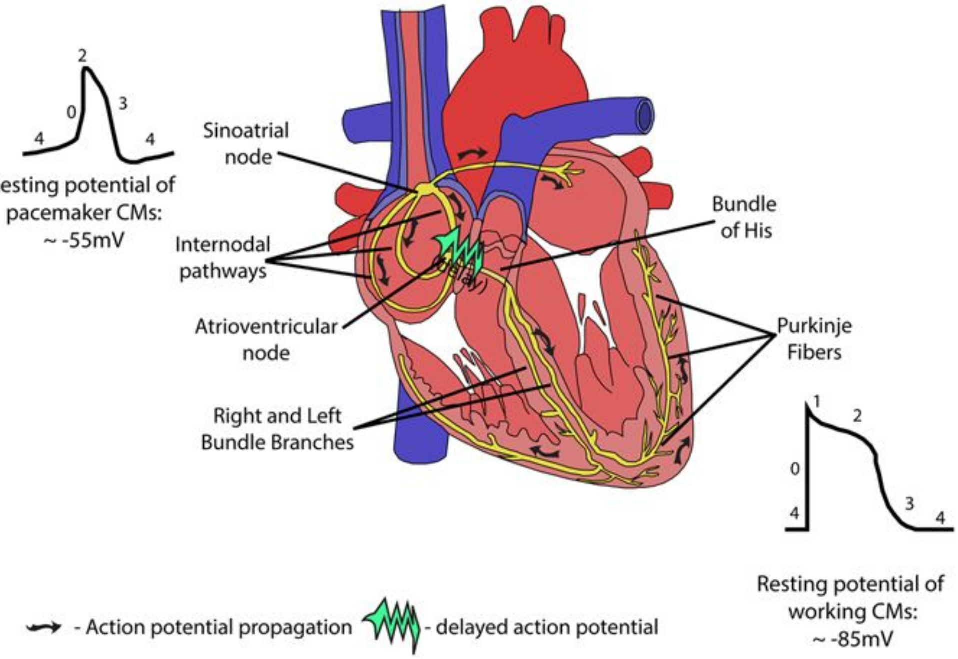

Figure 1-1*: The cardiac conduction system*

The cardiac conduction system serves to allow for the orderly electrical excitation of cardiac tissue, from the SAN, to the atria, to the AVN, through the bundle of His and Purkinje fibers, and finally to the ventricles. Reproduced from Monteiro et al [3] under CC.

between atrial contraction and ventricular contraction which are otherwise electrically insulated from each other, before proceeding to the extremely fast conducting fibers of the His-Purkinje network. The Purkinje network allows the electrical signals to ultimately reach the ventricular tissue in an extremely synchronized manner, causing each ventricular heart cell to contract in synchrony, resulting in the strong robust contraction required to pump blood through the pulmonary and systemic circulations [4]. This efficient cardiac conduction system encompasses multiple scales of organization, ranging from ion channel proteins, to the cellular level, to coupled cardiac tissue, and ultimately the whole organ [1].

Cardiac myocyte electrophysiology and excitation-contraction coupling

The cardiac cell, called a cardiac myocyte, is the fundamental unit of both cardiac electrophysiology and contraction. Myocytes are excitable rod-shaped muscle cells that make up cardiac tissue (Figure 1-2). Like all cells, myocytes are enclosed by a bi-lipid membrane which separate the intra and extra cellular spaces. A net difference of ionic concentrations between the inside and outside the cell sets up a voltage difference across the cell membrane. The primary ionic species involved include sodium (Na^+), calcium (Ca^{2+}), and potassium (K^+) [5].

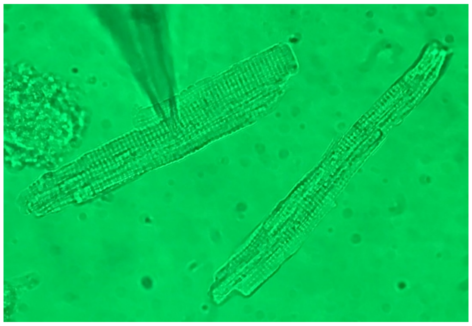

Figure 2-2: Ventricular cardiac myocytes isolated from a rabbit heart

A light microscopy image of two isolated rabbit ventricular myocytes.

Embedded in the membrane are ion channel proteins which include both passive and active transport types as wells as cotransporters. Each of these ion channels have their own unique properties, including voltage-gating, calcium-gating, and kinetic time constants, and produce inward and outward currents at different times to produce a whole-cell voltage depolarization called an action potential (AP) (Figure 1-3). The major cardiac currents include: the sodium current (I_{Na}), the L-type calcium current ($I_{Ca,L}$), the rapidly (I_{Kr}) and slowly (I_{Ks}) activating delayed rectifier potassium currents, the inward rectifying potassium current (I_{K1}), the transient

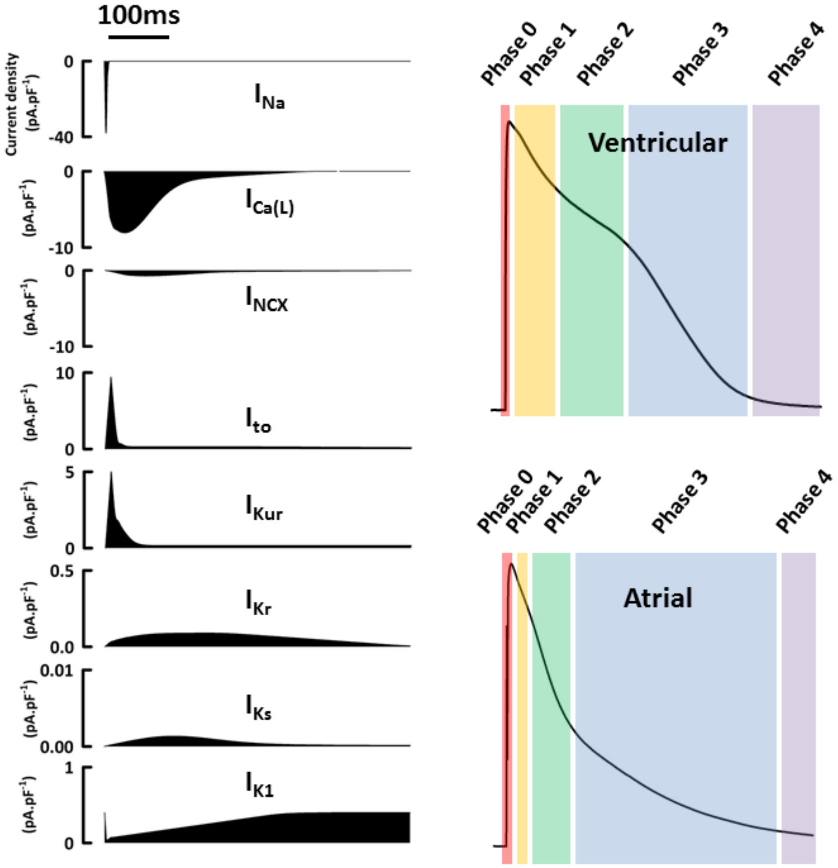

Figure 1-3: Cardiac action potential and major ionic currents

Different ionic currents activate with different time courses during the action potential, playing different roles in depolarization, plateau, repolarizing, and resting potential phases. Reproduced under CC from Wikimedia Commons[2].

outward voltage-gated potassium current (I_{to}), the sodium-calcium exchange current (I_{NCX}), and the sodium-potassium pump (I_{NaK}) [5-7]. These currents play different roles at the different phases of the action potential. For example I_{Na} is primarily responsible for the phase 0 depolarization upstroke with a threshold activation voltage of ~-60 mV, $I_{Ca,L}$ for the phase 2 plateau, and the various potassium currents for membrane repolarization in phase 3. The phase 4 resting potential of around -87 mV for human ventricular myocytes is primarily maintained by the balance between outward I_{K1} and inward I_{NCX}. Once excited, these cells also exhibit a refractory period during which they cannot be re-excited until the sodium channels have fully recovered. This refractory period plays an important role in both the initiation and the termination of arrhythmias [8].

In addition to being electrically excitable, myocytes are also muscle cells with sarcomeres consisting of actin fibrils and myosin heads utilizing ATP to contract the cell. The myosin binding sites on the actin fibrils are typically blocked by a protein complex called troponin, preventing muscle contraction. When calcium ions bind to troponin, a conformational change occurs and the myosin binding sites are revealed, allowing for contraction. The bulk of myocyte calcium is stored in a surrounding organelle called the sarcoplasmic reticulum (SR) and is released through a process called calcium-induced calcium release (CICR) involving the L-type calcium channels ($I_{Ca,L}$) in the cell membrane [9, 10]. Thus, when an action potential occurs and $I_{Ca,L}$ is activated, calcium is released from the SR, allowing for the sarcomere to contract – a process called excitation-contraction coupling which links the electrical signals to mechanical contraction [11, 12]. To facilitate synchronous contraction for all myofibrils including those deep in the cell,

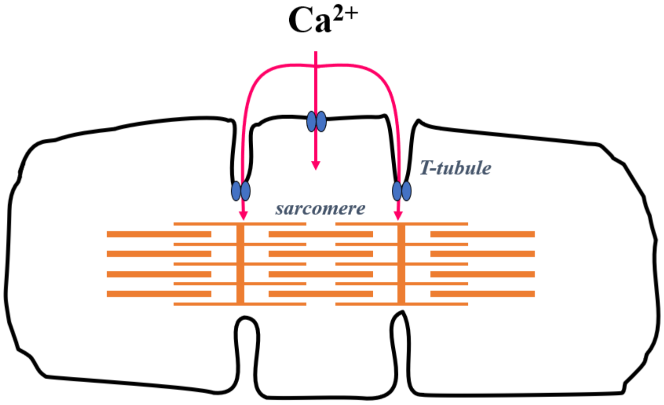

Figure 1-4: T-tubules allow for efficient contraction of the entire sarcomere

T-tubules are invaginations in the cell membrane that allow the calcium release units to be spaces regularly even in the interior of the cell.

myocytes, especially those in the ventricle, have regular invaginations of their cell membrane called transverse tubules or T-tubules (Figure 1-4) to allow the L-type calcium channels to stay within close proximity to the SR throughout the entire interior of the cell [13].

Different types of cells exist in different regions of the heart, each with different electrical and contractile properties and functions [14]. For example, ventricular myocytes with a size of 100-200 µm in length, 20-30 µm in width, and 10-20 µm in depth are larger than atrial myocytes to facilitate the increased contractile needs of the ventricles [15, 16]. Similarly, ventricular myocytes have the most regular T-tubules while atrial myocytes can have intermediate or sparse T-tubules [17, 18]. SAN and Purkinje cells can also be considered specialized myocytes with unique ion channel combinations to facilitate their roles. SAN cells exhibit a self-depolarizing phase 4 in their AP due to the so-called “funny” current (I_f) [19] while Purkinje cells have no T-tubules as they play no role in contraction but instead are only focused on fast conduction [20]. Together, these different types of cardiac cells form well-organized cardiac tissue that ultimately facilitates efficient and synchronous contraction at the whole organ level.

Cardiac tissue and electrical propagation

Cardiac tissue consists of a syncytium of myocytes that are coupled together with their neighbors by gap junctions formed by the protein connexin 43 [21]. These gap junctions allow for the passage of ions from once cell to another and generally obey a passive Ohm's law relationship. Thus, current will tend to flow from high to low voltage. When one myocyte fires an AP, its membrane voltage will be greater than that of its neighbor, causing current to flow which simultaneously reduces the voltage of the current cell, and increases the voltage of its neighbor. If there is enough current source, the voltage of the neighboring cell may rise sufficiently to the threshold for it to fire its own AP. With many cells, this results in a wave of electrical excitation propagating through the cardiac tissue, as each cell excites its neighbor, which through excitation-contraction coupling results in a corresponding wave of mechanical contraction. Therefore, synchronized excitation is essential for synchronized contraction. To facilitate their unique functions, different cardiac tissue have different conduction velocity (CV) properties. For instance, electrical conduction in atrial and ventricular tissue is around 0.5 m/s while the CV in the His-Purkinje system is significantly faster at 2-3 m/s, which is required for a highly synchronized ventricular activation [4].

Arrhythmias and sudden cardiac death

Under many conditions, irregular or abnormal heart rhythms can develop which are called arrhythmias. As the contraction of the heart is directly linked to its electrical excitation, an irregular rhythm translates to irregular contraction and potentially insufficient blood flow to the brain and other vital organs. If a severe abnormal rhythm persists, this can quickly lead to sudden cardiac death (SCD) which is a leading cause of death in developed countries, annually accounting for over 300,000 deaths in the United States of America alone [22, 23].

There are numerous different causes of arrhythmias. Many disease conditions can cause arrhythmias including scar or fibrosis formation after a myocardial infarction (MI), heart failure (HF), hypertrophic cardiomyopathy (HCM), and genetic disorders such as catecholaminergic polymorphous ventricular tachycardia (CPVT), Brugada syndrome, and the congenital long QT syndromes (LQTS) [5, 23-26]. Many drugs can induce arrhythmias as well as a side effect, with the problem becoming so severe that the U.S. Federal Drug Administration in 2005 started requiring new drugs to undergo a Thorough QT study to reject drugs that may have arrhythmia risk [27, 28]. Electrolyte abnormalities in potassium (hypo/hyperkalemia), sodium (hypo/hypernatremia), calcium (hypo/hypercalcemia), and magnesium (hypo/hypermagnesemia) also affect the ion channel behavior and can result in arrhythmias [5, 29]. And finally, arrhythmias can occur even in an otherwise physiologically normal heart due to a transient functional disturbance.

There are also many types of arrhythmias, with some dangerous but many benign or even self-terminating. Arrhythmias can be generally described as too slow a rhythm (bradycardia), too fast a rhythm (tachycardia), or a completely disorganized rhythm (fibrillation). Arrhythmias are often classified into two categories which are ventricular and supraventricular. Supraventricular arrhythmias, as the name suggests, originate before the ventricles in the cardiac conduction system, aka in the atria or His-Purkinje system. These include atrial tachycardia, atrial fibrillation, premature atrial contractions, sinus bradycardia, sick-sinus-syndrome, AVN block, or AVN reentrant tachycardia. Ventricular arrhythmias originate from the ventricles and can include premature ventricular contractions (PVCs), several different types of ventricular tachycardias (VT), and ventricular fibrillation (VF). Generally, supraventricular arrhythmias are less immediately dangerous than ventricular arrhythmias, as the AVN will act as a checkpoint, still allowing for synchronized contraction of the ventricles which is the main chamber for pumping blood. Sustained ventricular arrhythmias on the other hand, especially ventricular fibrillation, typically appear suddenly and can be immediately life threatening as the heart can lose its ability to pump blood. This dissertation primarily focuses on the initiation of ventricular arrhythmias.

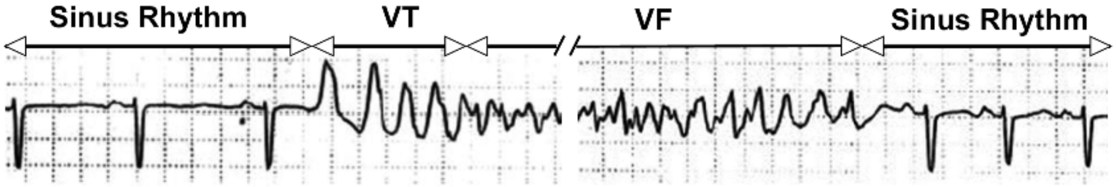

Figure 1-5: Electrocardiogram showing transition to arrhythmia

This patient starts out in normal sinus rhythm but then suddenly and abruptly initiates a ventricular tachycardia. After a few cycles, the VT transitions into the more disorganized ventricular fibrillation which is maintained for awhile. Luckily for this patient, the VF spontaneously terminated and the heart resumed sinus rhythm. Reproduced from Qu et al [1].

Treatment and prevention of arrhythmias

Life threatening ventricular arrhythmias share the key feature of a transition from an orderly sinus rhythm (controlled by the SAN) to disorganized turbulent electrical activity in the ventricles. Figure 1-5 shows an electrocardiogram (ECG) of a patient undergoing such a transition. The ECG is a clinical indicator of the weighted electrical activity in the heart as measured between electrode leads placed on different parts of the body surface. Generally, the

P-wave corresponds to atrial excitation, the QRS-complex to ventricular excitation, and the T-wave to ventricular repolarization. Clinicians are often able to assess and diagnose the underlying electrical behavior of the heart based on the rate, rhythm, and morphological appearance of the ECG. In this patient, we can see the complete evolution of an arrhythmia, from initiation (also called arrhythmogenesis), to the transition and maintenance of VF, and finally to its termination. This ECG starts out in normal sinus rhythm but then suddenly and abruptly changes to a short run of ventricular tachycardia with wide semi-regular QRS-complexes. This quickly transitions into a complexly disorganized and irregular rhythm known as ventricular fibrillation. During VF, the ventricles are not contracting as a synchronized unit and very little blood is being pumped forward to the lungs or body, which is life-threatening if sustained for more than a few minutes [30]. Fortunately for this patient, the arrhythmia spontaneously terminated before death occurred and the ECG reverted to sinus rhythm.

In most cases of VF however, the arrhythmia does not spontaneously revert back to normal rhythm, in which case electrical defibrillation is necessary to save the patient. Electrical defibrillation is an emergency procedure where a high energy electrical shock is delivered across the heart, simultaneously activating all non-refractory cardiac tissue and resetting the electrical state across the entire heart [31]. If successfully, this allows the SAN pacemaker to regain control and put the heart back into sinus rhythm. For patients with a known risk for arrhythmias and SCD, an implantable cardioverter-defibrillator (ICD) can be implanted under the skin, with leads monitoring the heart at all times ready to deliver a defibrillation shock at any time automatically without any human intervention. This remains the most effective therapy to date for the prevention of SCD, but are far from an ideal solution due to their severe side effects including pain and sudden inappropriate shocks [32]. There is also an enormous challenge for the cost-effective use of ICDs as currently the clinical risk stratification of patients is of limited accuracy. ICDs are expensive to implant but clinical trials have shown that only one out of every five implanted ICDs ever actually deliver a life-saving shock [33, 34]. In other worlds, due to our limited ability to predict which patients will actually experience a life-threatening arrhythmia event, we implant unnecessary ICDs in 80% of patients. Finally, defibrillation, as important a tool as it is, can be considered a rather crude strategy as it is always reactive, focusing on the termination of existing sustained arrhythmias after they have already occurred. At this point, the patient has likely already fainted from lack of perfusion and the ICD only serves to shock them back into normal rhythm before permanent organ damage occurs. While potentially life-saving, the long-term quality of life for ICD patients in this manner can be poor.

A more ideal strategy would be the prevention of arrhythmias before they initiate altogether. Sometimes there may be a clear anatomical region where the arrhythmia is initiating from (e.g. a scar or fibrosis from a previous myocardial infarction). In these cases, a process called ablation can be used, where a radiofrequency or cryogenic catheter is used to burn tissue and make it electrically unexcitable [35]. This is done in a manner that isolates or destroys the circuit allowing the arrhythmia to occur. Ablation however of course sacrifices healthy cardiac tissue and in cases where no obvious anatomical arrhythmia source is present cannot always be used, especially in the ventricles. Therefore, pharmacological approaches exist as well.

Over the decades many anti-arrhythmic drugs have been developed in 4 main classes with the goal of preventing arrhythmias: (Class I, sodium channel blockers; Class II, beta blockers; Class III, potassium channel blockers; Class IV, calcium channel blockers) [36]. Most of these classes unsurprisingly target the ion channels of the three main relevant ions in myocyte electrophysiology: sodium, potassium, and calcium. Unfortunately, multiple clinical trials have demonstrated that most of these drugs are not actually effective overall in preventing arrhythmias, and some may even increase mortality over placebo [37-39]. It may seem paradoxical that drugs intended to be anti-arrhythmic could have a pro-arrhythmic effect, which highlights the complex intertwined nature of cardiac electrophysiology. A drug that decreases arrhythmia risk from one mechanism may inadvertently increase the risk from another mechanism. For example, the Cardiac Arrhythmia Suppression Trials (CAST I [37] and CAST II [38]) in 1991 and 1992 demonstrated that sodium channel blockers were successful in preventing premature ventricular contractions (PVCs), but increased the number of arrhythmia-related deaths overall.

In order to develop future more effective arrhythmia prevention strategies, a broad mechanistic understanding of arrhythmogenesis, the process by which arrhythmias are initiated, is needed.

Focal and reentrant arrhythmias

Typically, ventricular arrhythmias can be thought of either as focal or reentrant [26]. In focal arrhythmias, abnormal electrical impulses are generated and propagate out from a source region in all directions, forming a pattern called a target wave (Figure 1-6A). These arrhythmias are considered a problem with impulse initiation and abnormal automaticity, and are thought to be related to cellular early-afterdepolarizations (EADs) and delayed-afterdepolarizations (DADs).

Reentrant arrhythmias are more clearly defined and occur through a process called reentry, in which the electrical wave travels in a repetitive circular motion (also sometimes described as "circus movement") and can be either anatomical or functional in nature. Reentry is so-named because the tip of the wave appears to re-enter on itself, forming a periodic circular pattern. In anatomical reentry, the electrical wave circles along an anatomical obstacle or pathway, resulting in a tachycardia since the rotation speed of the reentry is typically much faster than normal sinus rhythm. This type of anatomical reentry as an arrhythmia mechanism was first hypothesized in 1887 [40] and experimentally demonstrated in canine hearts in 1913-14 [41]. The obstacle or pathway could be a normal anatomical structure or from a pathological process such as scarring or fibrosis after heart injury. Ablation therapies are most effective against anatomical reentrant arrhythmias when a reentrant obstacle or pathway can be identified to be isolated and ablated.

Reentry can also occur without any anatomical obstacles, even in homogeneous tissue. This type of behavior is called functional reentry and results from the phenomenon of spiral waves, which rotate around a phase singularity rotation core. Spiral waves were studied in general excitable media [42-44] long before their application to cardiac arrhythmias in the 1980's [45, 46], with experimental evidence of this phenomenon in cardiac tissue appearing both before [47] and after [48, 49] the theory was formalized. Experimental and computational modeling studies that followed have linked spiral waves to different forms of VT depending on the stable or meandering nature of the phase singularity, as well as chaotic spiral wave breakup to VF [50, 51]. With these insights, the field of computational cardiology has exploded in the theoretical and computational investigation of the dynamical properties of spiral wave maintenance, transitions, and termination [52-54]. For example, conduction velocity was shown to be an important component of the cardiac tissue wavelength which determines whether a spiral wave could be maintained in a particular tissue size [55]. Steep action potential duration (APD) restitution has been shown to be a critical necessary component for spiral wave breakup and the transition from VT to VF [56, 57]. Techniques using optogenetics have even been developed for spiral wave control in *in* vitro experimental systems, allowing a laser beam to steer and modulate the behavior of a spiral wave in tissue [58, 59]. Despite these sophisticated advances, our understanding of reentrant arrhythmia initiation has remained fairly simplistic, even though arrhythmogenesis represents an ideal target for clinical arrhythmia prevention.

Arrhythmogenesis: The role of triggers and substrates

Traditionally, reentrant arrhythmias are thought to initiate when two independent aspects combine: a trigger and a substrate [26]. The arrhythmogenic trigger is an abnormal excitation event, while the arrhythmogenic substrate are the potentially dangerous tissue conditions, and when the two are combined with the proper timing planar wave break occurs and a reentrant wave is formed. Triggers can arise from automaticity, early-afterdepolarizations, delayed-afterdepolarizations, (which when sustained by themselves are considered focal arrhythmias), or even external forces such as chest thumps or electrical shocks. Triggers can originate from anywhere in the heart including the atria, His-Purkinje conduction system, and the ventricles. Generally, the exact nature of the trigger is not considered to be important, as long as it provides an initial wave to be broken up by the substrate and allowed to reenter.

The role of the substrate is to break up the planar wavefront from the trigger in such a manner that it has enough room to form reentry without running into itself and annihilating. Substrates can be anatomical substrates, in the case of post-MI scar and fibrosis as discussed before, or functional substrates in the case of S1-S2 initiation or dispersion of repolarization. Functional substrates are dynamically more interesting and arise due to the fact that cardiac cells have a electrical refractory period during which they cannot be excited until the sodium channel has fully recovered.

S1-S2 initiation is the simplest case where an external depolarization is suddenly superimposed overlapping the waveback of a repolarizing tissue [60]. Because the region closest to the waveback is in its refractory period, it is unable to fire an action potential while the region further away can. This results in electrical conduction being blocked in the direction toward the waveback, but propagating in the direction away. Since the wave now travels only in one direction, it has the opportunity to curve in on itself and if given enough space form a reentry. Note that this phenomenon did not require any anatomical heterogeneities and can in fact occur in completely homogeneous tissue. Clinical examples of S1-S2 include comodio cordis, where a severe chest thump sometimes from a sports impact is able to depolarize cardiac tissue right during the repolarization phase of the ventricles, or during a poorly timed defibrillation attempt when the shock is delivered to a heart that still has a somewhat organized rhythm at just the wrong timing, impacting during ventricular repolarization and starting a new arrhythmia instead of terminating the last. The latter scenario is the reason for synchronized cardioversion, where the defibrillator will attempt to place the shock on during a QRS complex to avoid ventricular repolarization during the T-wave. This precise timing requirement is represented by a concept called the vulnerable window for reentry, which corresponds to the narrow time window in which the external stimulation can initiate a reentry. This mechanism is also why arrhythmias can be induced in a completely physiologically normal heart

The external trigger in S1-S2 initiation is rather artificial and does not apply to the majority of arrhythmias encountered clinically which typically arise spontaneously without an obvious external trigger. In these cases, reentrant arrhythmias are thought to arise through a process called unidirectional conduction block [61-63]. Traditional triggers for spontaneous ventricular arrhythmias are thought to arise from EADs or DADs in certain areas of the cardiac tissue, which under certain conditions can propagate out as a target wave causing a PVC. If this traveling ectopic wave by chance encounters a repolarizing region with the exact wrong timing, the wave may not be able to progress in that direction due to the refractory period of the repolarizing tissue. In this case, conduction is blocked in that one direction, but not the surrounding directions, breaking up the original wave into two. Similar to before, if given enough room for the tips to not collide and annihilate, the two wavefronts reenter on each other to form what is called a figure-of-eight reentry with two symmetrical spiral waves. Therefore, the entirety of the trigger substrate interaction in this mechanism boils down to whether the timing and the geometry allows for unidirectional conduction block to occur with enough room for reentry, similar to the concept of the vulnerable window in S1-S2 initiation although less clearly defined. Dispersion of repolarization, or a wide range of heterogenous APDs across the tissue, is known increase the likelihood that unidirectional conduction block will occur somewhere in the tissue, and therefore is considered a functional substrate for arrhythmias.

Triggers and substrates traditionally have been considered as independent factors, with the probability of arrhythmias being the probability of a trigger occurring coupled with the timing in relation to a substrate [26, 64]. This interpretation is often cited as a qualitative explanation to justify the relative rarity of arrhythmia events, even in those patients with risk factors. This thinking was also the original justifications for trials such as CAST, as eliminating potential PVC triggers with sodium channel blockers was envisioned to have eliminated the arrhythmias as well. However, as discussed previously, the result in this case was in fact the opposite, with the reduction of PVC triggers paradoxically increasing overall mortality from arrhythmias. Thus, it has become clear that the real physiology in the heart is more complicated than independent triggers and substrates meeting by chance. An intervention that decreases the incidence of triggers may actually simultaneously make the substrate worse, or in some cases there may not be a clear distinction between the trigger and substrate at all when arrhythmogenesis occurs.

Throughout this dissertation, the complex nature of triggers and substrates is investigated with a focus on advancing our understanding of clinically relevant spontaneous arrhythmogenesis beyond the traditional paradigm.

Calcium cycling and delayed afterdepolarizations

A major source of spontaneous triggered activity is thought to arise from DADs [5, 26, 64-67]. DADs are simply defined as additional depolarizations during late phase 4 after an AP has already finished repolarizing. They are known to occur more frequently in diseased hearts, including those in heart failure, CPVT, and calcium overload conditions, and are mechanistically linked to spontaneous calcium waves. Calcium is one of the most involved ions in the myocyte, responsible for both the plateau phase of the AP as well as being the primary link in excitation-contraction coupling. As such, the myocyte has large stores of Ca^{2+} in the SR which is released through calcium-induced calcium-release (CICR) in concert with the membrane $I_{Ca,L}$. This tight coupling between the membrane calcium current and the SR release forms what is called the calcium cycling system of the myocyte.

The fundamental functional unit of the calcium cycling system is the calcium release unit (CRU) [9]. A basic CRU consists of a specialized junctional domain of the SR with special calcium release channels called ryanodine receptors (RyRs) in close proximity with the myocyte membrane's L-type calcium channels. After an action potential releases the SR Ca^{2+} into the cytoplasm, the SERCA channel uses ATP to pump the Ca^{2+} back into the SR, ready for the next beat. The Na-Ca exchanger (NCX) and Na-K pump also play a role in maintaining Ca^{2+} balance. These processes are collectively referred to as calcium cycling, as the myocyte's calcium is constantly cycled between the SR and the cytoplasm to facilitate contraction, tightly coupled to the electrical AP.

A ventricular myocyte contains a large CRU network consisting of approximately 20,000 CRUs integrated into its T-tubule network. When one CRU fires, aka the RyRs open and begin releasing Ca^{2+} from the SR, Ca^{2+} can diffuse in the cytoplasm to neighboring CRUs, which through CICR can cause the neighbors to fire as well, a process sometimes referred to as "fire-diffuse-fire". If a number of neighboring CRUs are able to fire together, they can form a Ca^{2+} spark [68, 69]. If neighboring CRUs are able to sustain a chain of sequential firings, then a Ca^{2+} wave can occur [68]. The transition between Ca^{2+} sparks and Ca^{2+} waves can be explained neatly through a theory of self-organized criticality with a dependence on Ca^{2+} load as well as RyR leakiness [70, 71]. It is these spontaneous Ca^{2+} waves that are thought to generate DADs, as an excess of Ca^{2+} in the cytoplasm will activate NCX to restore Ca^{2+} balance, producing a voltage depolarization as current moves across the channel. If the membrane voltage is able to rise to the level of the sodium channel threshold (~60 mV), a triggered AP can occur in the myocyte. For coupled cardiac tissue, the requirements for triggered activity (TA) also involve the source-sink relationship between the cells having DADs and those without, as the cell voltages will be smoothed across the tissue. If the DADs are able to cause TA in tissue, they may propagate out as a target wave PVC and potentially act as an arrhythmogenic trigger if it encounters a substrate.

Chapters 2, 3, and 4 of this dissertation all investigate arrhythmogenic mechanisms related to DADs using a combined computational and experimental approach. Computer modeling and patch clamp experiments in isolated myocytes provide complimentary tools to test our hypotheses. Chapter 2 looks at the factors affecting the single myocyte threshold for DADs to elicit triggered activity, which is elucidated in the case of hypokalemia and is not strictly just the Na channel threshold at -60 mV. An analytical expression for this “dynamical threshold” for triggered activity is derived from non-linear dynamics analysis, which is then validated in both single cell computer modeling as well as patch clamp experiments in rabbit myocytes. Chapter 3 explores the multiple factors that affect the probability of TA formation in tissue, using experimentally measured DAD properties as physiological inputs into the cardiac tissue simulations. Chapter 4 then uses computational modeling to investigate the role DADs play at the tissue level not only as arrhythmogenic triggers, but also as a functional substrate as well, combining the origins of trigger and substrate from the same source.

Long QT syndromes

Long QT syndromes (LQTS) are also associated with increased risk of arrhythmias, particularly polymorphic ventricular tachyarrhythmias (PVT) and torsades de points (TdP) [25, 72-76]. LQTS can be congenital LQTS, arising from numerous different genetic mutations with 16 different subtypes [77], or acquired LQTS due to drug side effects [28]. While the specific ionic causes of LQTS can differ (e.g. LQT1 is a mutation in I_{Ks}, LQT2 in I_{Kr}, and LQT3 in I_{NaL}), they all result in a prolonged QT interval. The QT interval is the time between the QRS complex and the end of the T-wave on ECG, which roughly corresponds to the time interval between ventricular depolarization and repolarization, mainly affected by the cellular APD. The classical mechanism by which LQTS leads to arrhythmias also generally follows the traditional trigger substrate paradigm. APD prolongation can enhance existing heterogeneities, and is additionally exacerbated under beta-adrenergic stimulation, which leads to an increased dispersion of repolarization, a well-known substrate for reentrant arrhythmias [26].

APD prolongation is also known to make myocytes prone to EADs, which are after-depolarizations occurring earlier than DADs during phase 3 of the AP [78, 79]. Cellular EADs have been studied extensively in both experimental and computational contexts and are known to arise due to a reactivation of the I_{CaL} window current [80-82]. EADs in tissue also are affected by the source-sink relationship [83, 84] although the propagation of PVCs from an I_{CaL} instability in tissue has been shown to not necessarily require EADs to be present [73]. Therefore, it is thought that APD prolongation may also increase EAD-mediated triggered activity acting as an arrhythmogenic trigger.

Chapter 5 investigates mechanisms of arrhythmia formation in different LQTS genotypes, not only with respect to arrhythmia initiation itself but also explaining the characteristic ECG patterns commonly seen in LQTS patients before PVT occurs, including pause-dependent short-long-short sequences, T-wave alternans, and R-on-T phenomena. We detail a novel common mechanism of LQTS arrhythmias, which we call “R-from-T”, that blurs the distinction between trigger and substrate roles. Using our new knowledge of this common mechanism, we then detail a unified therapeutic strategy for arrhythmia prevention in LQTS.

Multiscale computational modeling of cardiac electrophysiology

Computational modeling is an important research tool, complementary to experimental and clinical studies, to reveal the underlying mechanisms of arrhythmias. Modeling studies have a unique advantage in investigating the specific effects of each individual change involved in cardiac remodeling due to the accessibility of all state variables in the cell throughout the simulation experiment. Furthermore, computer modeling is able to simulate interventions and track multiple parameters in ways that are physically impossible in experimental models, providing crucial mechanistic insight. In this dissertation, cardiac electrophysiology is modeled at multiple levels as appropriate to the question at hand (Figure 1-6). While anatomical whole heart modeling with a full Purkinje network system is necessary for certain clinical questions, such as investigating the ECG patterns of LQTS initiation, many mechanistic insights are actually more easily obtained in concert with simpler cellular or tissue models. Ultimately, a combination of modeling scales is usually appropriate for the most complete understanding of the phenomenon.

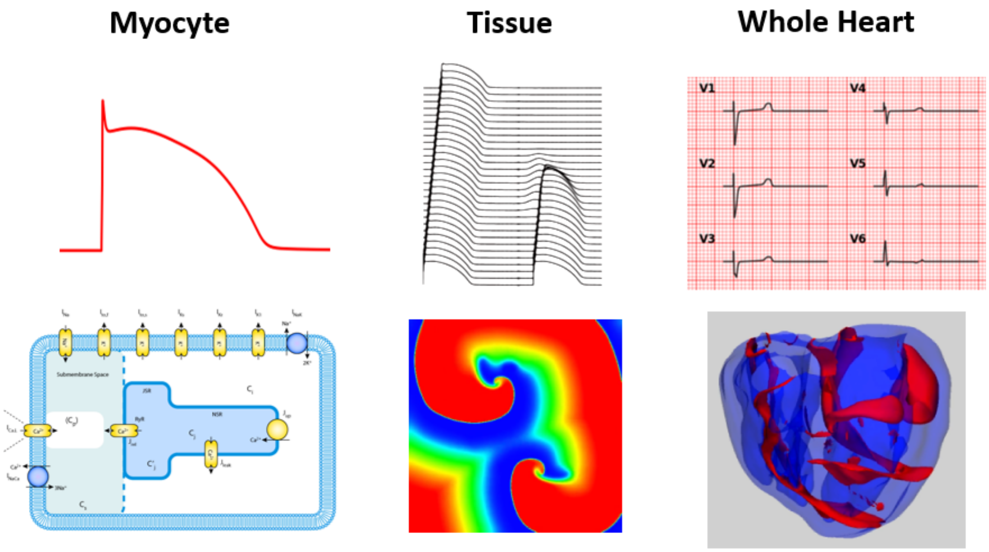

Figure 1-6: Multiscale cardiac modeling

The heart has many different scales of dynamics traversing from a single myocyte to the whole heart. Simulations should be performed at a scale appropriate for the problem at hand for the clearest understanding of the phenomenon.

Single myocyte modeling

Cardiac computational modeling was first performed in 1963 by Denis Noble's group who developed the first cardiac AP model using modified Hodgkin-Huxley neuronal AP equations computed on a 1 ton "Ferranti Mercury" computer [85]. Since then, many cardiac AP models have been creating ranging over many cell types and species [86-92]. Early models, such as the Luo-Rudy (LR1) guinea pig model [90] only incorporated Na^+, Ca^{2+}, and K^+ currents, while the later models include not only numerous currents, but also equations for the calcium cycling system as well [89, 91, 92].

Despite the large diversity of models, all single myocyte action potentials are simulated in a similar manner. The master ordinary differential equation (ODE) for the membrane voltage of the myocyte is

$$\frac{dV}{dt} = -\frac{1}{C_m} \cdot I_{total}$$

where *dV/dt* is the change in voltage over time, C_m is the membrane capacitance, and I_{total} is the sum of all ionic currents in the cell. Therefore, to compute the change in voltage over any given simulation timestep, we only needs to compute the numerical value of I_{total}. Each of the component currents in I_{total} will have their own set of differential equations, and can consist of Hodgkin-Huxley type equations, Markov chain formulations, or other voltage or ligand gated schemes. Regardless of the details, as long as a numerical value can be computed for each current, the equation for voltage can be numerically integrated. As the cardiac myocyte is a non-conservative system, a simple Euler integration scheme usually suffices, although this can be supplemented with adaptive time-stepping or higher order (e.g. Runge-Kutta) methods when required.

In this dissertation, the cellular AP models used were the UCLA rabbit ventricular myocyte model [91] in Chapters 2, 3, and 4, and the O'Hara-Rudy human ventricular myocyte model [92] and the Stewart human Purkinje fiber model [88] in Chapter 5.

Cardiac tissue modeling

To model cardiac tissue coupled by gap junctions, the single cell ODE is modified with an additional partial differential equation (PDE) term to describe the diffusion of voltage between neighboring cells. Gap junctions are modeled as passive channels obeying Ohm's law ($\Delta V = IR$). Adding this results in the following general tissue master equation

$$\frac{\partial V}{\partial t} = -\frac{1}{C_m} \cdot I_{total} + D\left(\frac{\partial^2 V}{\partial x^2} + \frac{\partial^2 V}{\partial y^2} + \frac{\partial^2 V}{\partial z^2}\right)$$

where *D* is the voltage diffusion constant related to gap junction connectivity, and $\left(\frac{\partial^2 V}{\partial x^2} + \frac{\partial^2 V}{\partial y^2} + \frac{\partial^2 V}{\partial z^2}\right)$ is the net differences in voltage between neighboring cells in all directions. The diffusion constant *D* can be modified to simulate conditions of reduced gap junction conductance and slow conduction. Because the time scales of the ionic ODE and the diffusion PDE can be different, techniques such as operator splitting have been developed to allow for more efficient computation [93]. Advances in general-purpose graphics processing unit (GPGPU) technology has also allowed for massively parallel simulations, reducing the computational runtime of cardiac tissue simulations by orders of magnitude. This computational speed up becomes necessary as the tissue size is scaled up, especially at the whole organ level.

Anatomical whole heart modeling

Modeling the heart at the whole organ level is a complex and intensive task, but necessary to investigate the clinical ECG features in LQTS in Chapter 5. The basic principles of modeling the anatomical heart are more or less similar to those governing cardiac tissue. The cellular ODE still applies for every cell in the heart, except now there are millions of cells to be computed, and there still needs to be a differential equation governing the voltage diffusion between neighboring cells. Unlike general cardiac tissue, the cells in the anatomical heart are not arranged in a strict rectangular grid and instead form fibers with anisotropic conduction properties following a complex geometrical pattern. Models can either use experimentally measured fiber orientations, often obtained using diffusion-tensor weighted MRI (DT-MRI) [94, 95], or use a general set of fiber rotation principles called the Streeter rules [96]. From this, the anatomical heart is governed by the following partial differential equation

$$\frac{\partial V}{\partial t} = -I_{ion}/C_m + \sum_i \sum_j \frac{\partial}{\partial x_i} D_{ij} \frac{\partial}{\partial x_j} V$$

where D_{ij} is the 3D conductivity tensor describing the anisotropy of voltage propagation corresponding to the fiber direction field, with *i,j* as indices for the 3 cartesian dimensions.

Anatomical heart modeling also can incorporate a coupled Purkinje network model [97-100]. As described in more detail in Chapter 5, the cardiac conduction system was modeled starting at the AV node, including the His bundle and the Purkinje network which is ultimately coupled to the ventricular myocardium. Our model represented the Purkinje network as a connected set of 1D cables that branches into a mesh network at the endocardial surface. Altogether, this coupled Purkinje ventricular model enables the simulation of retrograde conduction block and compensatory pauses following PVCs that play an important role for arrhythmogenesis in LQTS.

References

1. Qu, Z., et al., *Nonlinear and Stochastic Dynamics in the Heart.* Phys Rep, 2014. **543**(2): p. 61-162.

2. PeaBrainC, *Currents responsible for the cardiac action potential*. 2015: Wikimedia Commons.

3. Monteiro, L.M., et al., *Restoring heart function and electrical integrity: closing the circuit.* npj Regenerative Medicine, 2017. **2**(1): p. 9.

4. Durrer, D., et al., *Total excitation of the isolated human heart.* Circulation, 1970. **41**(6): p. 899-912.

5. P Zipes, D. and J. Jalife, *Cardiac Electrophysiology: From Cell to Bedside*. WB Saunders Company. Vol. xvi. 2000.

6. Bartos, D.C., E. Grandi, and C.M. Ripplinger, *Ion Channels in the Heart.* Comprehensive Physiology, 2015. **5**(3): p. 1423-1464.

7. Grant, A.O., *Cardiac Ion Channels.* Circulation: Arrhythmia and Electrophysiology, 2009. **2**(2): p. 185-194.

8. Burton, F.L. and S.M. Cobbe, *Dispersion of ventricular repolarization and refractory period.* Cardiovascular Research, 2001. **50**(1): p. 10-23.

9. Stern, M.D., *Theory of excitation-contraction coupling in cardiac muscle.* Biophysical Journal, 1992. **63**(2): p. 497-517.

10. Fabiato, A., *Calcium-induced release of calcium from the cardiac sarcoplasmic reticulum.* American Journal of Physiology-Cell Physiology, 1983. **245**(1): p. C1-C14.

11. Bers, D.M., *Cardiac excitation–contraction coupling.* Nature, 2002. **415**: p. 198.

12. Bers, D.M., *Excitation-Contraction Coupling and Cardiac Contractile Force*. 2nd ed. 2001, Dordrecht: Kluwer Academuc Publishers. 149-151.

13. Brette, F. and C. Orchard, *T-Tubule Function in Mammalian Cardiac Myocytes.* Circulation Research, 2003. **92**(11): p. 1182-1192.

14. Shih, H.T., *Anatomy of the action potential in the heart.* Texas Heart Institute journal, 1994. **21**(1): p. 30-41.

15. Campbell, S.E., A.M. Gerdes, and T.D. Smith, *Comparison of regional differences in cardiac myocyte dimensions in rats, hamsters, and guinea pigs.* Anat Rec, 1987. **219**(1): p. 53-9.

16. Satoh, H., et al., *Surface:volume relationship in cardiac myocytes studied with confocal microscopy and membrane capacitance measurements: species-dependence and developmental effects.* Biophys J, 1996. **70**(3): p. 1494-504.

17. Kirk, M.M., et al., *Role of the transverse-axial tubule system in generating calcium sparks and calcium transients in rat atrial myocytes.* J Physiol, 2003. **547**(Pt 2): p. 441-51.

18. Frisk, M., et al., *Variable t-tubule organization and Ca2+ homeostasis across the atria.* Am J Physiol Heart Circ Physiol, 2014. **307**(4): p. H609-20.

19. DiFrancesco, D. and J.S. Borer, *The funny current: cellular basis for the control of heart rate.* Drugs, 2007. **67 Suppl 2**: p. 15-24.

20. Di Maio, A., H.E. Ter Keurs, and C. Franzini-Armstrong, *T-tubule profiles in Purkinje fibres of mammalian myocardium.* J Muscle Res Cell Motil, 2007. **28**(2-3): p. 115-21.

21. Kanno, S. and J.E. Saffitz, *The role of myocardial gap junctions in electrical conduction and arrhythmogenesis.* Cardiovasc Pathol, 2001. **10**(4): p. 169-77.

22. Zipes, D.P. and H.J. Wellens, *Sudden cardiac death.* Circulation, 1998. **98**(21): p. 2334-51.

23. Rubart, M. and D.P. Zipes, *Mechanisms of sudden cardiac death.* J Clin Invest, 2005. **115**(9): p. 2305-15.

24. Mann, D.L., et al., *Braunwald's Heart Disease: A Textbook of Cardiovascular Medicine*. 10th ed. 2015, Philadelphia: Elsevier Saunders.

25. Morita, H., J. Wu, and D.P. Zipes, *The QT syndromes: long and short.* The Lancet, 2008. **372**(9640): p. 750-763.

26. Antzelevitch, C. and A. Burashnikov, *Overview of Basic Mechanisms of Cardiac Arrhythmia.* Cardiac electrophysiology clinics, 2011. **3**(1): p. 23-45.

27. Darpo, B., *The thorough QT/QTc study 4 years after the implementation of the ICH E14 guidance.* British journal of pharmacology, 2010. **159**(1): p. 49-57.

28. Fermini, B. and A.A. Fossa, *The impact of drug-induced QT interval prolongation on drug discovery and development.* Nature Reviews Drug Discovery, 2003. **2**: p. 439.

29. Surawicz, B., *Role of electrolytes in etiology and management of cardiac arrhythmias.* Progress in Cardiovascular Diseases, 1966. **8**(4): p. 364-386.

30. Witkowski, F.X., et al., *Spatiotemporal evolution of ventricular fibrillation.* Nature, 1998. **392**: p. 78.

31. Nichol, G., et al., *Defibrillation for Ventricular Fibrillation: A Shocking Update.* Journal of the American College of Cardiology, 2017. **70**(12): p. 1496-1509.

32. Tung, R., P. Zimetbaum, and M.E. Josephson, *A critical appraisal of implantable cardioverter-defibrillator therapy for the prevention of sudden cardiac death.* J Am Coll Cardiol, 2008. **52**(14): p. 1111-21.

33. Bardy, G.H., et al., *Amiodarone or an implantable cardioverter-defibrillator for congestive heart failure.* N Engl J Med, 2005. **352**(3): p. 225-37.

34. Turakhia, M. and Z.H. Tseng, *Sudden Cardiac Death: Epidemiology, Mechanisms, and Therapy.* Current Problems in Cardiology, 2007. **32**(9): p. 501-546.

35. Wissner, E., K.-H. Kuck, and W.G. Stevenson, *Catheter ablation of ventricular tachycardia in ischaemic and non-ischaemic cardiomyopathy: where are we today? A clinical review.* European Heart Journal, 2012. **33**(12): p. 1440-1450.

36. Kowey, P.R., *Pharmacological Effects of Antiarrhythmic Drugs: Review and Update.* Archives of Internal Medicine, 1998. **158**(4): p. 325-332.

37. Echt, D.S., et al., *Mortality and morbidity in patients receiving encainide, flecainide, or placebo. The Cardiac Arrhythmia Suppression Trial.* N Engl J Med, 1991. **324**(12): p. 781-8.

38. *Effect of the antiarrhythmic agent moricizine on survival after myocardial infarction.* N Engl J Med, 1992. **327**(4): p. 227-33.

39. Waldo, A.L., et al., *Effect of d-sotalol on mortality in patients with left ventricular dysfunction after recent and remote myocardial infarction. The SWORD Investigators. Survival With Oral d-Sotalol.* Lancet, 1996. **348**(9019): p. 7-12.

40. McWilliam, J.A., *Fibrillar Contraction of the Heart.* The Journal of physiology, 1887. **8**(5): p. 296-310.

41. Mines, G.R., *On dynamic equilibrium in the heart.* The Journal of physiology, 1913. **46**(4-5): p. 349-383.

42. Winfree, A.T., *Spiral Waves of Chemical Activity.* Science, 1972. **175**(4022): p. 634-636.

43. Suzuki, R.S., S; Nagumo, J, *Electrochemical Active Network.* Notes of Professional Group on Nonlinear Theory of IECE (Japan), 1963.

44. Zhabotinsky, A.M. and A.N. Zaikin, *Autowave processes in a distributed chemical system.* Journal of Theoretical Biology, 1973. **40**(1): p. 45-61.

45. Winfree, A.T., *Electrical instability in cardiac muscle: phase singularities and rotors.* J Theor Biol, 1989. **138**(3): p. 353-405.

46. Morris, S.A. and P.J. Nyikos, *Sudden cardiac arrest and a problem in topology.* The Journal of the Australian Mathematical Society. Series B. Applied Mathematics, 2009. **33**(2): p. 123-132.

47. Allessie, M.A., F.I. Bonke, and F.J. Schopman, *Circus movement in rabbit atrial muscle as a mechanism of tachycardia. III. The "leading circle" concept: a new model of circus movement in cardiac tissue without the involvement of an anatomical obstacle.* Circ Res, 1977. **41**(1): p. 9-18.

48. Chen, P.S., et al., *Mechanism of ventricular vulnerability to single premature stimuli in open-chest dogs.* Circ Res, 1988. **62**(6): p. 1191-209.

49. Frazier, D.W., et al., *Stimulus-induced critical point. Mechanism for electrical initiation of reentry in normal canine myocardium.* J Clin Invest, 1989. **83**(3): p. 1039-52.

50. Gray, R.A., et al., *Nonstationary vortexlike reentrant activity as a mechanism of polymorphic ventricular tachycardia in the isolated rabbit heart.* Circulation, 1995. **91**(9): p. 2454-69.

51. Weiss, J.N., et al., *The dynamics of cardiac fibrillation.* Circulation, 2005. **112**(8): p. 1232-40.

52. Niederer, S.A., J. Lumens, and N.A. Trayanova, *Computational models in cardiology.* Nature Reviews Cardiology, 2019. **16**(2): p. 100-111.

53. Fenton, F. and A. Karma, *Vortex dynamics in three-dimensional continuous myocardium with fiber rotation: Filament instability and fibrillation.* Chaos: An Interdisciplinary Journal of Nonlinear Science, 1998. **8**(1): p. 20-47.

54. Weiss, J.N., et al., *Perspective: A dynamics-based classification of ventricular arrhythmias.* J Mol Cell Cardiol, 2015. **82**: p. 136-152.

55. Smeets, J.L., et al., *The wavelength of the cardiac impulse and reentrant arrhythmias in isolated rabbit atrium. The role of heart rate, autonomic transmitters, temperature, and potassium.* Circ Res, 1986. **58**(1): p. 96-108.

56. Qu, Z., J.N. Weiss, and A. Garfinkel, *Cardiac electrical restitution properties and stability of reentrant spiral waves: a simulation study.* Am J Physiol, 1999. **276**(1): p. H269-83.

57. Qu, Z., et al., *Origins of spiral wave meander and breakup in a two-dimensional cardiac tissue model.* Ann Biomed Eng, 2000. **28**(7): p. 755-71.

58. Burton, R.A.B., et al., *Optical control of excitation waves in cardiac tissue.* Nature Photonics, 2015. **9**: p. 813.

59. Majumder, R., et al., *Optogenetics enables real-time spatiotemporal control over spiral wave dynamics in an excitable cardiac system.* eLife, 2018. **7**: p. e41076.

60. Tran, D.X., et al., *Vulnerability to re-entry in simulated two-dimensional cardiac tissue: Effects of electrical restitution and stimulation sequence.* Chaos: An Interdisciplinary Journal of Nonlinear Science, 2007. **17**(4): p. 043115.

61. Akar, F.G. and D.S. Rosenbaum, *Transmural electrophysiological heterogeneities underlying arrhythmogenesis in heart failure.* Circ Res, 2003. **93**(7): p. 638-45.

62. Laurita, K.R. and D.S. Rosenbaum, *Interdependence of modulated dispersion and tissue structure in the mechanism of unidirectional block.* Circ Res, 2000. **87**(10): p. 922-8.

63. Restivo, M., W.B. Gough, and N. el-Sherif, *Ventricular arrhythmias in the subacute myocardial infarction period. High-resolution activation and refractory patterns of reentrant rhythms.* Circ Res, 1990. **66**(5): p. 1310-27.

64. Kalin, A., et al., *Cardiac Arrhythmia: A Simple Conceptual Framework.* Trends in Cardiovascular Medicine, 2010. **20**(3): p. 103-107.

65. January, C.T. and H.A. Fozzard, *Delayed afterdepolarizations in heart muscle: mechanisms and relevance.* Pharmacol Rev, 1988. **40**(3): p. 219-27.

66. Kimura, S., et al., *Delayed afterdepolarizations and triggered activity induced in feline Purkinje fibers by alpha-adrenergic stimulation in the presence of elevated calcium levels.* Circulation, 1984. **70**(6): p. 1074-82.

67. Tse, G., *Mechanisms of cardiac arrhythmias.* Journal of arrhythmia, 2016. **32**(2): p. 75-81.

68. Cheng, H., et al., *Calcium sparks and [Ca2+]i waves in cardiac myocytes.* Am J Physiol, 1996. **270**(1 Pt 1): p. C148-59.

69. Cheng, H., W.J. Lederer, and M.B. Cannell, *Calcium sparks: elementary events underlying excitation-contraction coupling in heart muscle.* Science, 1993. **262**(5134): p. 740-4.

70. Nivala, M., et al., *Criticality in intracellular calcium signaling in cardiac myocytes.* Biophys J, 2012. **102**(11): p. 2433-42.

71. Song, Z., et al., *Calcium-voltage coupling in the genesis of early and delayed afterdepolarizations in cardiac myocytes.* Biophys J, 2015. **108**(8): p. 1908-21.

72. Halkin, A., et al., *Pause-dependent torsade de pointes following acute myocardial infarction: a variant of the acquired long QT syndrome.* J Am Coll Cardiol, 2001. **38**(4): p. 1168-74.

73. Huang, X., et al., *Spontaneous initiation of premature ventricular complexes and arrhythmias in type 2 long QT syndrome.* American Journal of Physiology - Heart and Circulatory Physiology, 2016. **311**(6): p. H1470-H1484.

74. Kim, T.Y., et al., *Complex excitation dynamics underlie polymorphic ventricular tachycardia in a transgenic rabbit model of long QT syndrome type 1.* Heart Rhythm, 2015. **12**(1): p. 220-8.

75. Roden , D.M., *Long-QT Syndrome.* New England Journal of Medicine, 2008. **358**(2): p. 169-176.

76. Napolitano, C., et al., *Sudden Cardiac Death and Genetic Ion Channelopathies.* Circulation, 2012. **125**(16): p. 2027-2034.

77. Giudicessi, J.R., A.A.M. Wilde, and M.J. Ackerman, *The genetic architecture of long QT syndrome: A critical reappraisal.* Trends in Cardiovascular Medicine, 2018. **28**(7): p. 453-464.

78. Dutta, S., et al., *Early afterdepolarizations promote transmural reentry in ischemic human ventricles with reduced repolarization reserve.* Progress in Biophysics and Molecular Biology, 2016. **120**(1–3): p. 236-248.

79. Maruyama, M., et al., *Genesis of phase 3 early afterdepolarizations and triggered activity in acquired long-QT syndrome.* Circ Arrhythm Electrophysiol, 2011. **4**(1): p. 103-11.

80. Zeng, J. and Y. Rudy, *Early afterdepolarizations in cardiac myocytes: mechanism and rate dependence.* Biophysical journal, 1995. **68**(3): p. 949-964.

81. Tran, D.X., et al., *Bifurcation and Chaos in a Model of Cardiac Early Afterdepolarizations.* Physical Review Letters, 2009. **102**(25): p. 258103.

82. Qu, Z., et al., *Early afterdepolarizations in cardiac myocytes: beyond reduced repolarization reserve.* Cardiovasc Res, 2013. **99**(1): p. 6-15.

83. Xie, Y., et al., *So little source, so much sink: requirements for afterdepolarizations to propagate in tissue.* Biophysical journal, 2010. **99**(5): p. 1408-1415.

84. Myles, R.C., et al., *Local β-Adrenergic Stimulation Overcomes Source-Sink Mismatch to Generate Focal Arrhythmia.* Circulation Research, 2012. **110**(11): p. 1454-1464.

85. Noble, D., *A modification of the Hodgkin--Huxley equations applicable to Purkinje fibre action and pace-maker potentials.* The Journal of physiology, 1962. **160**(2): p. 317-352.

86. Wilders, R., H.J. Jongsma, and A.C. van Ginneken, *Pacemaker activity of the rabbit sinoatrial node. A comparison of mathematical models.* Biophysical journal, 1991. **60**(5): p. 1202-1216.

87. Courtemanche, M., R.J. Ramirez, and S. Nattel, *Ionic mechanisms underlying human atrial action potential properties: insights from a mathematical model.* Am J Physiol, 1998. **275**(1 Pt 2): p. H301-21.

88. Stewart, P., et al., *Mathematical models of the electrical action potential of Purkinje fibre cells.* Philos Trans A Math Phys Eng Sci, 2009. **367**(1896): p. 2225-55.

89. Ten Tusscher, K.H., R. Hren, and A.V. Panfilov, *Organization of ventricular fibrillation in the human heart.* Circ Res, 2007. **100**(12): p. e87-101.

90. Luo, C.H. and Y. Rudy, *A model of the ventricular cardiac action potential. Depolarization, repolarization, and their interaction.* Circ Res, 1991. **68**(6): p. 1501-26.

91. Mahajan, A., et al., *A rabbit ventricular action potential model replicating cardiac dynamics at rapid heart rates.* Biophys J, 2008. **94**(2): p. 392-410.

92. O'Hara, T., et al., *Simulation of the undiseased human cardiac ventricular action potential: model formulation and experimental validation.* PLoS Comput Biol, 2011. **7**(5): p. e1002061.

93. Qu, Z. and A. Garfinkel, *An advanced numerical algorithm for solving partial differential equation in cardiac conduction.* IEEE Trans. Biomed. Eng., 1999. **49**(9): p. 1166-1168.

94. Helm, P.A., et al., *Ex vivo 3D diffusion tensor imaging and quantification of cardiac laminar structure.* Magnetic Resonance in Medicine, 2005. **54**(4): p. 850-859.

95. Wang, V.Y., et al., *Modelling passive diastolic mechanics with quantitative MRI of cardiac structure and function.* Medical Image Analysis, 2009. **13**(5): p. 773-784.

96. Streeter, D.D., Jr., et al., *Fiber orientation in the canine left ventricle during diastole and systole.* Circ Res, 1969. **24**(3): p. 339-47.

97. Behradfar, E., A. Nygren, and E.J. Vigmond, *The Role of Purkinje-Myocardial Coupling during Ventricular Arrhythmia: A Modeling Study.* PLOS ONE, 2014. **9**(2): p. e88000.

98. Berenfeld, O. and J. Jalife, *Purkinje-Muscle Reentry as a Mechanism of Polymorphic Ventricular Arrhythmias in a 3-Dimensional Model of the Ventricles.* Circulation Research, 1998. **82**(10): p. 1063-1077.

99. Romero, D., et al., *Effects of the Purkinje System and Cardiac Geometry on Biventricular Pacing: A Model Study.* Annals of Biomedical Engineering, 2010. **38**(4): p. 1388-1398.

100. Vergara, C., et al., *A coupled 3D–1D numerical monodomain solver for cardiac electrical activation in the myocardium with detailed Purkinje network.* Journal of Computational Physics, 2016. **308**: p. 218-238.

Chapter 2: A dynamical threshold for cardiac delayed afterdepolarization-mediate triggered activity

Abstract

Ventricular myocytes are excitable cells whose voltage threshold for action potential (AP) excitation is around -60 mV at which I_{Na} is activated to give rise to a fast upstroke. Therefore, for a short stimulus pulse to elicit an AP, a stronger stimulus is needed if the resting potential lies further away from the I_{Na} threshold, such as in hypokalemia. However, for an AP elicited by a long duration stimulus or a diastolic spontaneous calcium release, we observed that the stimulus needed was lower in hypokalemia than in normokalemia in both computer simulations and experiments of rabbit ventricular myocytes. This observation provides insight into why hypokalemia promotes calcium-mediated triggered activity, despite the resting potential lying further away from the I_{Na} threshold. To understand the underlying mechanisms, we performed bifurcation analyses and demonstrated that there is a dynamical threshold, resulting from a saddle-node bifurcation mainly determined by I_{K1} and I_{NCX}. This threshold is close to the voltage at which I_{K1} is maximum, and lower than the I_{Na} threshold. After exceeding this dynamical threshold, the membrane voltage will automatically depolarize above the I_{Na} threshold due to the large negative slope of the I_{K1}-V curve. This dynamical threshold becomes much lower in hypokalemia, especially with respect to calcium, as predicted by our theory. Because of the saddle-node bifurcation, the system can automatically depolarize even in the absence of I_{Na} to voltages higher than the $I_{Ca,L}$ threshold, allowing for triggered APs in single myocytes with complete I_{Na} block. However, since I_{Na} is important for AP propagation in tissue, blocking I_{Na} can still suppress premature ventricular excitations in cardiac tissue caused by calcium-mediated triggered activity. This suppression is more effective in normokalemia than in hypokalemia due to the difference in dynamical thresholds.

Introduction

Under normal conditions, ventricular myocytes have a diastolic resting potential around -80 mV, stabilized by the inward rectifier K^+ current (I_{K1}). An action potential (AP) can be elicited by a brief current pulse, overcoming the stabilizing effect of I_{K1} and bringing the voltage to the threshold (~-60 mV) for Na^+ current (I_{Na}) activation. In other words, the voltage threshold for eliciting an AP using a brief stimulus pulse is near the I_{Na} threshold around -60 mV for a ventricular myocyte. Therefore, when the resting potential is hyperpolarized (e.g., under hypokalemic conditions), a larger stimulus current for a brief pulse is needed to depolarize the membrane voltage to the I_{Na} threshold to elicit an AP. Similarly, the conduction velocity (CV) in cardiac tissue is slower for a hyperpolarized resting potential [1-3]. The resting potential of a ventricular myocyte can also be destabilized by reduction of I_{K1} to result in pacemaking activity [4, 5] or delayed afterdepolarization (DAD)-mediated triggered activity (TA) [6-8]. In both cases, a lowered I_{K1} allows the Na^+-Ca^{2+} exchange current (I_{NCX}) to overcome the repolarizing effect of I_{K1}, depolarizing the cell to the I_{Na} threshold for AP generation.

A DAD is a voltage depolarization caused by spontaneous calcium (Ca^{2+}) release (SCR) during the diastolic phase following a previous AP [9-13]. If the depolarization is large enough to reach the I_{Na} threshold, the DAD can trigger an AP causing TA. This phenomenon is potentiated by various diseased conditions including heart failure [7, 14] and hypokalemia [15]. In heart failure, ryanodine receptors (RyRs) become leaky, which promotes SCRs resulting in DADs. In addition, I_{K1} is reduced and I_{NCX} is increased, which decreases the diastolic Ca^{2+}-to-voltage gain to promote TA.

In hypokalemia, multiple factors come into play. Na^+-K^+ pump activity is reduced which results in an elevated intracellular Na^+ concentration [16, 17]. This inhibits forward Na^+-Ca^{2+} exchange, which increases intracellular Ca^{2+} concentration and promotes SCR. Hypokalemia also causes a reduced I_{K1} conductance, which tends to destabilize the resting potential and potentiates DAD-mediated TA. However, hypokalemia also causes a hyperpolarized resting potential through the left-shift of reversal potential E_K. This acts to move the membrane voltage further away from the I_{Na} threshold, which would seem to counter the TA promoting effect of reduced I_{K1}.

A recent theoretical study by Greene and Shiferaw [18] showed that the voltage threshold for DAD-mediated TA is actually lower than the I_{Na} threshold, and is determined by the voltage at which I_{K1} is maximal. These findings indicate that the traditional understanding of the voltage threshold for DAD-mediated TA as the voltage threshold for I_{Na} activation needs to be revisited. In this study, we seek to dissect the determinants of the threshold for DAD-mediated TA in normokalemic and hypokalemic conditions, using patch clamp experiments, computer simulations, and nonlinear dynamics. We show that there exists a dynamical threshold for TA, which is a saddle-node bifurcation point, mainly determined by I_{K1} and I_{NCX}. This threshold becomes lower in hypokalemia, potentiating DAD-mediated TA in hypokalemia.

Methods

Myocyte experiments

Ventricular myocyte isolation. Young adult (3-4 months of age) New Zealand white male rabbits (1.7–2.0 kg) were euthanized by intravenous injection of heparin sulfate (1000 U) and sodium pentobarbital (100 mg/kg). Hearts were quickly excised by thoracotomy and retrogradely perfused at 37 °C in Langendorff fashion with Ca^{2+}-free Tyrode's solution for 5-7 minutes followed by enzyme digestion perfusion with Tyrode's solution containing 0.05 mg/mL Liberase TH (Roche, South San Francisco, CA) for 20-30 minutes at 25 mL/min. The Tyrode's solution contained the following (in mmol/L): 136 NaCl, 5.4 KCl, 0.33 NaH_2PO_4, 1.0 $MgCl_2$, 10 HEPES, and 10 glucose (pH 7.4 with KOH). All chemicals were purchased from Sigma-Aldrich (St. Louis, MO) unless indicated otherwise. Myocytes were separated from digested ventricles by gentle mechanical dissociation in 0.2 mM Ca^{2+} Tyrode's solution. Ca^{2+} concentration was gradually increased to 1.8 mmol/L over 30 min. Myocytes were used within 6-8 hours. All procedures complied with UCLA Animal Research Committee policies.

Patch clamp experiments in myocytes. Standard whole-cell patch clamp methods were used to measure voltage in the current clamp mode. Borosilicate glass electrodes (tip resistance 1.4-2.2 MΩ) were filled with internal solution containing (in mmol/L) 110 K-Aspartate, 30 KCl, 5 NaCl, 10 HEPES, 5 MgATP, 5 creatine phosphate, 1 KH_2PO_4, and 0 EGTA (pH 7.2 with KOH). All chemicals were purchased from Sigma unless indicated otherwise. Data were acquired with an Axopatch 200A patch-clamp amplifier and Digidata 1200 acquisition board driven by pCLAMP

9.0 software (Axon Instruments, Inc., Union City, CA). Corrections were made for liquid junction potentials. Signals were filtered at 1 kHz. All experiments were carried out in Tyrode's solution maintained at 37°C. Constant current square pulses (2 ms or 200 ms duration) were applied step-wise in 0.1 nA increments from -0.2 nA up to 3.0 nA to determine AP thresholds under normokalemic ($[K^+]_o$ = 5.4 mM) or hypokalemic ($[K^+]_o$ = 2.7 mM) conditions. For experiments involving Na^+ channel blockade, patch-clamped myocytes were rapidly superfused with either normal Tyrode's solution or Tyrode's solution containing 20 µmol/L tetrodotoxin (TTX) (Tocris Bioscience, Bristol, UK) using a rapid solution exchange device [19] positioned near the myocyte under the control of Axopatch software.

Computer simulations

Computer simulations were performed in a single cell and one-dimensional (1D) cables using the AP model previously described by Mahajan et al [20]. In the single cell simulations, the cell model was first pre-paced to its steady state. Spontaneous Ca^{2+} release were simulated by clamping the myocyte submembrane Ca^{2+} ($[Ca^{2+}]_s$) level to a Gaussian-like shape during the diastolic phase after an stimulated AP, i.e., $[Ca^{2+}]_s = Ca_{peak} \cdot e^{-\frac{(t-t_0)^2}{2\sigma^2}}$, where t_0 is the peak time of $[Ca^{2+}]_s$ (t was set to zero at the time of the stimulation, see Fig.2-1), σ determines the width of the Ca^{2+} transient, and Ca_{peak} is the peak $[Ca^{2+}]_s$ value. σ = 150 ms and t_0 = 850 ms were used for all simulations unless otherwise specified. Submembrane Ca^{2+} was used to determine Ca^{2+} thresholds to produce a DAD of sufficient amplitude to cause TA, since the I_{NCX} dependence

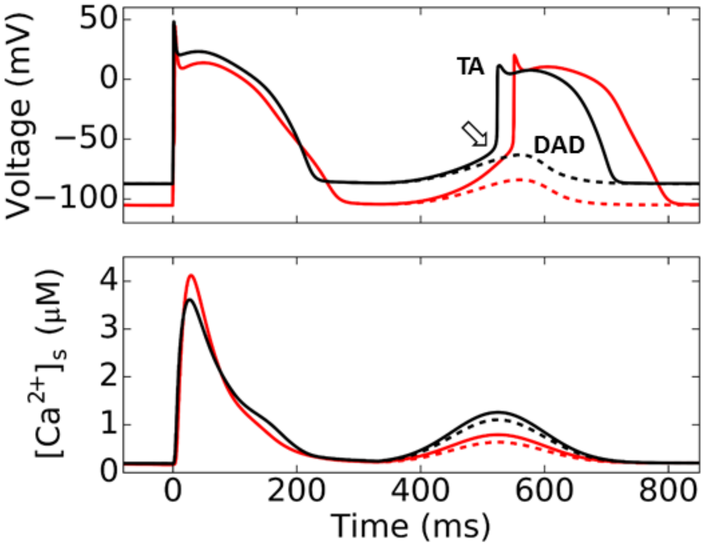

Figure 2-1. Simulated DAD and TA using the AP model.

Membrane voltage (upper traces) and submembrane Ca^{2+} concentration ($[Ca^{2+}]_s$, lower traces) during a normal stimulated AP followed by a DAD due to spontaneous Ca^{2+} release which is just above (solid lines) or below (dashed lines) the threshold to trigger an AP. The black traces are for normokalemia ($[K^+]_o$=5.4 mM), and the red ones are for hypokalemia ($[K^+]_o$=2.7 mM). Open arrow indicates the I_{Na} threshold. The parameters for Gaussian-like function of the clamped spontaneous Ca^{2+} release (see Methods) were t_0 = 525 ms and σ = 70 ms for all four traces. For normokalemia, Ca_{peak}= 1.258 µM (black solid) and 1.102 µM (black dashed), respectively. For hypokalemia, Ca_{peak} = 0.790 µM (red solid) and 0.634 µM (red dashed).

on Ca^{2+} is specifically formulated in terms of submembrane Ca^{2+}. Normokalemia and hypokalemia were simulated by changing the value of $[K^+]_o$ from 5.4 mM to 2.7 mM. Intracellular sodium ($[Na^+]_i$) was clamped to 10 mM.

1D cable simulations were carried out using the following equation for voltage

$$\frac{\partial V}{\partial t} = -I_{ion}/C_m + D\left(\frac{\partial^2 V}{\partial x^2}\right) \qquad (1)$$

where V is the membrane voltage, C_m=1 µF/cm^2 is the membrane capacitance, and D is the diffusion constant set to 0.0005 cm^2/ms. The pre-paced single-cell steady state was used as initial condition for each cell in the cable. DADs were simulated by a time-dependent commanded spontaneous release of the SR Ca^{2+} with random latencies drawn from a Gaussian distribution with a certain standard deviation as described previously [21, 22]. Briefly, a SR release conductance was added with a certain strength and duration to release Ca^{2+} from the SR. The onset of this release was determined by a random latency drawn from the Gaussian distribution. A time adaptive algorithm was used with a time step (Δt) varying between 0.01 ms and 0.1 ms. In the single cell simulations, DAD-mediated triggered activity was considered to have occurred if the voltage exceeded 0 mV. In the cable simulations, if a propagating wave was detected at either end of the cable after the sinus beat, a propagating premature ventricular contraction (PVC) was considered to have occurred.

Results

Hypokalemia results in a lower threshold for DAD-mediated TA in a ventricular myocyte model

We carried out simulations to examine the threshold for TA in the rabbit ventricular myocyte model by Mahajan et al [20]. The spontaneous Ca^{2+} release that cause a DAD or TA was simulated by a clamped Ca^{2+} transient (see Methods). Fig.2-1 shows the voltage and $[Ca^{2+}]_s$ for a stimulated beat followed by a spontaneous Ca^{2+} release just below (dashed) and above (solid) the threshold for TA. Hypokalemia hyperpolarized the resting membrane potential to below -100 mV. Despite the resting potential being 20 mV more negative, the Ca^{2+} amplitude threshold for DAD-mediated TA is much lower during hypokalemia than normokalemia, indicating that hypokalemia substantially lowered the threshold for TA. This is consistent with well-known experimental observations that hypokalemia potentiates DAD-mediated TA despite hyperpolarizing the resting membrane potential [15]. The voltage still needs to eventually depolarize past the I_{Na} threshold to result in a fast upstroke under both normokalemia and hypokalemia. However, in the case of hypokalemia, a much smaller Ca^{2+} transient and thus a much smaller I_{NCX} was sufficient to depolarize the voltage to the same I_{Na} threshold. To gain a more complete understanding of the mechanisms underlying this phenomenon, we combined nonlinear dynamics analysis with computer simulations and patch clamp experiments as described in the sections below.

Short and long current pulse thresholds for eliciting an AP

Since the duration of a DAD is much longer than that of a typical electrical stimulus, we first studied the role that the duration of a pulse stimulus plays in eliciting an AP. Fig. 2-2 compares excitation thresholds for a short (2 ms) versus a long (200 ms) current pulse to elicit an AP in a patch-clamped rabbit ventricular myocyte (current clamp mode) under both normokalemic ($[K]_o$=5.4 mM) and hypokalemic conditions ($[K]_o$=2.7 mM). Hypokalemia shifted the resting potential from -87 mV to -110 mV.

For the 2 ms current pulse (Fig.2-2A and B), the minimum current required to elicit an AP increased from 1.6 nA under normokalemic conditions to 2.1 nA under hypokalemic conditions, as expected due to the more hyperpolarized resting membrane potential during hypokalemia. In both cases, the smallest current amplitude eliciting an AP depolarized the membrane very close to the I_{Na} threshold of -60 mV, followed by the AP upstroke within 5 ms. For the 200 ms current pulse (Fig.2-2C and D), however, the results were reversed, with the minimum current eliciting an AP decreasing from 0.6 nA during normokalemia to 0.5 nA during hypokalemia. Moreover, the smallest current amplitude eliciting an AP initially depolarized the membrane voltage to only -74 mV for normokalemia and -94 mV for hypokalemia. The membrane voltage then rose very slowly before finally reaching the I_{Na} activation threshold at

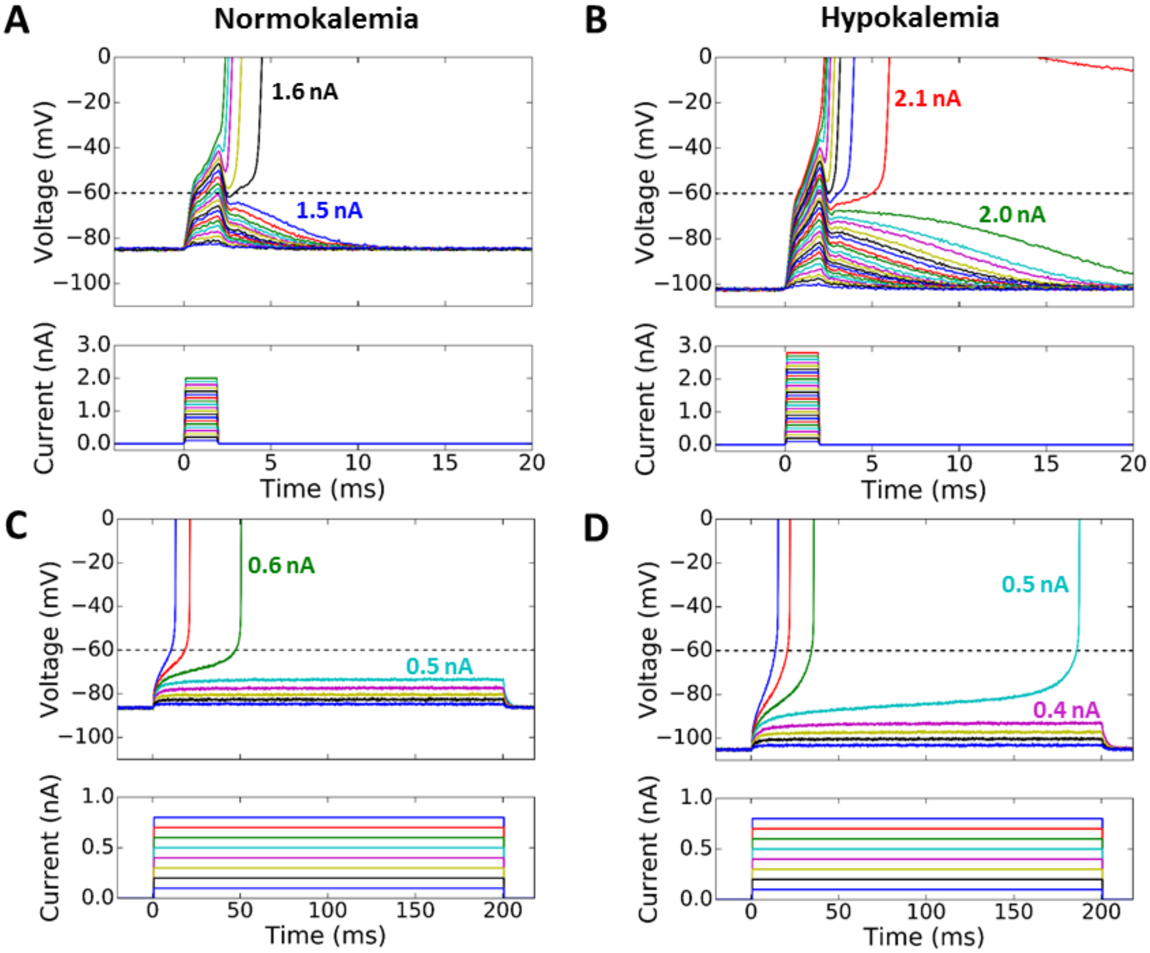

Figure 2-2. Current thresholds for triggering an AP by short and long stimuli in normokalemic ($[K^+]_o$=5.4 mM) and hypokalemic ($[K^+]_o$=2.7 mM) rabbit ventricular myocytes.

A. Superimposed voltage (upper) and current (lower) traces during 2 ms current pulses of increasing amplitude in a normokalemic patch clamped rabbit ventricular myocyte. The minimum current needed to elicit an AP was 1.6 nA. **B**. Same as A but during hypokalemia. With a hyperpolarized resting potential, the minimum current needed to elicit an AP increased to 2.1 nA. **C-D.** Corresponding traces for 200 ms current pulses. The minimum current needed to elicit an AP was 0.6 nA, which decreased to 0.5 nA during hypokalemia. Note how the take-off potential is lower than the I_{Na} activation threshold at -60 mV, and is further lowered in hypokalemia.

approximately -60 mV to generate the AP upstroke. Thus, consistent with the predictions from Greene and Shiferaw [18], the threshold for a long current pulse to elicit an AP was considerably more negative than -60 mV, especially during hypokalemia.

To analyze the dynamics underlying these behaviors, we considered a system composed only of I_{K1} and the stimulus current (I_{sti}), described by the following differential equation:

$$\frac{dV}{dt} = -(I_{K1} + I_{sti})/C_m \qquad (2)$$

where I_{sti} is a square pulse with a duration (τ) and height (I_0), i.e.,

$$I_{sti} = \begin{cases} -I_0, & 0 \le t \le \tau \\ 0, & t > \tau \end{cases} \qquad (3)$$

The resting potential of Eq.2 is simply the reversal potential (E_K) of I_{K1}. The voltage at the end of the stimulus current pulse ($t = \tau$) is given by

$$V(\tau) = \int_0^{\tau} -(I_{K1} - I_0)/C_m dt \qquad (4)$$

To facilitate analytical solutions of Eq.2 or Eq.4, we approximated I_{K1} by a piece-wise linear function as follows (Fig.2-3A):

$$I_{K1} = \begin{cases} \alpha(V - E_K), & V < V_{max} \\ \beta(V_0 - V), & V_{max} \le V \le V_0 \\ 0 & V > V_0 \end{cases} \qquad (5)$$

where $\alpha = \frac{I_{K1,max}}{V_{max} - E_K}$ and $\beta = \frac{I_{K1,max}}{V_0 - V_{max}}$. $I_{K1,max}$ is the peak I_{K1} at V_{max}. V_{max} and V_0 are defined as in Fig.2-3A.

When $I_0 < I_{K1,max}$, Eq.4 can be explicitly solved, which leads to

$$V(\tau) = E_K + \frac{I_0}{\alpha} - \frac{I_0}{\alpha} e^{-\frac{\alpha\tau}{C_m}} \qquad (6)$$

For an infinitely long pulse, the voltage reaches a steady state, which is given by

$$V(\tau \rightarrow \infty) = E_K + \frac{I_0}{\alpha} < V_{max} \qquad (7)$$

When $I_0 > I_{K1,max}$, the solution of Eq.2 can be expressed with three time regions as follows:

For $t < t'$,

$$V(t) = E_K + \frac{I_0}{\alpha} - \frac{I_0}{\alpha} e^{-\frac{\alpha t}{C_m}} \qquad (8)$$

with t’ as the time at which $V(t') = V_{max}$, obtained from Eq.8 as

$$t' = -\frac{C_m}{\alpha} ln \frac{-(V_{max} - E_K - \frac{I_0}{\alpha})\alpha}{I_0} \qquad (9)$$

2) For $t' < t < t''$,

$$V(t) = V_0 - \frac{I_0}{\beta} + (V_{max} - V_0 + \frac{I_0}{\beta}) e^{\frac{\beta(t-t')}{C_m}} \qquad (10)$$

with t” as the time at which $V(t'') = V_0$, obtained from Eq.10 as

$$t'' = t' + \frac{C_m}{\beta} ln \frac{\frac{I_0}{\beta}}{V_{max} - V_0 + \frac{I_0}{\beta}} \qquad (11)$$

3) For $t > t''$,

$$V(t) = V_0 + I_0(t - t'')/C_m \qquad (12)$$

Since the I_{Na} threshold ($V_{th,Na}$) is near -60 mV, which is higher than V_{max} but lower than V_0 (see Fig.2-3A), then only the cases where $t < t''$ need to be considered. Assume that at $t = \tau$, the voltage reaches the I_{Na} threshold, i.e., $V(\tau) = V_{th,Na}$. Eq. 10 then becomes

$$V_{th,Na} = V_0 - \frac{I_{0,th}}{\beta} + (V_{max} - V_0 + \frac{I_{0,th}}{\beta}) e^{\frac{\beta(\tau-t')}{C_m}} \qquad (13)$$

which leads to

$$\tau = t' + \frac{C_m}{\beta} ln \frac{V_{th,Na} - V_0 + \frac{I_{0,th}}{\beta}}{V_{max} - V_0 + \frac{I_{0,th}}{\beta}} \qquad (14)$$

By inserting t' from Eq.9 to Eq.14, one obtains

$$\tau = \frac{C_m}{\beta} ln \frac{V_{th,Na} - V_0 + \frac{I_{0,th}}{\beta}}{V_{max} - V_0 + \frac{I_{0,th}}{\beta}} - \frac{C_m}{\alpha} ln \frac{-(V_{max} - E_K - \frac{I_{0,th}}{\alpha})\alpha}{I_{0,th}} \qquad (15)$$

By setting $\tau = \infty$ in Eq.15 (this can only be satisfied if the second logarithmic term goes to infinity), the minimum stimulus strength can be calculated as

$$I_{0,th} = \alpha\,(V_{max} - E_K) = I_{K1,max} \qquad (16)$$

Therefore, when $I_{0,th} < I_{K1,max}$, the voltage can never reach $V_{th,Na}$ but rather asymptotically approaches the steady state (Eq.7), which is always lower than V_{max}. However, when $I_{0,th} > I_{K1,max}$, there always exists a finite τ during which the voltage can grow to reach $V_{th,Na}$.

Hypokalemia has three main effects on I_{K1}: a left-shift of E_K, a left-shift of V_{max}, and a reduced $I_{K1,max}$ as shown in Fig.2-3A.

In Fig.2-3B, we plot the threshold current $I_{0,th}$ versus the pulse duration τ using Eq.15 for both normokalemia and hypokalemia, showing that $I_{0,th}$ is smaller for normokalemia than for hypokalemia when τ < 29 ms, which is reversed when τ > 29 ms. We also plot in Fig.2-3B the corresponding results (circles) from the computer simulation using the rabbit ventricular myocyte model, which agrees well with the theoretical prediction. Figs.2-3C and D show two

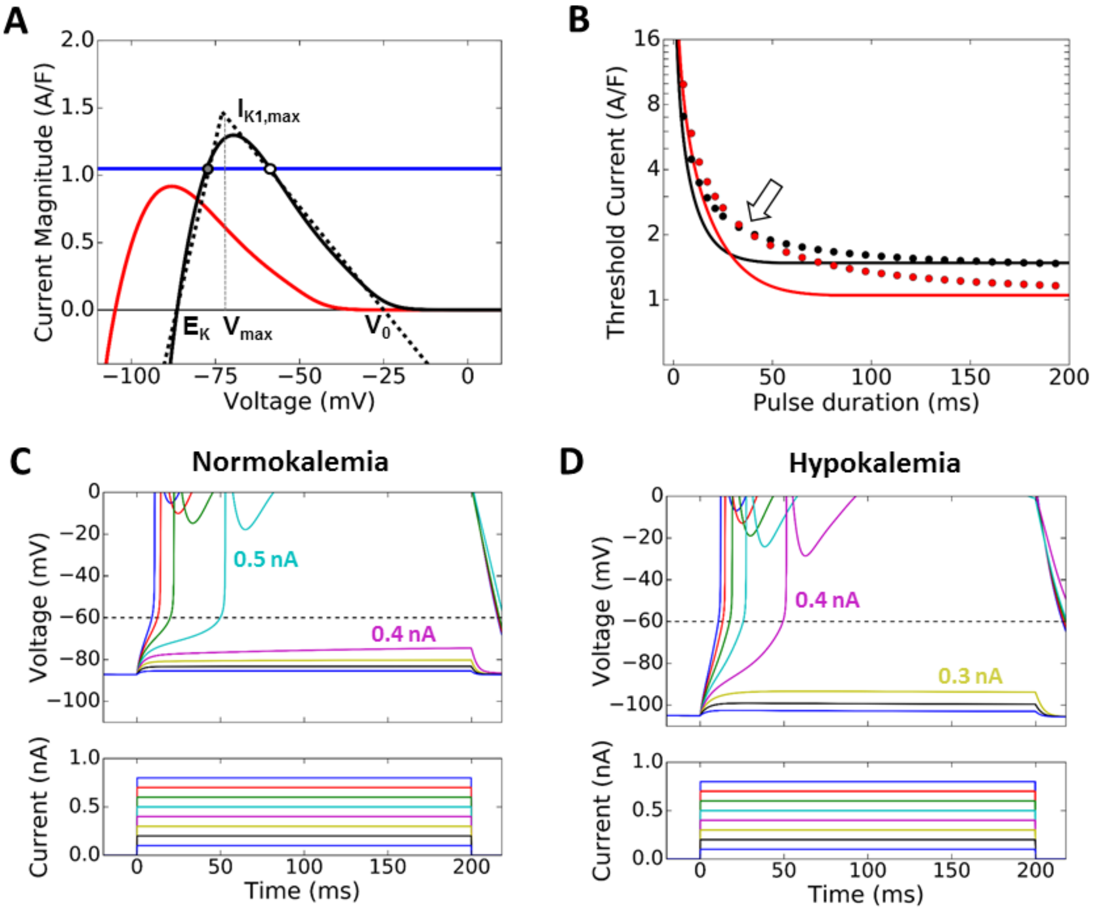

Figure 2-3. Theoretical analysis of the current threshold for triggering an AP by a pulse stimulus.

A. The I_{K1}-V curves for normokalemia ($[K^+]_o$=5.4 mM, black) and hypokalemia ($[K^+]_o$=2.7 mM, red). The I_{K1} curve is mainly determined by 4 parameters: E_K, $I_{K1,max}$, V_{max}, and V_0. To most closely match the actual I_{K1} curves, for normokalemia we used E_K = -86.5 mV, $I_{K1,max}$ = 1.47 A/F, V_{max} = -73 mV, and V_0 = -25 mV. For hypokalemia, we used E_K = -104.5 mV, $I_{K1,max}$ = 1.04 A/F, V_{max} = -92 mV, and V_0 = -43 mV in the linear piecewise approximation for I_{K1} (dotted line) used for the analytical treatment. The blue horizontal line represents an example constant inward current that is subthreshold in normokalemia but suprathreshold in hypokalemia. Circles are the points at which the net current is zero, i.e., the equilibrium points. The solid circle marks a stable equilibrium point and the open circle is an unstable equilibrium point in normokalemia. In hypokalemia, this example has no equilibrium point. **B**. The threshold current ($I_{0,th}$) versus pulse duration (τ) from the theoretical prediction (lines), and from the simulations (dots) using the AP model with a constant stimulus pulse of varying duration in normokalemia (black) and hypokalemia (red). The open arrow points to where the current threshold reverses between normokalemia and hypokalemia. **C-D**. Voltage (upper) and current (lower) traces corresponding to 200 ms current pulses of increasing amplitude during normokalemia and hypokalemia, from the simulations using the AP model. The minimum current needed to elicit an AP was 0.5 nA, which decreased to 0.4 nA in simulated hypokalemia. Note again how the takeoff potential is lower than the I_{Na} activation threshold, and is further lowered in hypokalemia.

examples of incremental current amplitudes with a 200 ms pulse duration to illustrate the threshold current in normokalemia ($[K^+]_o$ = 5.4 mM) and hypokalemia ($[K^+]_o$ = 2.7 mM).

Based on Eqs.15 and 16, the threshold current $I_{0,th}$ to elicit an AP depends on the voltage threshold of the Na^+ channel ($V_{th,Na}$) for a short stimulus pulse but not for a long pulse. This indicates that in the absence of Na^+ current (I_{Na}), a larger $I_{0,th}$ is required to elicit an AP for a short pulse since the voltage threshold ($V_{th,Ca}$) for L-type Ca^{2+} channel is higher (around -40 mV). For a long pulse, $I_{0,th}$ will remain unchanged since Eq.16 is independent of either $V_{th,Na}$ or $V_{th,Ca}$. To demonstrate this experimentally, we performed patch clamp experiments as in Fig.2-2 by blocking the Na^+ channel using TTX (Fig.2-4). For a 2 ms stimulation pulse, the addition of TTX increased the current threshold from 1.8 nA to 2.5 nA (Figs.2-4 A and B). However, for a 200 ms stimulation pulse, the addition of TTX did not change the current threshold, which remained at 0.7 nA before and after TTX addition (Figs.2-4 C and D), agreeing with the theoretical prediction. Note that after TTX application, the turning points for steep upstroke occurred at higher voltages and the maximum upstroke slopes were reduced under both short and long pulses (see corresponding dV/dt plots in the insets). This indicates that TTX was effective in blocking the Na^+ channel and the AP upstroke after TTX was mediated by the L-type Ca^{2+} current ($I_{Ca,L}$). Based on our theory, this same observation should hold true for hypokalemia. However, the TTX effect of blocking the Na^+ channel is voltage dependent, which becomes less effective for lower pre-holding voltages [23-25]. Because of this voltage dependent behavior, we were not able to convincingly repeat this experimental protocol in hypokalemia.

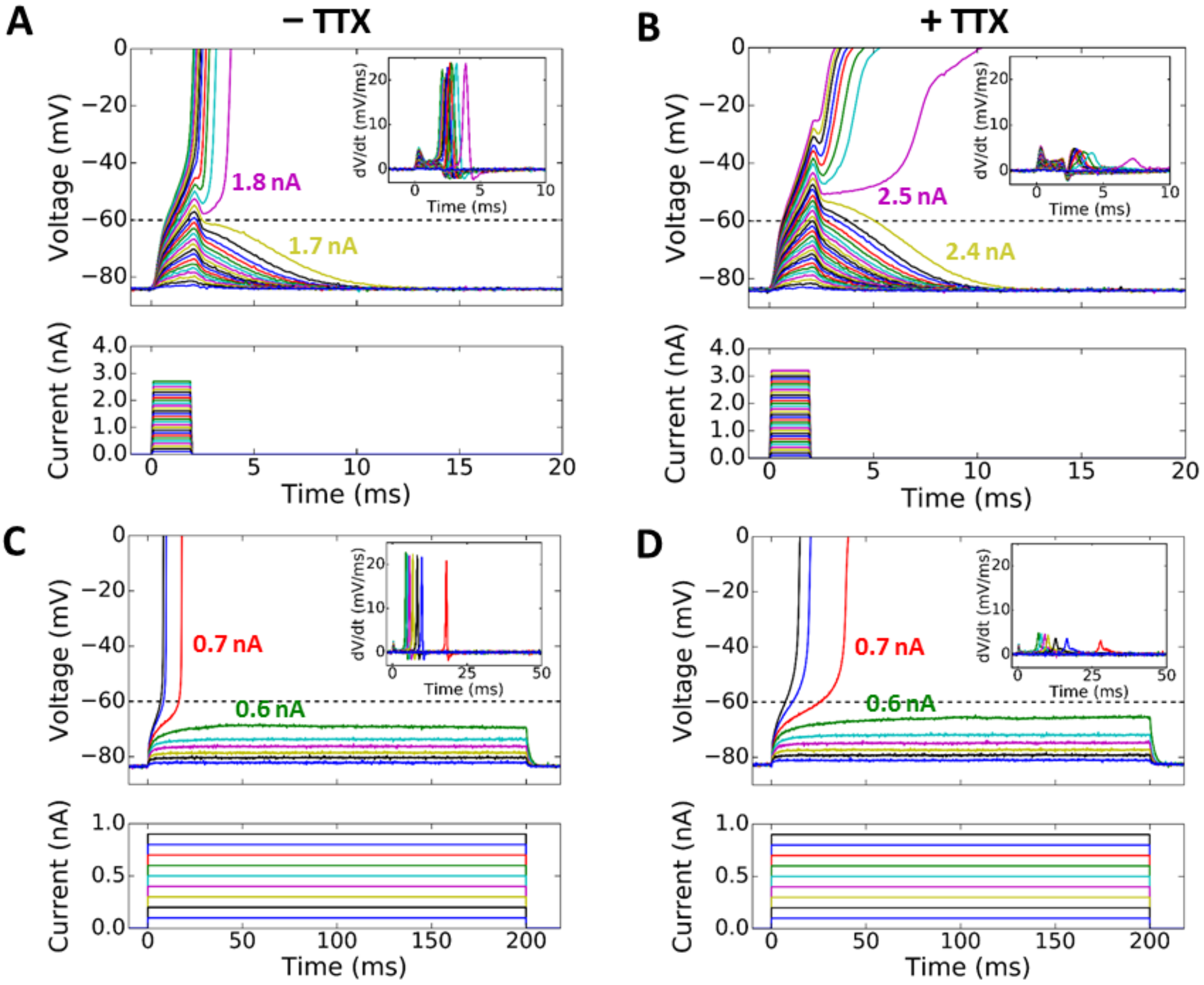

Figure 2-4. Current thresholds for triggering an AP by short and long stimuli with and without TTX.

A. Superimposed voltage (upper) and current (lower) traces during 2 ms current pulses of increasing amplitude in a normokalemic patch clamped rabbit ventricular myocyte (repeat of the protocol in Fig2.A in a different cell). The minimum current needed to elicit an AP was 1.8 nA. The inset shows the rate of change of the voltage traces (dV/dt). **B**. Same as A but in the presence of 20 µM TTX. With the addition of TTX, the minimum current needed to elicit an AP increased to 2.5 nA. The inset shows a 4-fold reduction in maximum dV/dt due to TTX. **C-D.** Corresponding traces for 200 ms current pulses without and with TTX, respectively. The minimum current needed to elicit an AP was 0.7 nA in both cases, demonstrating no change in the current threshold by TTX. Again, the addition of TTX reduced the dV/dt.

Nonlinear dynamics caused by the interaction of I_{K1} and I_{NCX}

In contrast to constant current pulses, the depolarizing current I_{NCX} during a DAD is not constant, but a function of Na^+, Ca^{2+} and voltage. Therefore, the analysis for constant current pulses above provides important qualitative insights, but it is not sufficient for a detailed understanding of the mechanisms of DAD-mediated TA. Here we further analyze the nonlinear dynamical interactions between I_{K1} and I_{NCX} using the following equation:

$$\frac{dV}{dt} = -(I_{K1} + I_{NCX})/C_m \qquad (17)$$

For simplicity, we first assume Na^+ and Ca^{2+} to be constant parameters instead of changing variables, and thus Eq.17 is a nonlinear equation with respect to voltage only. At equilibrium, $\frac{dV}{dt} = 0$, which leads to

$$I_{K1} = -I_{NCX} \qquad (18)$$

i.e., when the magnitudes of the two currents are equal, the system is at an equilibrium point.

Since the currents involved are nonlinear functions of voltage, multiple equilibria can exist. Fig.2-5A plots the I-V curves for I_{K1} and inverted I_{NCX} ($-I_{NCX}$), in which the intersections of the two curves are the equilibrium points. When Ca^{2+} is low, I_{NCX} is small and there is only one intersection close to the reverse potential of I_{K1} (E_K). The net current is inward when voltage is more negative than the equilibrium point and outward when voltage is more positive (top panel in Fig.2-5B). Therefore, if the voltage is displaced away from the equilibrium voltage, it is automatically driven back toward the equilibrium point, and thus the equilibrium point is stable. As Ca^{2+} rises, the $-I_{NCX}$ curve increases and shifts to the right, resulting in three

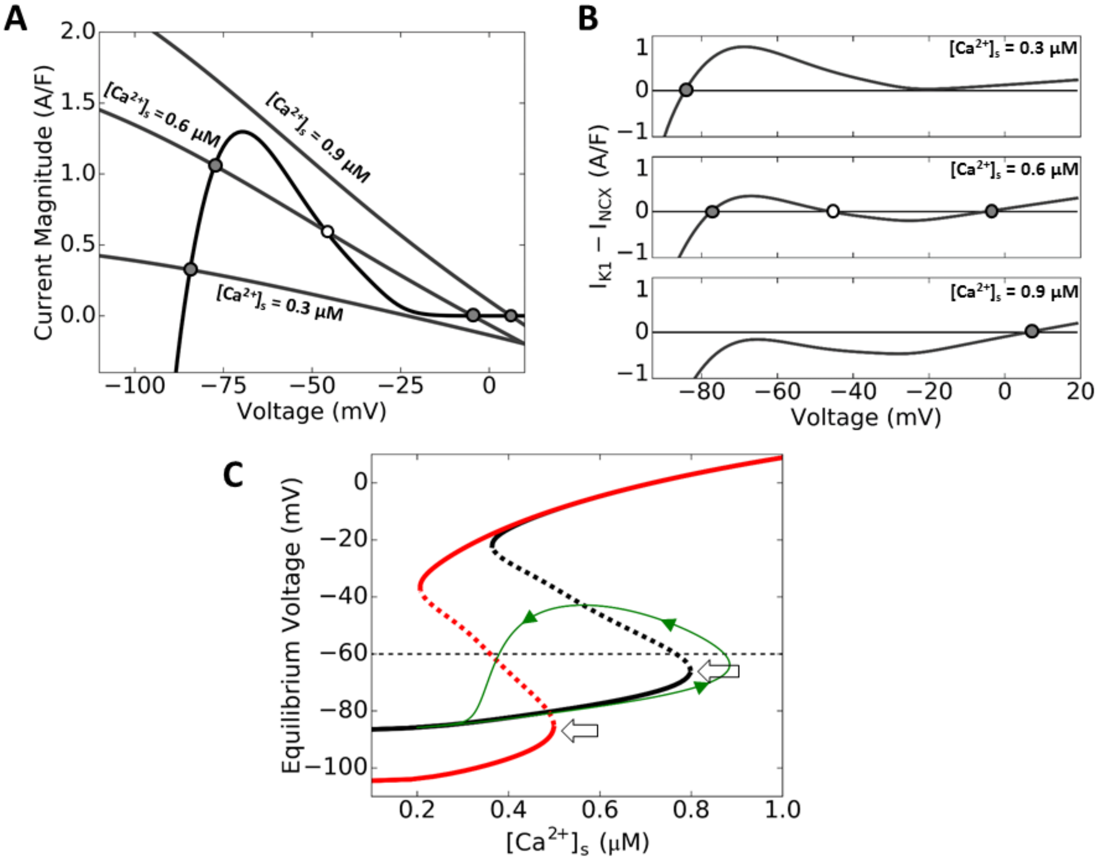

Figure 2-5. A dynamical threshold determined by I_{K1} and I_{NCX} for a constant Ca^{2+} conditions.

A. I-V plot of I_{K1} and $-I_{NCX}$ at $[K]_o$ = 5.4 mM (normokalemia), corresponding to low (0.3 μM), medium (0.6 μM), and high (0.9 μM) submembrane Ca^{2+} concentration levels. The solid circles are stable equilibrium points and the open circle is an unstable equilibrium point. Note how with low Ca^{2+} there is only one (stable) equilibrium point at low voltage, with medium Ca^{2+} there are three (stable-unstable-stable) equilibrium points, and with high Ca^{2+} there is only one (stable) equilibrium point at high voltage. **B**. Net current versus voltage for the corresponding three cases in A, using the same symbols for the equilibrium points. **C**. Equilibrium voltage versus steady-state Ca^{2+} during normokalemia (black) and hypokalemia (red). Solid lines indicate stable equilibrium points and dashed lines unstable equilibrium points for the particular Ca^{2+} concentration. Arrows indicate the respective dynamical thresholds, which determine the voltage and Ca^{2+} needed to cross the saddle-node and elicit an AP. The green trace is an example of a simulated trajectory using the simple two-current system consisting of I_{K1} and I_{NCX}, with a Ca^{2+} transient simulated by a Gaussian-shaped function similar to the function described in Fig.1. Note that voltage continues to increase for a period of time even after the Ca^{2+} concentration has started to decrease, due to crossing the dynamical threshold.

equilibrium points. The total net current changes from inward to outward, then to inward, and to outward again as voltage increases (middle panel in Fig.2-5B). Thus the lower and upper equilibrium points are stable while the middle is unstable. As Ca^{2+} rises above a critical level, the lower equilibria points converge then vanish, leaving only the single stable high voltage equilibrium point remaining. This behavior is summarized in Fig.2-5C by plotting the equilibrium voltages of this two-current system versus Ca^{2+} concentration, with the stable equilibrium points plotted as a solid line and unstable points as a dashed line. Therefore, when Ca^{2+} exceeds a critical value (arrows in Fig.2-5C), the membrane voltage will automatically depolarize towards the remaining single equilibrium point at high voltage. This occurs because of the steep negative slope of the I_{K1}-V curve in this region causing I_{K1} to decrease faster than $-I_{NCX}$ as voltage increases, making the net current always inward thereby depolarizing the membrane voltage further. The voltage at the critical point, which occurs where the $-I_{NCX}$ curve lies exactly tangent to I_{K1} slightly above V_{max}, is lower than the I_{Na} threshold. Therefore, once the voltage reaches this critical value, it will continue to rise. We call this critical voltage a *dynamical threshold* since it is determined by the nonlinear dynamics of the interaction between I_{K1} and I_{NCX}. The dynamical threshold is a bifurcation point called a saddle-node bifurcation point [26]. Hypokalemia results in a lower voltage threshold (red line in Fig.2-5C) due to the left-shift of the I_{K1}-V curve and reduction of maximum I_{K1} conductance.

Influence of the intracellular Ca^{2+} waveform during spontaneous Ca^{2+} release on AP activation

The nonlinear dynamics shown in Fig.2-5 is valid when Ca^{2+} is constant, but during a DAD, cytosolic Ca^{2+} concentration rises and then falls. As Ca^{2+} increases from the diastolic Ca^{2+} concentration, the system first follows the lower branch of equilibrium voltage. When Ca^{2+}

increases past the critical value (arrows in Fig.2-5C), voltage will continue to increase even when Ca^{2+} is declining (green trajectory in Fig.2-5C). Therefore, whether a cell reaches the I_{Na} threshold to trigger an AP depends not only on crossing the dynamical threshold, but also on the rate of decay of Ca^{2+} influencing the I_{NCX} curve. To investigate the effects of Ca^{2+} decay on the TA threshold, we varied the duration of a clamped Ca^{2+} transient with a Gaussian-like shape by changing the width of full width at half-maximum (FWHM). Fig.2-6A shows the Ca^{2+} transient amplitude threshold for TA (i.e. the peak amplitude of the Ca^{2+} transient required to trigger an AP) versus the width of the Ca^{2+} transient for different values of $[K^+]_o$. The Ca^{2+} transient amplitude threshold for TA decreased with lower $[K^+]_o$ or a wider Ca^{2+} transient which decays more slowly. The dependence of the Ca^{2+} threshold on Ca^{2+} transient width gradually saturates when the Ca^{2+} transient FWHM is greater than about 200 ms. This indicates that when the Ca^{2+} transient duration is 200 ms or longer, the system has reached the steady state solution, closely agreeing with the prediction of the bifurcation analysis, when including I_{NaK} which contributes about 20% to the effective I_{K1} peak (dashed lines in Fig.2-6A). The FWHM was observed in rabbit ventricular myocytes to be 180-300 ms [27], which easily satisfies this condition and therefore are always in the regime of the dynamical threshold.

As I_{NCX} and I_{NaK} both depend on the intracellular Na^+ concentration of the myocyte, we investigated the effect of $[Na^+]_i$ on the TA threshold. Fig. 2-6B shows that lower $[Na^+]_i$ lowers the TA threshold, while higher $[Na^+]_i$ increases the threshold. This can be explained by the two diastolic currents that $[Na^+]_i$ affects: I_{NaK} and I_{NCX}. At higher $[Na^+]_i$, I_{NaK} contributes to a slightly higher effective I_{K1} peak through the I_{NaK} contribution, while I_{NCX} is reduced. Both of these factors would serve to make TA more difficult, requiring a higher Ca^{2+} trasient amplitude. With

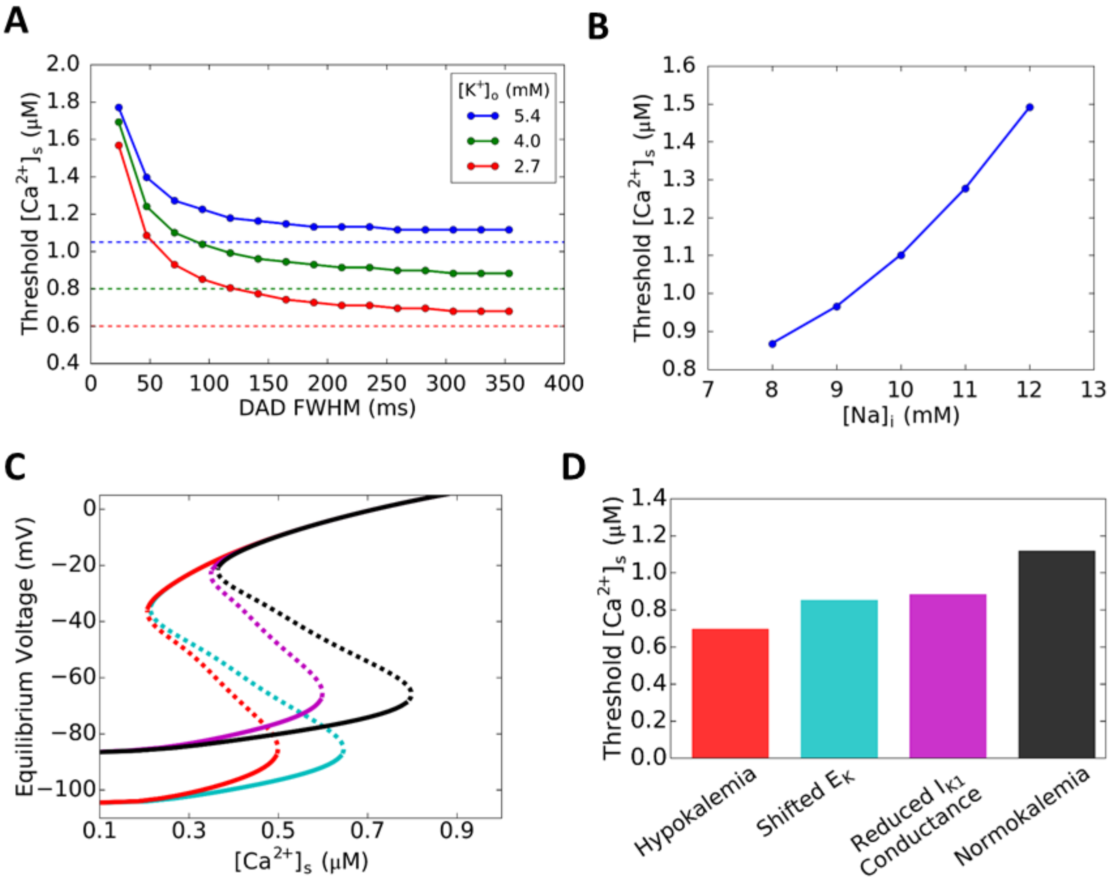

Figure 2-6. Submembrane Ca^{2+} transient thresholds for TA.

A. Ca^{2+} amplitude threshold for TA versus the full width at half maximum (FWHM) of the Ca^{2+} transient and DAD for three different $[K]_o$ (5.4 mM blue, 4.0 mM green, and 2.7 mM red). Dashed lines are the theoretical thresholds predicted using a three-current (I_{K1}, I_{NCX}, and I_{NaK}) system, with I_{NaK} adding a small quantitative increase in the outward current. Since the Ca^{2+} transient is a Gaussian function instead of a constant value, the Ca^{2+} threshold at steady state is slightly above the theoretically predicted values. **B.** Ca^{2+} amplitude threshold for TA versus the intracellular Na^+ concentration $[Na^+]_i$. Lower $[Na^+]_i$ values result in a lower Ca^{2+} threshold. **C**. Equilibrium voltage versus steady state Ca^{2+} concentration under different conditions: control (black); reduced I_{K1} only (magenta); left-shifted E_K only (cyan); and hypokalemia (red). Note how the dynamical threshold shifts with each condition. **D.** Ca^{2+} threshold results from simulations using the AP model under the same conditions in C. Both the left-shift of E_K as well as the reduced I_{K1} peak conductance lower the Ca^{2+} threshold to elicit an AP. This can be predicted by the different dynamical thresholds in each condition as seen in C.

lower $[Na^+]_i$ the opposite occurs, with I_{NaK} resulting in a slightly lower effective I_{K1} peak with increased I_{NCX}, allowing TA to occur more easily at a lower Ca^{2+} trasient amplitude. Note that these simulations only studied the effect of changing $[Na^+]_i$ with a given Ca^{2+} transient, and did not take into account any Ca^{2+} loading effects caused by the changes in $[Na^+]_i$.

Finally, to sort out the effects of lowered resting potential and reduced I_{K1} conductance caused by hypokalemia, we carried out simulations under four conditions: 1) control (normokalemia); 2) reduced I_{K1} conductance only; 3) left-shift of I_{K1} through E_K only, and 4) both reduced I_{K1} conductance and left-shift of E_K (hypokalemia). Fig. 2-6C shows the steady-state equilibrium voltage versus Ca^{2+} obtained using the simple system described by only I_{K1} and I_{NCX} (Eq.17), which shows that the reduction of I_{K1} conductance and the left-shift of E_K alone both resulted in similar lowered Ca^{2+} and voltage dynamical thresholds to elicit an AP. These predictions agreed with our simulation results (Fig. 2-6D) using the AP model.

TA and PVC suppression by blocking I_{Na}

The theoretical analyses above and experiments shown in Fig. 2-4 suggest that even in the absence of I_{Na}, the voltage will depolarize automatically beyond the $I_{Ca,L}$ threshold near -40 mV to elicit an AP as long as the Ca^{2+} amplitude and duration exceed the dynamical threshold. This implies that blocking I_{Na} may not be effective in suppressing TA. To demonstrate this effect, we carried out simulations in a single isolated myocyte by reducing the maximum conductance of I_{Na} from 12 mS/μF (the control value) to zero and determined the corresponding Ca^{2+} transient amplitude threshold for TA (Fig. 2-7A). For normokalemia, the Ca^{2+}

threshold increased slightly as g_{Na} was reduced from 12 to 6 mS/μF (the Ca^{2+} threshold was increased from 1.1 μM to 1.25 μM), then exhibited a faster increase as g_{Na} was reduced from 6 to 3 mS/μF (the Ca^{2+} threshold was increased from 1.25 μM to 1.6 μM), and then saturated as g_{Na} was finally reduced from 3 to 0 mS/μF. For hypokalemia ($[K^+]_o$=2.7 mM), the Ca^{2+} threshold remained almost the same until g_{Na} was reduced to 4 mS/μF from which the Ca^{2+} threshold was increased abruptly from 0.7 μM to 1.8 μM and then saturated. In both cases, the rapid increase in Ca^{2+} threshold as I_{Na} conductance decreases indicates the transition from a I_{Na}-mediated upstroke to a slower $I_{Ca,L}$-mediated upstroke, since it takes more time to reach the $I_{Ca,L}$ threshold. Fig. 2-7B show AP and Ca^{2+} traces when $I_{Na} = 0$.

Although these results demonstrated that I_{Na} is not necessary for TA in single myocytes, whether this is also true for TA mediated PVCs in tissue was still unclear. To investigate the effect of I_{Na} block in cardiac tissue, we simulated a cable of 500 coupled myocytes with a central region of 40 cells exhibiting DADs of the same Ca^{2+} release strength but with different random latencies drawn from a Gaussian distribution (see Ref. [22]) for more details of the method), as in Fig. 2-8A. For the control g_{Na} value (12 mS/μF), the conduction velocity (CV) for AP conduction is ~0.05 cm/ms for normokalemia and 0.042 cm/ms for hypokalemia, which decreases as g_{Na} is lowered until $g_{Na} = 3$ mS/μF, after which conduction completely fails (Fig. 2-8B). As expected, hypokalemia reduces excitability and thus slows conduction.

We then calculated the probability of a PVC occurring in the cable at different levels of g_{Na} in normokalemia and hypokalemia (Fig. 2-8C). For control g_{Na} with this distribution of Ca^{2+} release strengths, the probability of PVC is about 65% in normokalemia but almost 100% in hypokalemia. In normokalemia, the probability of PVC decreased as I_{Na} decreased, which drops

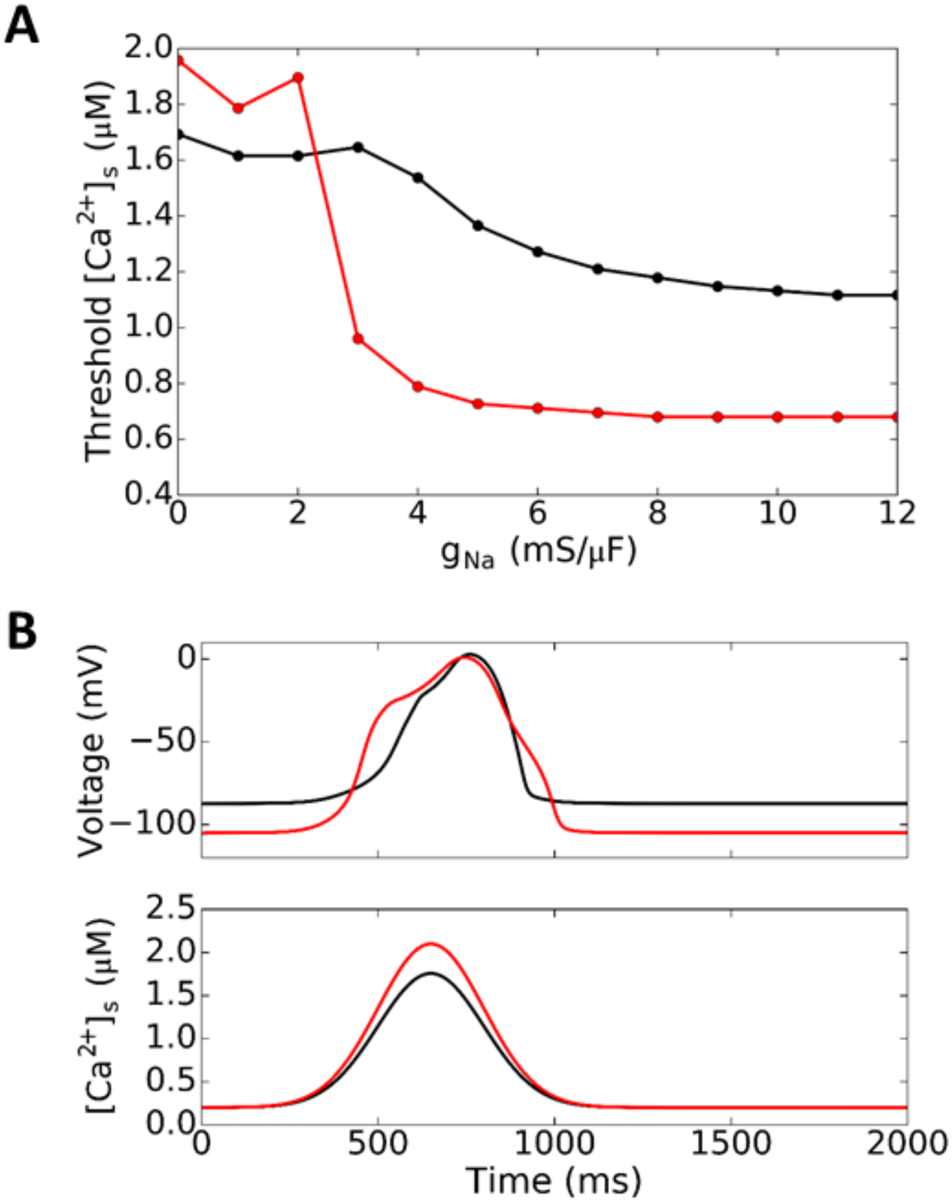

Figure 2-7. Effects of I_{Na} blockade on TA in a single isolated myocyte.

A. Submembrane Ca^{2+} transient threshold for TA versus g_{Na} in normokalemia (black) and hypokalemia (red). For most g_{Na} values, the Ca^{2+} threshold for TA is lower in hypokalemia than in normokalemia. **B**. Voltage and Ca^{2+} traces for Ca^{2+} transients just above threshold with $g_{Na} = 0$, under normokalemic (black) and hypokalemic conditions (red). Due to the dynamical threshold automatically driving the voltage to the $I_{Ca,L}$ threshold, we still can elicit a slow upstroke AP with complete I_{Na} block.

to near zero at g_{Na} = 3 mS/μF. In hypokalemia, however, the probability of PVC exhibited almost no change until g_{Na} was reduced to 3 mS/μF and then dropped rapidly to zero at g_{Na} = 2 mS/μF. In both cases, the probability of PVC became zero only when I_{Na} is too small (g_{Na} = 2 mS/μF) to support conduction at all in the cable (Fig. 2-8B). Note that we used the same Ca^{2+} release strength for both hypokalemia and normokalemia, and since the Ca^{2+} threshold in hypokalemia is much lower than in normokalemia, the peak Ca^{2+} values were already much higher than the TA threshold in hypokalemia. Because of this, the Ca^{2+} transient in hypokalemia is strong enough to depolarize the voltage in the DAD region above the threshold for TA no matter how much I_{Na} is available, as long as there is enough I_{Na} strength for successful conduction (g_{Na} > 2 mS/μF). If one used a lower Ca^{2+} release strength distribution, the probability of PVC would have a stronger dependence on $I_{Na,}$ as shown in the normokalemia case. Therefore, at the tissue-scale, blocking I_{Na} can still suppress Ca^{2+}-mediated PVCs as long as the Ca^{2+} transient is not much higher than the Ca^{2+} threshold for TA.

Discussion

In this study, we investigated the voltage threshold for eliciting an AP by current pulses and DADs in ventricular myocytes. We show that a short current pulse must provide enough charge movement to directly depolarize the membrane potential to the I_{Na} threshold near -60 mV to elicit a rapid AP upstroke. Therefore, when the resting potential is hyperpolarized and lies further away from the I_{Na} threshold, such as during hypokalemia, a stronger stimulus is required to elicit an AP, i.e. the excitability of a myocyte is reduced and conduction velocity in tissue is slower [1-3]. However, during a long current pulse or a DAD, the threshold for triggering an AP is different. While the membrane voltage must eventually reach the I_{Na} threshold to

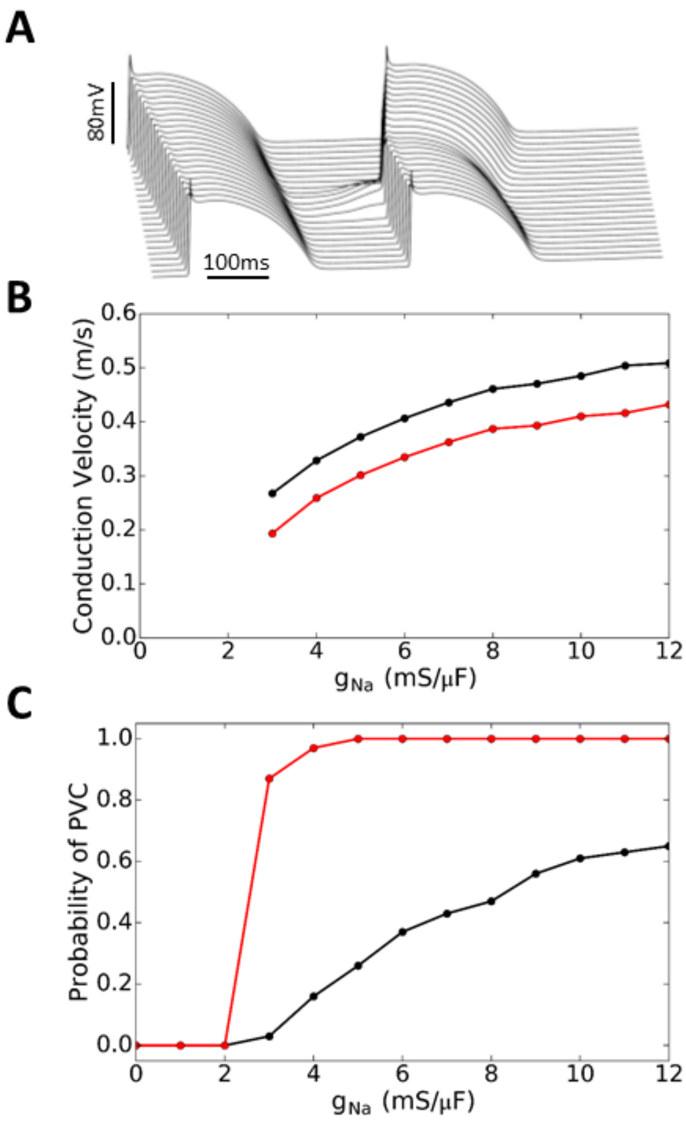

Figure 2-8. **Suppression of PVCs in tissue by I_{Na} blockade**.

A. Representative voltage traces for a 1D cable of 200 cells with a region of 40 cells in the center exhibiting DADs with a release strength g_{spon} = 0.250 ms^{-1} whose random latencies were drawn from a Gaussian distribution with time to onset $t_{0,onset}$ = 300 ms and standard deviation $\sigma_{latency}$ = 50 ms. (See ref (22) for method details. Note that in (22) t_0 corresponds to the Ca release onset, not the Ca release peak as in this paper.) This particular example shows a paced beat propagating through the entire cable, followed by the central region exhibiting suprathreshold DADs that trigger a propagating PVC. **B**. Conduction velocity versus g_{Na} for normokalemia (black) and hypokalemia (red). Conduction failure occurs for $g_{Na} < 3$ mS/μF. **C**. The probability of PVC occurring in the cable (100 random simulations per data point,) versus g_{Na} for normokalemia (black) and hypokalemia (red). For a fixed strength of spontaneous Ca^{2+} release in the DAD region, the probability of PVCs gradually decreased with lowered g_{Na} in normokalemia, but remained high in hypokalemia until conduction failure occurred.

trigger a rapid AP upstroke, the true threshold for TA is a dynamical threshold. In the case of a DAD, this dynamical threshold is mainly determined by I_{K1} and I_{NCX} (with I_{NaK} adding a small quantitative contribution, ~20% of the effective peak I_{K1}) manifesting as a saddle-node bifurcation in which the dynamical threshold is the bifurcation point. The dynamical threshold occurs at a lower voltage than the I_{Na} threshold during both normokalemia and hypokalemia. Once intracellular Ca^{2+} rises and activates sufficient I_{NCX} to depolarize the myocyte past the dynamical threshold, the voltage continues to automatically depolarize to above the I_{Na} threshold due to a steep negative slope of I_{K1}-V curve. Thus, despite

decreased excitability in response to short current pulses, DAD-mediated TA is facilitated by hypokalemia due to the lower dynamical threshold. The nonlinear dynamical analysis shows that the lower dynamical threshold results from a reduced I_{K1} conductance, a well-known factor that promotes (DAD)-mediated TA [6-8], and from a left-shift of $E_{K,}$ such that a smaller Ca^{2+} transient is able to induce TA. Thus, the lower dynamical threshold interacts synergistically with another key effect of hypokalemia, Na^+-K^+ pump inhibition causing intracellular Ca^{2+} overload [16, 17] and spontaneous diastolic Ca^{2+} release, to promote DAD-mediated TA. Since the voltage can automatically depolarize above the I_{Na} threshold to reach $I_{Ca,L}$ threshold after passing the saddle-node bifurcation point (or the dynamical threshold), triggered APs can occur in single myocytes in the absence of I_{Na}, suggesting that blocking I_{Na} may not be effective at suppressing TA. However, since I_{Na} is important for AP propagation in tissue, blocking I_{Na} can still suppress PVCs in cardiac tissue caused by Ca^{2+}-mediated TA.

Our findings expand on the previous work of Greene and Shiferaw [18], who demonstrated analytically that the threshold for AP excitation caused by a steady state constant current pulse is lower than the I_{Na} threshold near the voltage at which I_{K1} is maximum. In addition to experimentally validating this prediction in isolated myocytes and extending the findings to hypokalemia, we performed a detailed analysis of the nonlinear dynamics for DAD-mediated TA by considering a simple system incorporating the two currents most important in determining diastolic voltage, i.e., the I_{K1}-I_{NCX} system. We showed that the two-current system can exhibit bistability and undergoes a saddle-node bifurcation which determines the dynamical threshold. Besides the existence of a dynamical threshold, the nonlinear dynamics also predicts the following:

Once the voltage is above the dynamical threshold, the Ca^{2+} concentration does not necessarily need to increase further to depolarize the voltage to the I_{Na} threshold. The voltage can still automatically depolarize further even if Ca^{2+} decreases during this phase (Fig. 2-5C), as long as the rate of decrease in I_{NCX} is not faster than the decrease in I_{K1} as voltage rises to the I_{Na} threshold.

The position of the upper equilibrium point is an important factor governing the automatic phase of depolarization beyond the dynamical threshold, affecting the efficiency at which the myocyte reaches the I_{Na} or $I_{Ca,L}$ threshold. Note that in the constant stimulus current case as analyzed in this study and by Greene and Shiferaw [18], the upper equilibrium point does not exist. The upper equilibrium is mainly determined by I_{NCX}. It is obvious that the higher the upper equilibrium, the easier for the system to depolarize to the I_{Na} or $I_{Ca,L}$ threshold. For example, increasing the magnitude of I_{NCX} (by simply increasing the I_{NCX} amplitude) has little effect on elevating the upper equilibrium point (although it can have an effect on lowering the dynamical threshold) because this only tilts the I_{NCX} curve more steeply to affect the saddle-node bifurcation point. In contrast, increasing Ca^{2+} concentration can have a large effect on both the dynamical threshold and the upper equilibrium point, because in addition to tilting I_{NCX}, a larger Ca^{2+} also shifts the I_{NCX} curve to the right, increasing the margin between the I_{NCX} and I_{K1} curves. This steep tilt and right-shift of I_{NCX} effectively makes it easier to depolarize the voltage above the I_{Na} or $I_{Ca,L}$ threshold. Similarly, reducing I_{K1} conductance can also lower the dynamical threshold but will have little effect on the upper equilibrium point.

In conclusion, using nonlinear dynamics and patch clamp experiments, we have demonstrated the existence of a dynamical threshold for DAD-mediated TA, which is lower than the I_{Na} threshold. The dynamical threshold is further lowered by hypokalemia, facilitating DAD-mediated TA by hypokalemia. Our dynamical analysis and computer simulation have demonstrated distinct roles of Ca^{2+}, I_{K1}, I_{NCX}, as well as I_{Na} in potentiating DAD-mediated TA, which not only provide important insights into the mechanism of DAD-mediated TA but also useful information for future development of antiarrhythmic therapies.

References

1. Kagiyama, Y., J.L. Hill, and L.S. Gettes, *Interaction of acidosis and increased extracellular potassium on action potential characteristics and conduction in guinea pig ventricular muscle.* Circ Res, 1982. **51**(5): p. 614-23.
2. Shaw, R.M. and Y. Rudy, *Electrophysiologic effects of acute myocardial ischemia: A mechanistic investigation of action potential conduction and conduction failure.* Circ. Res., 1997. **80**(1): p. 124-138.
3. Xie, Y., et al., *Effects of fibroblast-myocyte coupling on cardiac conduction and vulnerability to reentry: A computational study.* Heart Rhythm, 2009. **6**(11): p. 1641-9.
4. Miake, J., E. Marban, and H.B. Nuss, *Biological pacemaker created by gene transfer.* Nature, 2002. **419**(6903): p. 132-3.
5. Silva, J. and Y. Rudy, *Mechanism of Pacemaking in IK1-Downregulated Myocytes.* Circulation Research, 2003. **92**(3): p. 261-263.
6. Schlotthauer, K. and D.M. Bers, *Sarcoplasmic reticulum Ca(2+) release causes myocyte depolarization. Underlying mechanism and threshold for triggered action potentials.* Circ Res, 2000. **87**(9): p. 774-80.
7. Pogwizd, S.M., et al., *Arrhythmogenesis and contractile dysfunction in heart failure: Roles of sodium-calcium exchange, inward rectifier potassium current, and residual beta-adrenergic responsiveness.* Circ Res, 2001. **88**(11): p. 1159-67.
8. Maruyama, M., et al., *Diastolic intracellular calcium-membrane voltage coupling gain and postshock arrhythmias: role of purkinje fibers and triggered activity.* Circ Res, 2010. **106**(2): p. 399-408.
9. Rosen, M.R., J.P. Moak, and B. Damiano, *The clinical relevance of afterdepolarizations.* Ann N Y Acad Sci, 1984. **427**: p. 84-93.
10. January, C.T. and H.A. Fozzard, *Delayed afterdepolarizations in heart muscle: mechanisms and relevance.* Pharmacol Rev, 1988. **40**(3): p. 219-27.
11. Marban, E., S.W. Robinson, and W.G. Wier, *Mechanisms of arrhythmogenic delayed and early afterdepolarizations in ferret ventricular muscle.* J Clin Invest, 1986. **78**(5): p. 1185-92.
12. ter Keurs, H.E.D.J. and P.A. Boyden, *Calcium and Arrhythmogenesis.* Physiol. Rev., 2007. **87**(2): p. 457-506.
13. Katra, R.P. and K.R. Laurita, *Cellular mechanism of calcium-mediated triggered activity in the heart.* Circ Res, 2005. **96**(5): p. 535-42.

14. Yeh, Y.H., et al., *Calcium-handling abnormalities underlying atrial arrhythmogenesis and contractile dysfunction in dogs with congestive heart failure.* Circ Arrhythm Electrophysiol, 2008. **1**(2): p. 93-102.

15. Morita, H., et al., *Mechanism of U wave and polymorphic ventricular tachycardia in a canine tissue model of Andersen-Tawil syndrome.* Cardiovasc Res, 2007. **75**(3): p. 510-8.

16. Pezhouman, A., et al., *Molecular Basis of Hypokalemia-Induced Ventricular Fibrillation.* Circulation, 2015. **132**(16): p. 1528-1537.

17. Aronsen, J.M., et al., *Hypokalaemia induces Ca2+ overload and Ca2+ waves in ventricular myocytes by reducing Na+,K+-ATPase α2 activity.* The Journal of Physiology, 2015. **593**(6): p. 1509-1521.

18. Greene, D.A. and Y. Shiferaw, *Approximate analytical solutions for excitation and propagation in cardiac tissue.* Physical Review E, 2015. **91**(4): p. 042719.

19. Scaringi, J.A., et al., *A new method to detect rapid oxygen changes around cells: How quickly do calcium channels sense oxygen in cardiomyocytes?* Journal of Applied Physiology, 2013. **115**(12): p. 1855-1861.

20. Mahajan, A., et al., *A rabbit ventricular action potential model replicating cardiac dynamics at rapid heart rates.* Biophys. J., 2008. **94**(2): p. 392-410.

21. Xie, Y., et al., *So little source, so much sink: requirements for afterdepolarizations to propagate in tissue.* Biophys J, 2010. **99**(5): p. 1408-15.

22. Liu, M.B., et al., *Delayed afterdepolarizations generate both triggers and a vulnerable substrate promoting reentry in cardiac tissue.* Heart Rhythm, 2015. **12**(10): p. 2115-24.

23. Baer, M., P.M. Best, and H. Reuter, *Voltage-dependent action of tetrodotoxin in mammalian cardiac muscle.* Nature, 1976. **263**(5575): p. 344-345.

24. Cohen, C.J., et al., *Tetrodotoxin block of sodium channels in rabbit Purkinje fibers. Interactions between toxin binding and channel gating.* The Journal of General Physiology, 1981. **78**(4): p. 383-411.

25. Carmeliet, E., *Voltage-dependent block by tetrodotoxin of the sodium channel in rabbit cardiac Purkinje fibers.* Biophysical Journal, 1987. **51**(1): p. 109-114.

26. Strogatz, S.H., *Nonlinear dynamics and Chaos: with applications to physics, biology, chemistry, and engineering*. Studies in nonlinearity. 2000, Cambridge: Westview Press. xi, 498.

27. Ko, C.Y., et al., *Multiscale Consequences of Spontaneous Calcium Release on Cardiac Delayed Afterdepolarizations.* Biophysical Journal. **108**(2): p. 264a.

Chapter 3: Multiscale determinants of delayed afterdepolarization amplitude in cardiac tissue

Abstract

Spontaneous calcium (Ca) waves in cardiac myocytes underlie delayed afterdepolarizations (DADs) which trigger cardiac arrhythmias. How these subcellular/cellular events overcome source-sink factors in cardiac tissue to generate DADs of sufficient amplitude to trigger action potentials (APs) is not fully understood. Here, we evaluate quantitatively how factors at the subcellular scale (number of Ca wave initiation sites), cellular scale (sarcoplasmic reticulum (SR) Ca load) and tissue scale (synchrony of Ca release in populations of myocytes) determine DAD features in cardiac tissue using a combined experimental and computational modeling approach. Isolated patch-clamped rabbit ventricular myocytes loaded with Fluo-4 to image intracellular Ca were rapidly paced during exposure to elevated extracellular Ca (2.7 mmol/L) and isoproterenol (0.25 μmol/L) to induce diastolic Ca waves and subthreshold DADs. As the number of paced beats increased from 1 to 5, SR Ca content (assessed with caffeine pulses) increased, the number of Ca wave initiation sites increased, integrated Ca transients and DADs became larger and shorter in duration, and the latency period to the onset of Ca waves shortened with reduced variance. *In silico* analysis using a computer model of ventricular tissue incorporating these experimental measurements revealed that whereas all of these factors promoted larger DADs with higher probability of generating triggered activity, the latency period variance and SR Ca load had the greatest influences. Therefore, incorporating quantitative experimental data into tissue level simulations reveals that increased intracellular Ca promotes DAD-mediated triggered activity in tissue predominantly by increasing both the synchrony (decreasing latency variance) of Ca waves in nearby myocytes and SR Ca load, whereas the number of Ca wave initiation sites per myocyte is less important.

Introduction

Delayed afterdepolarizations (DADs) in cardiac tissue are transient depolarizations of the diastolic membrane voltage which can both trigger action potentials (APs) and generate a vulnerable substrate for reentrant arrhythmias [1]. They constitute a major arrhythmogenic mechanism in the settings of heart failure, catecholaminergic polymorphic ventricular tachycardia (CPVT), digitalis toxicity, and other conditions in which intracellular calcium (Ca) cycling becomes unstable [2, 3]. DADs are intimately linked to intracellular Ca waves originating from the subcellular Ca release unit (CRU) network in cardiac myocytes. CRUs consist of L-type Ca channels (LTCCs) in the t-tubule membrane apposed to ryanodine receptors (RyRs) at the sarcoplasmic reticulum (SR) membrane. Under conditions of Ca overload, groups of CRUs which spontaneously release SR Ca at one or more subcellular locations can initiate Ca waves that propagate regeneratively throughout the CRU network of the myocyte. The resulting increase in cytoplasmic free Ca stimulates Ca-sensitive inward currents, primarily the Na-Ca exchange current (I_{NCX}), which causes a transient membrane depolarization. If the DAD is large enough to reach the activation threshold for an AP, one or a series of APs called triggered activity (TA) can be elicited to initiate focal and/or reentrant arrhythmias [4-8].

The time course and amplitude of a DAD in an isolated myocyte is shaped by two components: 1) the time course and amplitude of the integrated whole-cell Ca transient caused by the underlying Ca wave(s) and 2) the sensitivity of the resting voltage to changes in intracellular Ca, the so-called diastolic Ca-voltage coupling gain [9]. The second component is determined by the difference between inward current densities of I_{NCX} and other Ca-sensitive currents promoting depolarization to outward current densities opposing depolarization, primarily the inward rectifier potassium (K) channel, I_{K1}, in ventricular muscle and the His-Purkinje system. The first component, on the other hand, is more complex. At the subcellular scale, the location and number of initiation sites of Ca waves is a key determinant of the amplitude, rate-of-rise, and duration of the whole-cell Ca transient. For example, a Ca wave originating from the center of a myocyte will release SR Ca in half the time of a Ca wave originating from one end of the cell (assuming the same propagation speed), producing an integrated whole-cell Ca transient with approximately twice the amplitude, rate-of-rise, and half the width. In general, as the number of initiation sites increases, the whole-cell Ca transient becomes larger in amplitude and shorter in duration. At the cellular scale, increases in SR Ca content augment the total amount of Ca released and wave propagation speed, also causing a larger and shorter integrated whole-cell Ca transient. Whereas these factors are clearly major determinants of whether a DAD reaches sufficient amplitude to trigger an AP in an isolated myocyte, at the tissue scale, source-sink (loading) factors also come into play [10-13]. Since each ventricular myocyte is coupled through gap junctions to an average of 11 other myocytes [14], a single myocyte exhibiting a Ca wave will be voltage-clamped by neighboring quiescent myocytes, attenuating the DAD amplitude by more than an order of magnitude. Only when a large number of myocytes in a region of tissue all develop Ca waves quasi-synchronously within an overlapping time window can the source-sink mismatch be overcome to generate a DAD of appreciable magnitude in the tissue [11-13, 15, 16]. Thus, after rapid pacing in cardiac tissue, the timing of Ca waves (i.e. the latency period, defined as the time interval between the last paced Ca transient and the onset of a spontaneous diastolic Ca wave) [16, 17] in populations of adjacent myocytes plays a key role. If the latency periods have a large variance, the Ca waves in the individual myocytes may not summate effectively to overcome the source-sink mismatch and generate a DAD of appreciable amplitude.

Although the subcellular, cellular, and tissue scale factors all contribute positively to the probability of a DAD triggering an AP in tissue as intracellular Ca load increases, the quantitative importance of each factor under experimentally-defined conditions has not, to the best of our knowledge, been rigorously analyzed. Thus, the novel goal of this study is to tackle this issue using a combined experimental and computational approach. Accordingly, we induced Ca waves and DADs by pacing isolated patch-clamped rabbit ventricular myocytes and measured the number of Ca wave initiation sites, SR Ca content, and latency to onset of Ca waves as the pacing train duration increased. We then incorporated these experimental data into simulated cardiac tissue. Our findings provide for the first time a quantitative analysis of the multiscale factors that increase the probability of a DAD generating TA in cardiac tissue, including the effects of tissue dimensionality and gap junction coupling.

Materials and Methods

Ventricular myocyte isolation

Young adult (3-4 months age) New Zealand white male rabbits (1.7–2.0 kg) were euthanized by an intravenous injection of heparin sulfate (1000 U) and sodium pentobarbital (100 mg/kg). Hearts were quickly excised by thoracotomy and retrogradely perfused at 37 °C in Langendorff fashion with Ca-free Tyrode’s solution for 5-7 minutes followed by enzyme digestion perfusion with Tyrode’s solution containing 0.05 mg/mL Liberase TH (Roche, South San Francisco, CA) for 20-30 minutes at 25 mL/min. The Tyrode’s solution contained the following (mmol/L): 136 NaCl, 5.4 KCl, 0.33 NaH_2PO_4, 1.0 $MgCl_2$, 10 HEPES, 10 glucose, and pH 7.4 with KOH. Myocytes were separated from digested ventricles by gentle mechanical dissociation in 0.2 mmol/L Ca Tyrode's solution. Ca concentration was gradually increased to 1.8 mmol/L over 30 min. Myocytes were used within 6-8 hours. All procedures complied with UCLA Animal Research Committee policies.

Patch clamp recordings

Standard whole-cell patch-clamp methods were used to measure voltage and current in the current clamp or voltage clamp mode, respectively, modified slightly from previously described methods [18]. Borosilicate glass electrodes (tip resistance 1.4-2.2 MΩ) were filled with internal solution containing (in mmol/L) 110 K-Aspartate, 30 KCl, 5 NaCl, 10 HEPES, 5 MgATP, 5 creatine phosphate, 1 KH_2PO_4, and 0 EGTA, and pH 7.2 adjusted with KOH. Fluo-4 pentapotassium salt (10 µmol/L) (Life Technologies, Carlsbad, CA) and the reducing agent glutathione (GSH) (10 mmol/L) were added to the internal solution to visualize Ca fluorescence activity while minimizing the effects of phototoxic damage. APs were elicited with square current pulses of 2 ms duration and twice threshold amplitude. DADs were evoked following rapid pacing trains of varying durations in the presence of Tyrode's solution with elevated Ca (2.7 mmol/L) and ISO (0.25 µmol/L). Data were acquired with an Axopatch 200A patch-clamp amplifier and Digidata 1200 acquisition board driven by pCLAMP 9.0 software (Axon Instruments, Inc., Union City, CA). Corrections were made for liquid junction potentials. Signals were filtered at 1 kHz. All experiments were carried out at 37°C. All chemicals were purchased from Sigma-Aldrich (St. Louis, MO) unless indicated otherwise.

Calcium imaging

Ca fluorescence in patch-clamped myocytes was imaged using an inverted Nikon Diaphot microscope (60X objective, Olympus America Inc., Center Valley, PA) equipped with a CCD-based Photometrics (Tucson, AZ) Cascade 128+ camera (~100 frames/s, 128x128 pixels) operating under Imaging Workbench software (version 6.0, INDEC BioSystems, Santa Clara, CA). Pseudo line scan space-time plot images were generated from the acquired video data using ImageJ software [19]. Whole-cell Ca fluorescence traces were corrected for bleaching and then normalized to the peak amplitude of the Ca transient of the first AP in the AP train. Space-time plots were normalized in like manner per row along the space-axis that exhibited fluorescence signals originating from myocytes. Signals from non-myocyte regions were set to 0 for clarity.

Rapid caffeine solution delivery

To measure SR Ca content, patch-clamped myocytes were rapidly superfused with Tyrode's solution containing 10 mmol/L caffeine, 2.7 mmol/L Ca, and 0.25 µmol/L ISO using a rapid solution exchange device [20] positioned near the myocyte under the control of Axopatch software.

Mathematical model of cardiac tissue and simulations

Tissue simulations in one-dimensional (1D) cables (25 myocytes), two-dimensional (2D) tissue (25x25 myocytes) and three-dimensional (3D) tissue (25x25x25 myocytes) were carried out using the rabbit ventricular AP cell model previously described in Mahajan *et al.*[21]. The partial differential equation governing voltage is:

$$\frac{\partial V}{\partial t} = -I_{ion}/C_m + \nabla \cdot D\nabla V \qquad [1]$$

where V is the membrane voltage and C_m is the membrane capacitance (1 μF/cm^2). The diffusion term in Eq.1 is $D_x \frac{\partial^2 V}{\partial x^2}$ for 1D; $D_x \frac{\partial^2 V}{\partial x^2} + D_y \frac{\partial^2 V}{\partial y^2}$ for 2D; and $D_x \frac{\partial^2 V}{\partial x^2} + D_y \frac{\partial^2 V}{\partial y^2} + D_z \frac{\partial^2 V}{\partial z^2}$ for 3D. Eq.1 was discretized with a spatial resolution Δx=Δy=Δz=0.015 cm and integrated using an operator splitting and time adaptive algorithm with the time step (Δt) varying from 0.01 ms to 0.1 ms. Simulations were mainly done in isotropic tissue (i.e. $D_x=D_y=D_z=D$) with a diffusion constant 0.000557 cm^2/ms, unless otherwise indicated. In some 2D simulations, $D_x=0.25D_y$ was used to create 2:1 anisotropy in conduction velocity. The number of nearest neighbors in 1D, 2D, and 3D tissue were 2, 4, and 6, respectively.

DADs were generated by commanding an intracellular Ca transient using a Gaussian-shaped function in time as follows

$$[Ca]_i = A \cdot e^{-(t-\bar{t}_0)^2/2\sigma^2} \qquad [2]$$

where *A* is the maximum amplitude of the transient, t_0 sets the latency of the DAD, and σ controls the width of the Ca transient. To convert from measured FWHM values to σ, we used the standard equation for a Gaussian distribution: σ = FWHM / 2(2 ln 2)$^{1/2}$. Once an AP upstroke was detected, the Ca clamp waveform was turned off and Ca was allowed to run freely in the model. The amplitude, duration, and latency period of the Ca transient waveform were varied to simulate the experimentally-measured values. Assignment of latency periods to different myocytes in tissue simulations was accomplished by a bootstrap method, randomly selecting latency periods from the distribution of actual experimental data points corresponding to the low and high Ca load cases summarized in Table 3-1.

In the cell model, diastolic Ca-voltage coupling gain [9] was changed by altering the maximal conductance of the Na-Ca exchanger from its normal control value ($\overline{G}_{NCX} = 0.84\frac{\mu S}{\mu F}$) in the UCLA rabbit ventricular model. We refer to this control value as 1.0 and report the fold-change in $\overline{G}_{NCX}$ required for DAD to trigger an AP in tissue. $\overline{G}_{K1}$, the other major determinant of the diastolic Ca-voltage coupling gain, was left at its control value ($\overline{G}_{K1} = 0.30\frac{\mu S}{\mu F}$) to avoid causing changes in resting membrane potential.

Data Analysis and Statistics

Data are presented as medians and 95% CIs. The conventional percentile bootstrap-resampling approach with 10,000 replications was used for estimating 95% CIs [22, 23]. All analyses were performed by subroutines for bootstrapping developed in the Python programming language, using the Numpy and Scipy packages, based on our previously published code [24].

Results

Post-pacing Ca waves and DADs in isolated ventricular myocytes

Isolated patch-clamped rabbit ventricular myocytes were exposed to elevated extracellular [Ca] ($[Ca]_o$, 2.7 mmol/L) and ISO (0.25 µmol/L) and paced for 1 to 5 beats at a cycle length of 400 ms in order to load the myocyte incrementally with intracellular Ca. After each pacing train, the myocyte was left unstimulated for 5 s during which intracellular Ca fluorescence was imaged and membrane voltage recorded to detect Ca waves and DADs respectively, as illustrated in Fig. 3-1. In this representative myocyte, a single pacing stimulus (left-most column) elicited an AP and Ca transient, followed by a barely perceptible DAD (top row) associated with a small Ca transient after a long latency period (2nd row). The Ca transient was caused by a Ca wave arising from a site of origin near the middle of the cell (4th row, red dot) which propagated only partially through the cell (3rd row). As the number of paced beats in the train was increased from 2 to 5 (subsequent columns), DADs due to Ca waves arose from multiple sites following the last paced beat (indicated by the dashed vertical red line) in each train. With longer pacing trains, Ca waves began to appear during the pacing train (not shown), complicating the analysis of post-pacing Ca waves. Therefore, pacing trains longer than 5 beats were excluded from further analysis.

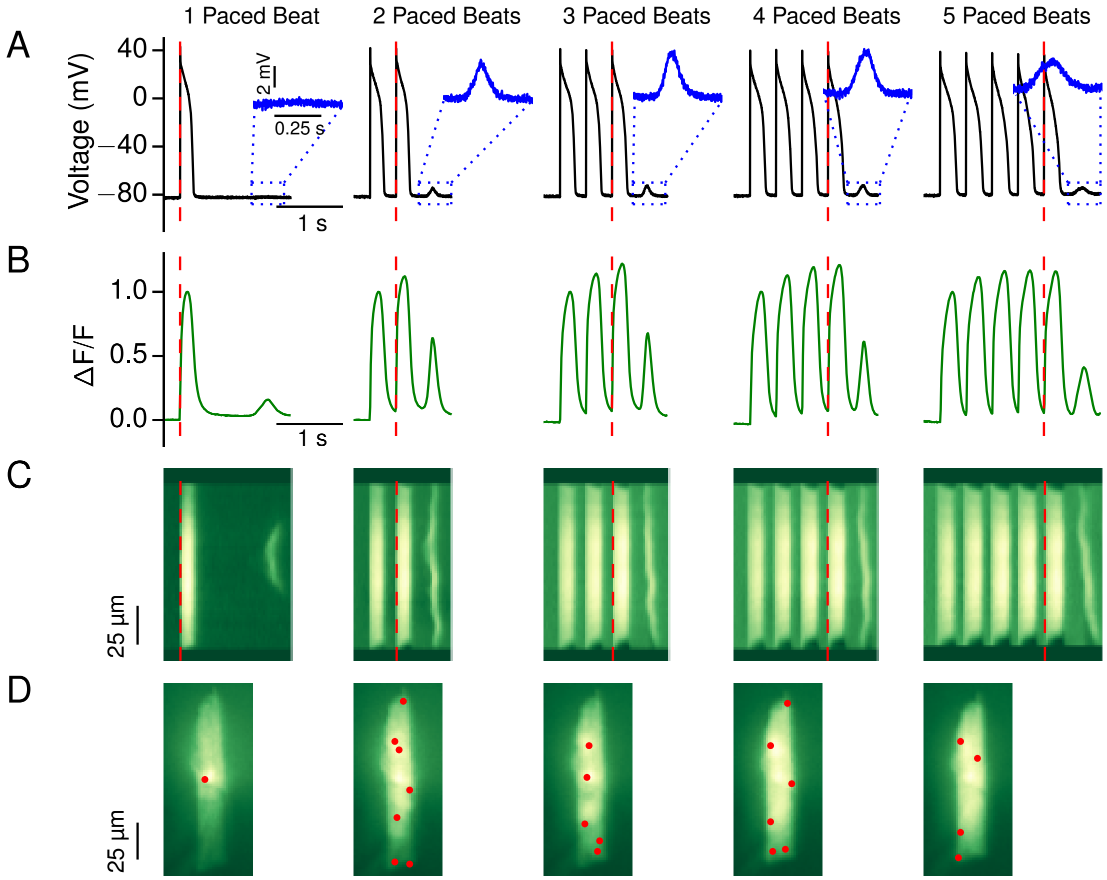

Figure 3-1. Induction of Ca waves and DADs by rapid pacing in a representative isolated ventricular myocyte**.**

Ca waves and corresponding DADs elicited from rabbit ventricular myocytes (n=10) exposed to elevated [Ca]o (2.7 mmol/L) and ISO (0.25 µmol/L) following a pacing train from 1 to 5 beats at 400 ms pacing cycle length. A-B. Voltage and Ca fluorescence traces illustrating post-pacing DADs and Ca wave transients as the number of paced beats was increased from 1 to 5. Dashed red line indicates the beginning of the last paced beat in a pacing train from which the latency period to the onset of the first spontaneous Ca wave or DAD was measured. C. Corresponding space-time plots of Ca fluorescence. D. Ca wave initiation sites (red dots) corresponding to post-pacing Ca waves.

The experimental data on DAD and Ca transient characteristics including amplitude, duration (full width at half maximum, FWHM), and rate of rise for 10 myocytes subjected to the same pacing train protocol in Fig. 3-1 are summarized in Fig. 3-2. Since the number of paced beats required to elicit a DAD varied from myocyte to myocyte and even from trial to trial due to the stochastic nature of spontaneous SR Ca release, the experimental DAD and Ca transient characteristics were compared relative to the minimum number of paced beats required to elicit the first post-pacing DAD (ranging from 1, as in Fig. 3-1, to 3-4). Hence, the horizontal axis label “+0” refers to the minimum number of paced beats required to elicit a DAD, “+1” refers to the DAD elicited by one additional paced beat over the minimum number, “+2” refers to the DAD elicited by two additional paced beats over the minimum, and so forth. The results show that as the number of additional paced beats increased and progressively loaded SR Ca stores (see later), DAD amplitude increased, duration shortened, and rate of rise increased (Fig. 3-2B), roughly in parallel with the changes in integrated whole-cell Ca wave transients (Fig. 3-2A).

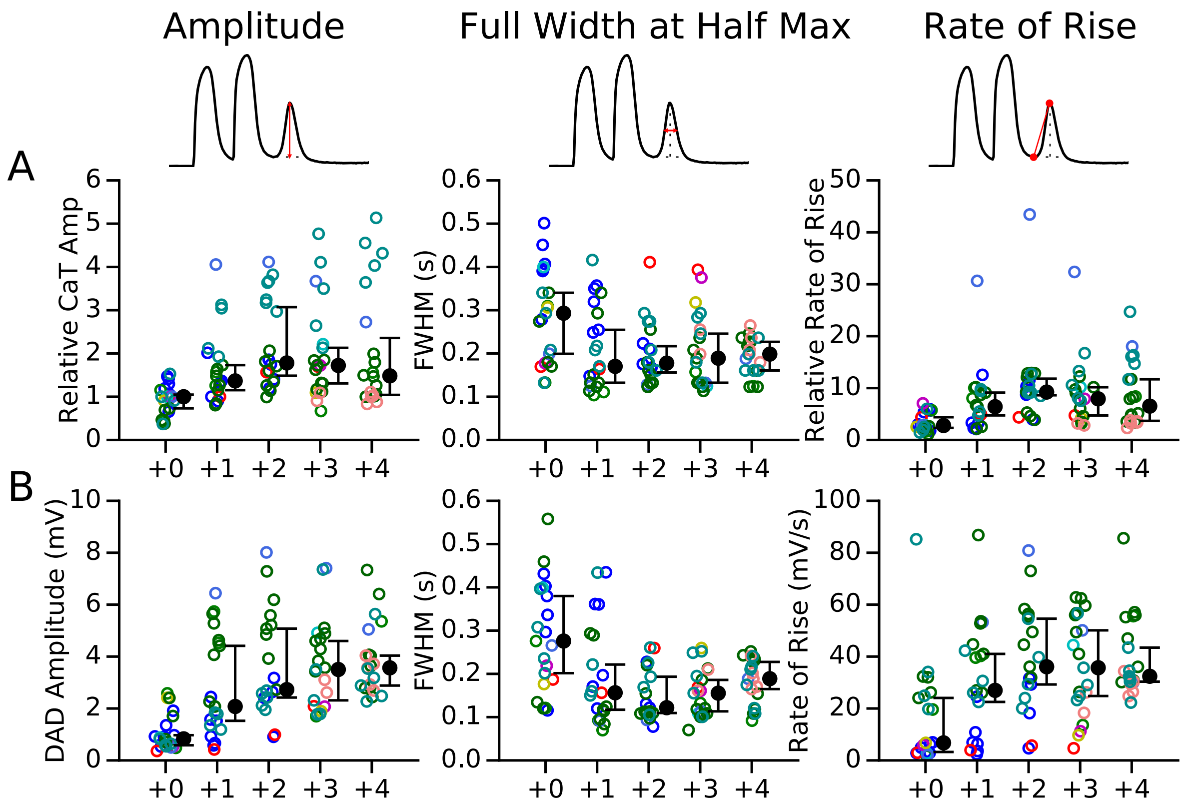

Figure 3-2. Post-pacing Ca wave transients and DAD properties in 10 isolated myocytes.

Ca wave transient (A) and DAD (B) amplitude, duration (FWHM) and rate of rise versus the number of paced beats (see text). Data from individual myocytes are shown in separate colors. Medians and 95% CIs of medians are indicated in black. Traces at top indicate how measurements were made (red lines).

In 4 of the 10 myocytes, the first DAD elicited by the minimum number of paced beats (the "+0" case in Fig. 3-2) resulted from multiple Ca wave initiation sites, instead of a single site as in Fig. 3-1. Therefore, we also analyzed the DAD and Ca transient characteristics according to the number of Ca wave initiation sites underlying the Ca transient and DAD. As shown in Fig. 3-3, as the number of Ca wave initiation sites increased, the resulting Ca transient (Fig. 3-3A) and DAD amplitude (Fig. 3-3B) increased, the duration shortened, and the rate of rise increased.

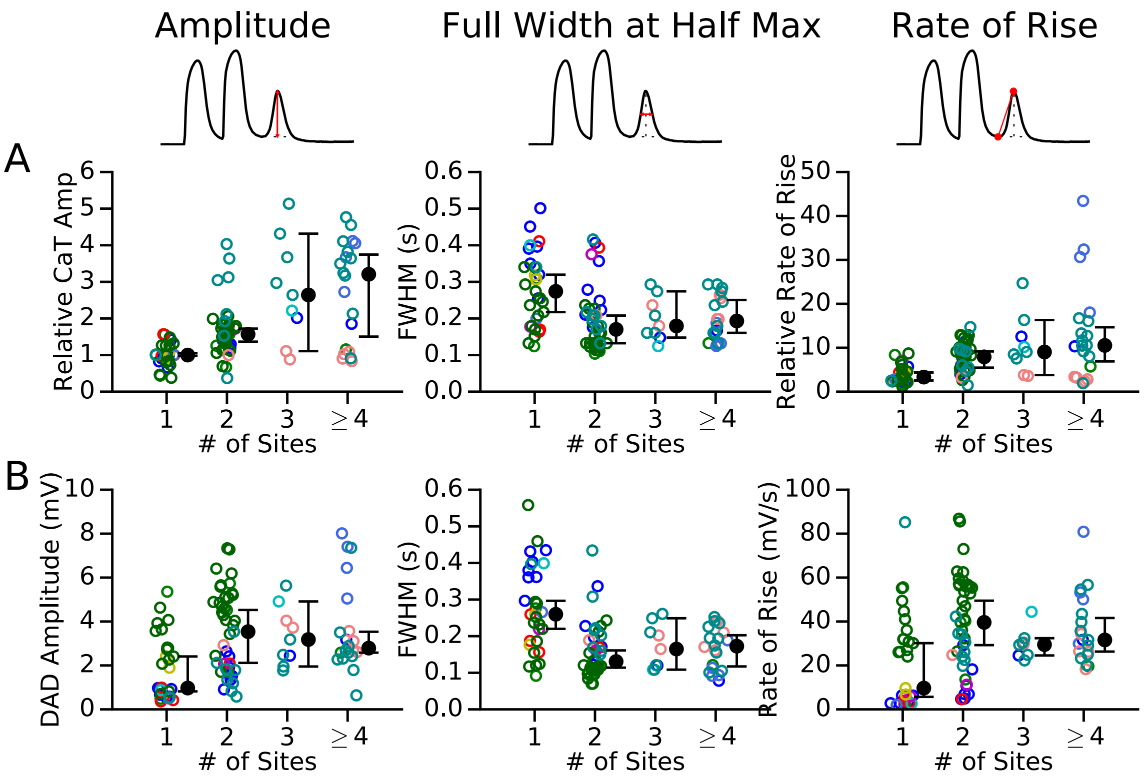

Figure 3-3. Post-pacing Ca wave transients and DAD properties in 10 isolated myocytes.

Ca wave transient (A) and DAD (B) amplitude, duration (FWHM) and rate of rise versus the number of sites initiating the post-pacing Ca wave (see text). Data from individual myocytes are shown in separate colors. Medians and 95% CIs of medians are indicated in black. Traces at top indicate how measurements were made (red lines).

Post-pacing Ca transient and DAD latency period distributions

The latency period, defined as the time interval from the last pacing stimulus to the onset of the first post-pacing Ca wave or DAD, also shortened as the number of paced beats in the train increased, as shown in Fig. 3-4A. The variance of the latency period also decreased significantly. Similarly, when the data was analyzed according to the number of Ca wave initiation sites (analogous to Fig. 3-3), both the latency period and its variance decreased as the number of Ca wave initiation sites increased (Fig. 3-4B).

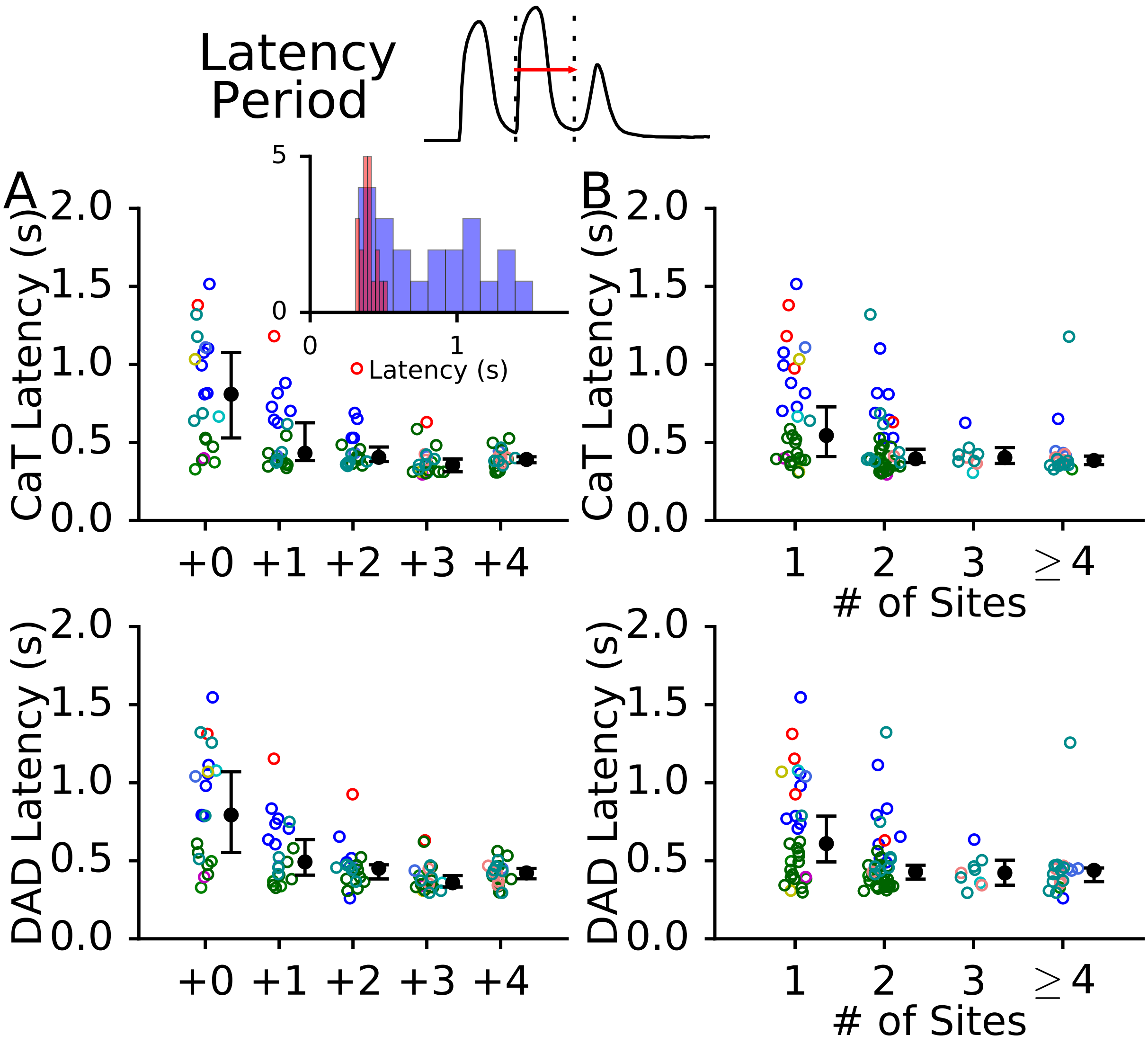

Figure 3-4. Post-pacing Ca wave transients and DAD latency periods in 10 isolated myocytes.

A. Latencies of Ca wave transients (above) and DADs (below) versus the number of paced beats corresponding to Fig. 3-2. Inset in upper panel shows the histogram of latencies after 1 (blue) or 5 (red) paced beats. B. Same as A but as a function of the number of sites initiating the post-pacing Ca wave transient, corresponding to Fig. 3-3. Data from individual myocytes are shown in separate colors. Medians and 95% CIs of medians are indicated in black. Trace at top indicates how measurements were made (red lines).

Post-pacing intracellular Ca load

The changes in Ca transient and DAD amplitude, duration, rate of rise, and latency period distributions observed in Figs. 3-2 to 3-4 are related to progressive intracellular Ca loading as the number of paced beats in the train increased [16, 17]. For example, it is apparent from the traces in Fig. 3-1B that diastolic Ca fluorescence did not return fully to the baseline between paced beats, consistent with the total intracellular Ca increasing with the number of paced beats. To estimate quantitatively the increase in SR Ca load as the number of paced beats increased, 6 voltage-clamped myocytes were paced with an AP clamp waveform. After the last AP waveform in the train (ranging from 1 to 5 beats), a caffeine pulse (10 mmol/L for 1 s) was rapidly applied to release SR Ca, and the resulting inward current due to Na-Ca exchange [4] was recorded simultaneously with the caffeine-induced Ca transient (Fig. 3-5A). The inward current (Fig. 3-5B) was integrated from the onset of caffeine exposure until return to the diastolic baseline to estimate the charge movement related to Ca extrusion by Na-Ca exchange. Fig. 3-5C shows that the intracellular Ca released by caffeine increased progressively with the number of paced beats in the train, from 0.00575 [0.00455, 0.01220] fmol/pF following a single paced beat to 0.01302 [0.01051, 0.01752] fmol/pF after 5 paced beats, a 2.3-fold increase.

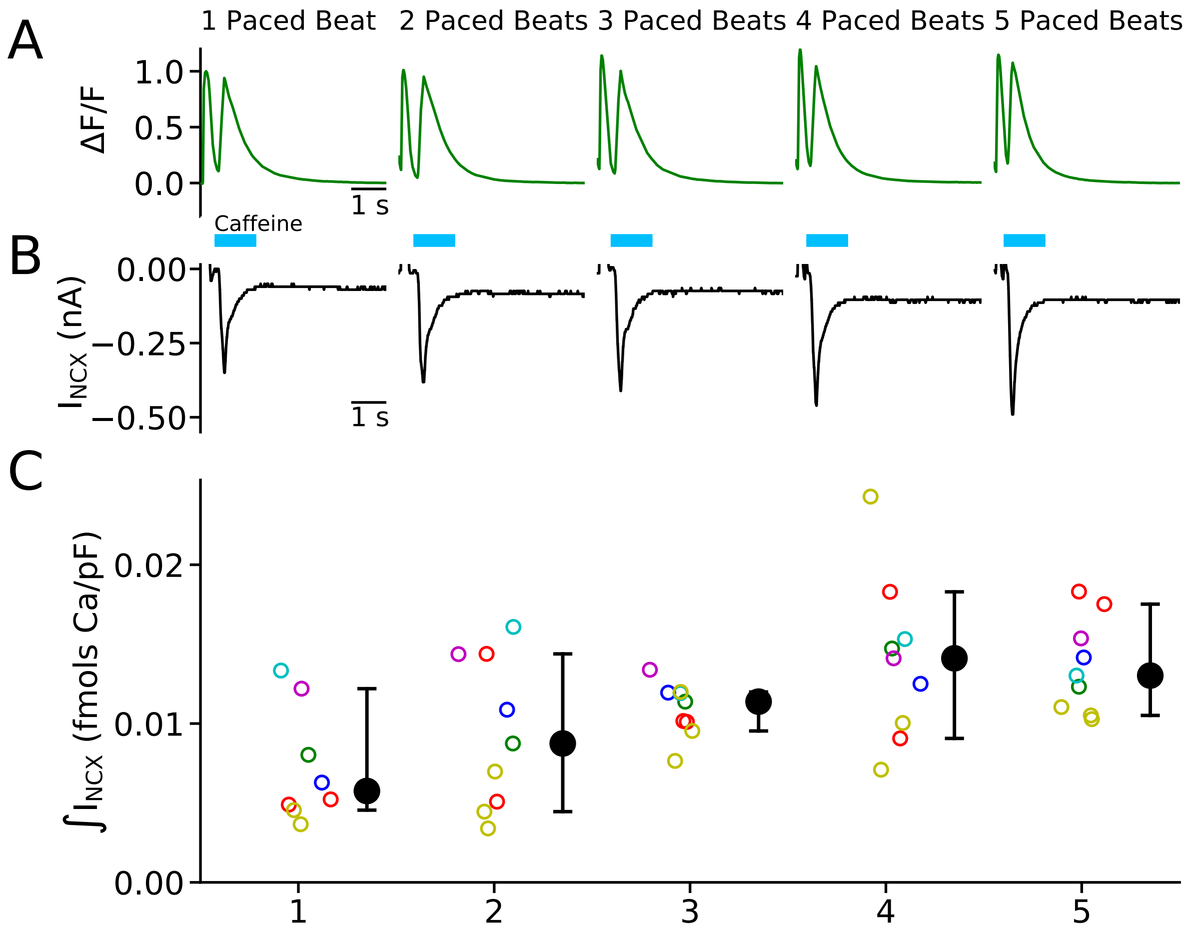

Figure 3-5. SR Ca load versus number of paced beats.

A-B. Rabbit ventricular myocytes (n=6) were paced from 1-5 beats with an AP waveform in the voltage clamp mode. Five hundred ms after the last AP, caffeine (10 mmol/L) was rapidly superfused for 1 s to release SR Ca. A. Ca fluorescence and B. membrane currents were recorded after the last paced AP. C. Ca extruded by Na-Ca exchange during the caffeine pulse, calculated from the integral of INCX during the caffeine-induced Ca transient, as a function of the number of paced beats. Data from individual myocytes are shown in separate colors. Medians and 95% CIs of medians are indicated in black.

Incorporation of experimental Ca wave and DAD characteristics into simulated 2D cardiac tissue

The experimental findings above demonstrate that as the intracellular Ca load increased with longer pacing trains (Fig. 3-5), post-pacing Ca transients and DADs had higher amplitude, shorter duration with a faster rate of rise (Fig. 3-1 to 3-3), and occurred earlier with a narrower latency period distribution (Fig. 3-4). To estimate quantitatively the degree to which each of these factors influences DAD characteristics in tissue, where source-sink effects come into play [11], we simulated a 2D cardiac tissue (25x25 myocytes) using a rabbit ventricular AP and Ca cycling model [21]. To generate DADs, the model (using control parameter values) was equilibrated to pacing at a cycle length of 400 ms, and one of two idealized intracellular Ca transient waveforms was commanded for each cell at a pre-specified latency period to stimulate I_{NCX} and evoke a DAD. For this purpose, the experimental data were categorized into either a low or a high intracellular Ca load case (Tables 3-1 and 3-2). For the low Ca load case, Ca transients were modeled to have a *long* duration with FWHM of 293 ms corresponding to the pooled median duration after 1 paced beat (Fig. 3-3A), a *low* amplitude corresponding to the relative amount of caffeine-induced SR Ca release following 1 paced beat (Fig. 3-5) and *broad* latency distribution bootstrapped from the pooled data after 1 paced beat (Fig. 3-4A, inset). For the high Ca load case, Ca transients were modeled to have a *short* duration of 198 ms corresponding to the pooled median duration after 5 paced beats (Fig. 3-3A), a *high* amplitude potentiated by a 2.3-fold greater SR Ca content than the low Ca load case (based on the relative increase in SR Ca load after 5 paced beats in Fig. 3-5), and a *narrow* latency distribution bootstrapped from the pooled data after 5 paced beats (Fig. 3-4A, inset). With these settings and the normal diastolic Ca-voltage coupling gain in the UCLA rabbit ventricular model (see Methods), the absolute [Ca] of Ca fluorescence waveform for the low Ca load case was set to produce a peak DAD amplitude of 0.83 mV, corresponding to the median value of the experimentally measured DAD amplitude for the low Ca load case. When the corresponding Ca waveform for the high Ca load case was converted to absolute [Ca] by the same scaling factor, the DAD amplitude was 3.62 mV, very close to the experimentally observed DAD amplitudes for the high Ca load case (Fig. 3-3B). This finding validated that the model produced similar results to the experimental measurements in real ventricular myocytes. The median and 95% CIs for SR Ca loads and latency periods for the low and high Ca load conditions are listed in Table 3-1.

Table 3-1. Properties of Ca waves and DADs associated with low and high Ca loads after 1 and 5 paced beats, respectively

Experimental CaT Properties	**Median FWHM (mV) (Median # Ca Wave Initiation Sites)**	**SR Ca load (fmol/pF)**	**Median DAD Amplitude (mV)**	**Latency Period (ms)**
Low Ca	293 (1)	0.0058 [0.0045, 0.0122]	0.83 [0.58, 0.97]	809 [529, 1076]
High Ca	198 (5)	0.0130 [0.0105, 0.0175]	3.56 [2.88, 4.04]	391 [370, 408]
Idealized CaT Properties	**FWHM (ms)**	**Relative Ca Released**	**DAD Amplitude (mV)**	**Latency Period (ms)**
Low Ca	293	1	0.83	809 [529, 1076]
High Ca	198	2.3	3.62	391 [370, 408]

Summary of experimental data in isolated rabbit myocytes (Experimental CaT Properties) from which properties of idealized Ca waves corresponding to low Ca load and high Ca load cases (Idealized CaT Properties) were derived. For the low Ca load case, experimental data corresponds to Ca waves initiated following 1 paced beat (in which Ca waves arose from a median of 1 site), with a low SR Ca load and the broad latency distribution after 1 paced beat shown in Fig. 3-4A (inset, blue histogram). For the high Ca load case, experimental data corresponds to Ca waves which were initiated after 5 paced beats (in which Ca waves arose from a median of 5 sites), with a 2.3-fold higher SR Ca load and the narrow latency distribution after 5 beats shown in Fig. 3-4A (inset, red histogram). DAD amplitudes produced in the model were measured at an NCX Multiplier value of 0.225. Values shown are the median and 95% CI. (CaT: Ca transient).

In order to assess how the features of the Ca transient waveforms and DADs in uncoupled single myocytes scale to the tissue level in which source-sink relationships become important [11], we implemented the idealized Ca transient waveforms corresponding to the high and low Ca load cases into a virtual tissue of 25x25 myocytes. The timing of the Ca transient waveform for each myocyte in the tissue was randomly selected from the narrow latency distribution after 5 paced beats in Table 3-1 for the high Ca load case, and from the broad latency distribution after 1 paced beat in Table 3-1 for the low Ca load case. Due to voltage diffusion when the myocytes were coupled, the resulting DADs in tissue had a lower amplitude and broader duration than their single myocyte counterparts (Fig. 3-6A, right traces). For the high Ca load case, DAD amplitude decreased by 16% from 3.58 to 2.99 mV, and the FWHM increased by 13% from 205 ms to 232 ms (Fig. 3-6A, left traces). For the low Ca load case, DAD amplitude in the tissue decreased by an average of 72% from 0.82 to 0.23 mV, and the FWHM increased by 314% from 233 ms to 965 ms. The greater attenuation of DAD amplitude and rate of rise in the low Ca load case occurred because the broad latency period distribution caused significant desynchronization of the Ca waves among myocytes in the tissue, attenuating the peak and smearing the duration to a greater extent than the high Ca load case with its narrower latency distribution.

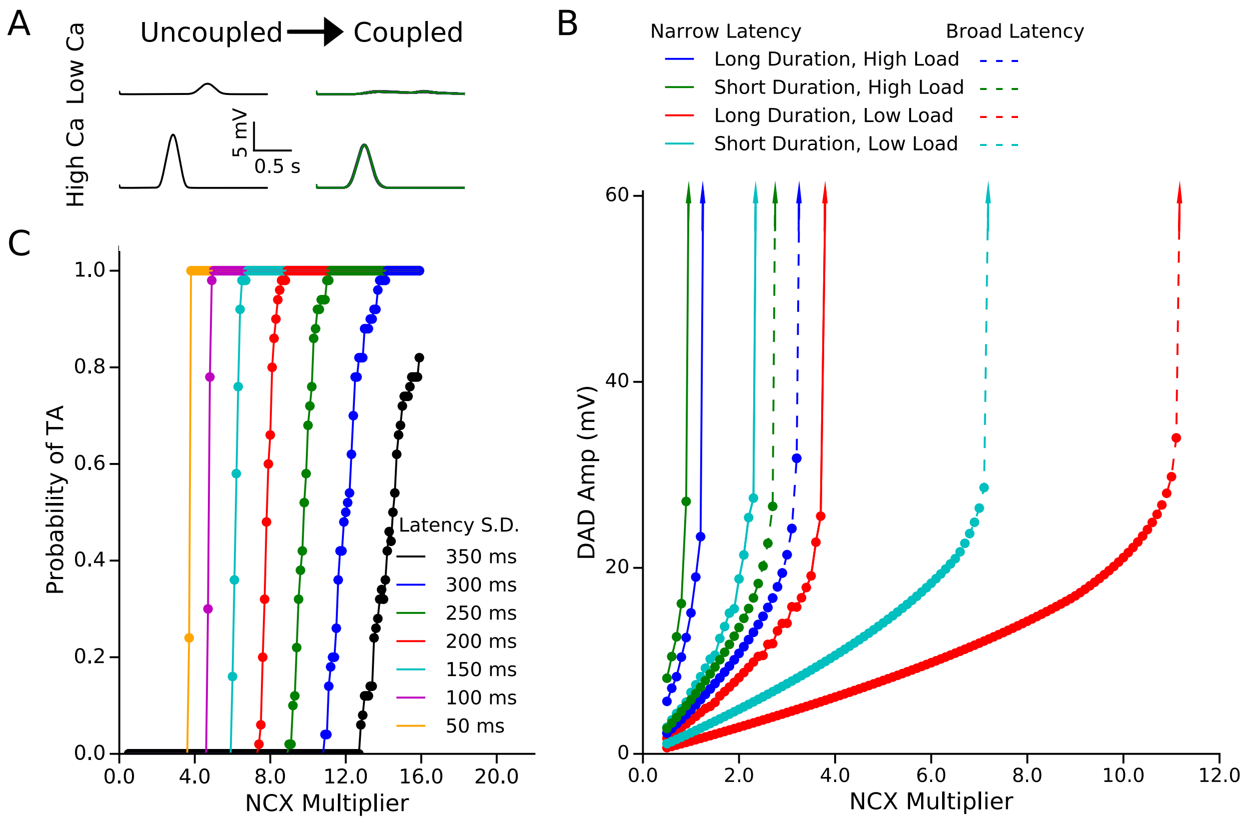

Figure 3-6. DAD simulations in virtual 2D cardiac tissue.

A. Attenuation and prolongation of DADs when myocytes are diffusively coupled in simulated 2D cardiac tissue (25x25 myocytes, D = 0.000557 cm2/ms). Traces show the cellular DADs corresponding to the low (upper) and high (lower) SR Ca loads before (left) and after coupling (right). Timing of the cellular DADs in individual myocytes throughout the tissue was randomly selected from the broad (upper) and narrow distributions (lower) in Table 3-1 and Fig. 3-4A (inset). B. Maximum DAD amplitude in 2D tissue as a function of the fold-change in maximal Na-Ca exchange conductance (NCX Multiplier), which alters the diastolic Ca-voltage coupling gain for different combinations of Ca transient (CaT) (high load or low load), duration (short or long FWHM), and latency distributions (narrow or broad) corresponding to the high and low Ca load cases in Tables 3-1 and 3-2. Sudden jumps in DAD amplitude indicate the thresholds for triggering an AP. C. Effect of the latency distribution on the probability of a DAD reaching the threshold to trigger an AP. Using the Ca wave/DAD properties corresponding to the low Ca load case (Tables 3-1 and 3-2) and a Gaussian distribution of latencies in the simulated 2D tissue (25x25 myocytes), the probability of a DAD triggering an AP in 50 trials for each NCX Multiplier value is plotted, as the standard deviation of the latency period distribution is varied from 350 to 50 ms. (TA: triggered activity).

In order to assess the ability of DADs to elicit APs in tissue, we scaled the amplitude of the high Ca load waveform uniformly to the minimum required to produce a suprathreshold DAD in the 2D tissue at the control value of the diastolic Ca-voltage coupling gain. The tissue simulations were repeated 50 times with a different randomly-selected spatial distribution of latency periods in each trial, using the narrow latency distribution (Table 3-1 and Fig. 3-4A inset). The Ca waveform amplitude which resulted in a triggered AP in at least 1 of the 50 trials was defined as the threshold (Fig. 3-6B, solid green line, and Table 3-2). This Ca waveform peaked at a submembrane [Ca] of 1.45 µM which caused a suprathreshold DAD triggering an AP in a single uncoupled myocyte. When the amplitude of the low Ca load waveform was scaled by the same factor, the Ca waveform peaked at a submembrane [Ca] of 0.426 µM, which resulted in a subthreshold DAD of 14 mV in a single uncoupled myocyte (which was attenuated in 2D tissue to 1.3 mV by source-sink effects). We then asked the question, by what factor did the normal maximal conductance of the Na-Ca exchanger $\overline{G}_{NCX}$ (corresponding to the normal control Ca-voltage coupling gain) need to be multiplied for the low Ca load DAD to reach the threshold to trigger an AP in any of 50 randomized trials in which DAD timing followed the broad latency distribution (Table 3-1)? $\overline{G}_{NCX}$ had to be increased 11.2-fold to trigger an AP (Fig. 3-6B, dashed red trace and Table 3-2). Thus, in the low Ca load case, the combination of low amplitude, slow rate-of-rise, long duration Ca waves (due to fewer Ca wave initiation sites and lower SR Ca content) coupled with a wide latency period distribution markedly suppressed the resulting DAD's ability to reach the threshold to trigger an AP in tissue, unless the Ca-voltage coupling gain was markedly increased by increasing $\overline{G}_{NCX}$ 11.2-fold.

Table 3-2. Ca-voltage coupling gain thresholds required to trigger an AP for different Ca transient waveform properties

Simulated Combination	CaT Duration	CaT Load (High = 2.3 x Low)	Latency Period Distribution	NCX Multiplier for Triggered AP
Low Ca load CaT	Long	Low	Broad	11.2
Hypothetical CaT #1	Short	Low	Broad	7.2
Hypothetical CaT #2	Long	Low	Narrow	3.8
Hypothetical CaT #3	Long	High	Broad	3.3
Hypothetical CaT #4	Short	High	Broad	2.8
Hypothetical CaT #5	Short	Low	Narrow	2.4
Hypothetical CaT #6	Long	High	Narrow	1.3
High Ca Load CaT	Short	High	Narrow	1.0

Based on the properties of the high and low Ca load cases (emboldened) summarized in Table 3-1, six additional hypothetical combinations were generated corresponding to Ca transients with high or low amplitude, short or long duration, and narrow or broad latency distribution. The NCX Multiplier (reflecting the diastolic Ca-voltage coupling gain) required to trigger an AP in a virtual 2D tissue of 25x25 coupled myocytes is listed for each case.

Determinants of the probability of a DAD triggering an AP in tissue

We next addressed which of the above parameter differences between the low and high Ca load cases (DAD amplitude/duration, SR Ca content, or latency variance) had the greatest influence on whether the DAD was able to reach the threshold to trigger an AP. For this purpose, we constructed hypothetical Ca transients possessing hybrid combinations of the three factors from the low and high Ca load cases, generating an additional six hypothetical Ca transients with the properties listed in Table 3-2. For each case, we performed 50 trials, each with a different randomly-selected spatial distribution of latency periods in the 2D tissue for each Ca-voltage coupling gain value. Figure 3-6B shows that among the three factors, the latency period distribution (solid vs. dashed lines) and the SR Ca load (blue vs red, green vs cyan lines) had the largest and nearly equivalent effects on the $\overline{G}_{NCX}$ value (NCX Multiplier) required for the DAD to trigger an AP in tissue. For example, whereas the large Ca load case produced a DAD with the NCX Multiplier value set at 1.0, Hypothetical Case #4 in which the only change was to switch the latency distribution from narrow to broad produced the largest increase in the NCX Multiplier to 2.8. Hypothetical Case #5, in which the only change was to decrease the SR Ca content, caused a slightly lesser increase to 2.4. However, opposite results were obtained for the low Ca load case in which an NCX Multiplier of 11.7 was required to produce a DAD. In this case, the greatest reduction in the NCX Multiplier (to 3.3) occurred in Hypothetical Case #3, in which the SR Ca content was switched from low to high, whereas Hypothetical Case #2, in which the latency distribution was switched from broad to narrow, caused a slightly lesser reduction to 3.8. In contrast, the FWHM of the Ca transient duration reflecting the number of Ca wave initiation sites (Hypothetical Cases #1 and #6) had milder effects that were accentuated when the Ca load was low (cyan vs red lines) rather than high (green vs blue). Based on this data, our results suggest that of the three factors listed in Table 3-2, broadening the latency distribution has the largest effect at suppressing DADs (i.e. by increasing the NCX Multiplier), whereas increasing the SR Ca content has the largest effect at triggering DADs (i.e. by decreasing the NCX Multiplier), with the cellular Ca transient duration having much weaker effects.

The influence of the latency period variance on the threshold value of $\overline{G}_{NCX}$ required for a DAD to trigger an AP in simulated 2D tissue is illustrated further in Fig. 3-6C, which plots the probability (50 trials) of a DAD triggering an AP as Ca-voltage coupling gain was increased by increasing $\overline{G}_{NCX}$. As the latency period variance was decreased from 350 ms to 50 ms, the Ca-$\overline{G}_{NCX}$ value required for a DAD to trigger an AP decreased three-fold.

The results in Fig. 3-6 were robust when the idealized low and high Ca load cases were defined based on the number of Ca release sites in place of the number of paced beats as in Table 3-1. When the FWHM of the Ca transient and the SR Ca content corresponding to the high and low Ca load cases were determined from Ca transients initiated by 1 site vs. 4 or more sites, or for 1-2 sites vs. 3 or more sites, the results were generally similar, except that as a single factor, the SR Ca content had a slightly larger effect on the NCX Multiplier than the latency distribution for both suppressing and triggering DADs. The FWHM of the Ca transient had mild effects in all cases. Results for both cases are shown in the Supporting Material (Tables 3-S1 & 3-S2, Figs. 3-S1 & 3-S2), and compared in Table 3-S3 to the NCX Multiplier values in Table 3-2. Overall, we conclude that the latency distribution and SR Ca load have roughly equivalent influences on the DAD threshold, with the cellular Ca transient duration (FWHM) playing a minor role.

Effects of tissue dimension and the diffusion coefficient

The simulations in Fig. 3-6 represent 2D cardiac tissue with a physiological diffusion coefficient (D=0.000557 cm^2/ms) representing normal gap junction coupling producing a physiological conduction velocity (52 cm/s). Since source-sink relationships are influenced by tissue dimensionality and diffusivity [11], we next investigated how these factors affected the ability of DADs to trigger an AP in tissue. Accordingly, the results in simulated 2D tissue (25x25 myocytes) were compared to a 1D cable (25 myocytes) and a 3D slab (25x25x25 myocytes), using Ca wave transients/DADs corresponding to the high and low Ca load cases in Table 3-1, as well as two of the hypothetical cases in Table 3-2. Fig. 3-7A shows that the NCX Multiplier reflecting the Ca-voltage coupling gain at which DADs triggered an AP was significantly lower in the 1D cable, especially when the latency distribution was broad, whereas the differences between 2D and 3D tissue were small.

Next, we compared the effect of decreasing the diffusion coefficient D (equivalent to reducing gap junction conductance). As shown in Fig. 3-7B, reducing D by a factor of 4 to halve conduction velocity had almost negligible effects on the NCX Multiplier reflecting the Ca-voltage gain required for the DAD (using the low Ca load case) to trigger an AP regardless of tissue dimension. Quantitatively similar results were obtained when D_x only was lowered by a factor of 4 to simulate anisotropic tissue in which the ratio of longitudinal to transverse conduction velocity was 2:1 (data not shown), as occurs in normal ventricle. However, if D was lowered by a factor of 100 to decrease conduction velocity 10-fold, the NCX Multiplier decreased modestly from 6.8 to 3.6 in a 1D cable, 11.2 to 5.4 in 2D tissue, and 12.4 to 8 in 3D tissue.

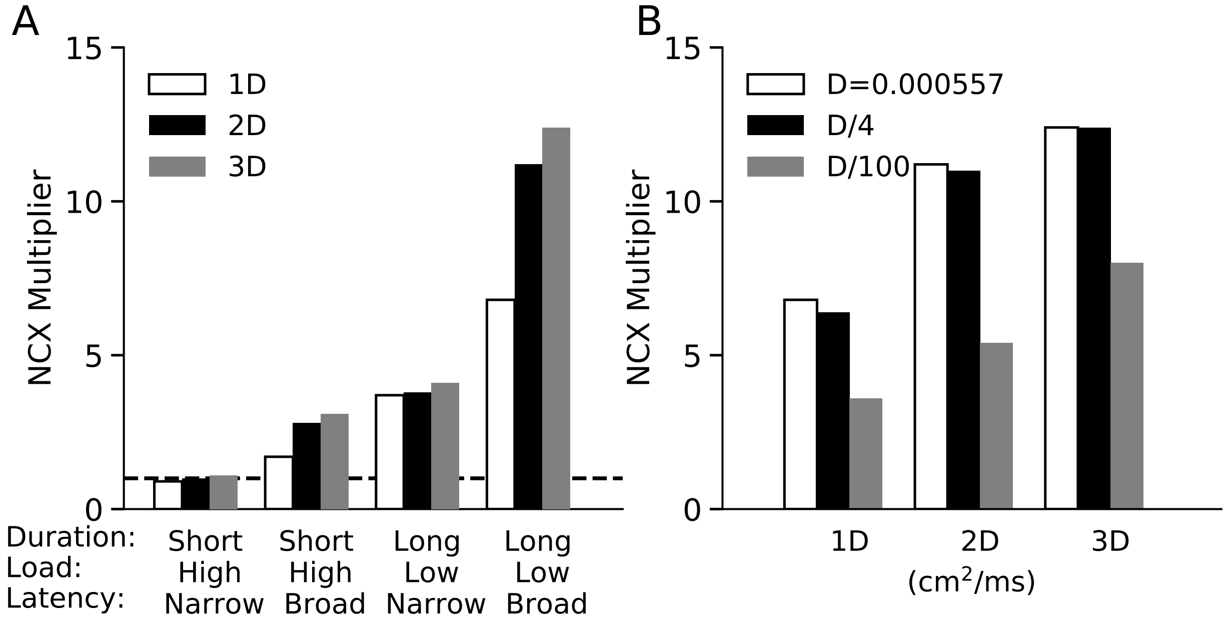

Figure 3-7. Effect of tissue dimension and diffusion coefficient on the ability of a DAD to trigger an AP.

A. The fold-change in maximal Na-Ca exchange conductance (NCX Multiplier), which alters the diastolic Ca-voltage coupling gain, required for a DAD to trigger an AP in 1D (25 myocytes), 2D (25x25 myocytes), and 3D (25x25x25 myocytes) is shown for 4 combinations of DAD properties in Tables 3-1 and 3-2: short or long duration, high or low amplitude, and narrow or broad latency distribution. Dotted black line indicates the control value of NCX Multiplier at which the high Ca load waveform produced a DAD with the minimum required amplitude to produce a suprathreshold DAD in 2D tissue. B. The values of the NCX Multiplier required for a DAD to trigger an AP in a simulated 1D, 2D, and 3D tissue for normal and reduced diffusion coefficients of D=0.000557 cm2/ms, D/4, and D/100, respectively, the latter corresponding to 2-fold and 10-fold reductions in conduction velocity. DAD properties correspond to the low Ca load case in Table 3-1.

Discussion

In this study, we used a combined experimental and modeling approach to analyze the quantitative contributions of subcellular/cellular/tissue scale factors to the probability that a DAD in cardiac tissue can reach sufficient amplitude to trigger an AP. The major known factors that we analyzed include: 1) how quickly the SR Ca is released in each myocyte (i.e. the location and number of sites at which Ca waves are initiated) which defines the peak amplitude and duration of the resulting whole-cell Ca transient activating I_{NCX} and other Ca-sensitive inward currents (the subcellular scale factor); 2) how much SR Ca is released by each myocyte (i.e. the SR Ca load representing the cellular scale factor); 3) how synchronously Ca waves in adjacent myocytes release their SR Ca (i.e. the latency period distribution) required to overcome the source-sink mismatch (the tissue scale factor); and 4) how sensitive the membrane voltage is to the increase in cytoplasmic free Ca (the diastolic Ca-voltage coupling gain, another cellular factor). Although all of these factors contribute to the probability that a DAD will trigger an AP in tissue as intracellular Ca load increases with pacing, the quantitative importance of each factor under experimentally-defined conditions has not, to the best of our knowledge, been rigorously analyzed until the present study. Our major finding is that for a given diastolic Ca-voltage coupling gain, the most influential factors determining whether a DAD in tissue reaches the threshold to trigger an AP are the latency period variance determining the synchrony of cellular Ca waves in a region of tissue and the SR Ca load, with the number of Ca release sites producing a Ca wave playing a minor role. It has previously been shown in confocal imaging studies in intact rat ventricular muscle that isolated Ca waves in individual myocytes during slow pacing caused no detectable changes in membrane potential due to the source-sink mismatch, and only when the majority of myocytes developed Ca waves synchronously did detectable DADs and TA result [15, 16]. Here we show in simulated tissue that even when 100% of the myocytes in the tissue develop Ca transients after a paced beat, the synchronicity of Ca waves still remains a predominant factor determining whether the DAD reaches sufficient amplitude to trigger an AP. This conclusion agrees with the recent simulation study examining the DAD threshold for triggering an AP as SR load was progressively increased in an anatomic rabbit ventricles model [13]. However, in this model, SR Ca load, DAD peak amplitude, rate-of-rise, duration, and latency all changed simultaneously, so that the individual contributions of the subcellular, cellular, and tissue factors were not analyzed. The novelty of our study is that we utilized experimentally measured properties of Ca waves elicited by pacing in rabbit ventricular myocytes to assure that the DAD peak amplitude, rate-of-rise, duration, and latency distributions as SR Ca load increased were physiologically realistic rather than purely model-generated. Thus, for physiologically realistic Ca wave properties, our results indicate that the tissue scale source-sink factor and the cellular scale SR Ca load factor are the most critical determinants of DAD amplitude in cardiac tissue, with the subcellular factor of Ca wave initiation sites determining the duration and peak amplitude of Ca waves in individual myocytes playing a less influential role. This was true for 1D, 2D, and 3D cardiac tissue, whether the diffusion coefficient was normal or reduced (Fig. 3-7). It was also true whether the high and low Ca load cases were determined from data comparing the number of paced beats (Fig. 3-6) or the number of Ca wave initiation sites (Supporting Material). The Ca-voltage coupling gain required for a DAD to trigger an AP was lower for 1D, but similar in 2D and 3D. Diffusion coefficient (gap junction conductance) only had significant effects when markedly reduced.

Biophysical mechanisms underlying Ca waves and DAD features

The mechanisms by which an increased number of Ca wave initiation sites and increased SR Ca load influence DAD amplitude and duration are intuitively straightforward. If whole-cell SR Ca content is released over a shorter time period due to the fusion of multiple Ca waves, the peak amplitude will increase and the duration will narrow proportionately, generating a larger and narrower DAD. If more Ca is released over the same time period due to a higher SR content, the DAD peak amplitude will increase proportionately without affecting DAD duration. However, a high SR Ca load also usually accelerates Ca wave speed, in which case the release time will be modestly shortened to cause a narrower DAD. The mechanism underlying the Ca wave latency period distribution, on the other hand, is more controversial. Experimental evidence indicates that both refilling of SR Ca stores and recovery of RyR refractoriness are complete well before the typical onset of a Ca wave, requiring an additional time delay, which has been called the “idle period” [17]. Theoretical analysis supported by experimental data predicts that the idle period arises from criticality in the CRU network [25] and reflects the time required for a random cluster of adjacent CRUs to all fire within the same time window, thereby releasing enough Ca locally to exceed the minimal wavefront curvature (Eikonal relationship) required for regenerative propagation as a Ca wave. The time needed to form a critical cluster as well as the critical cluster size becomes smaller as SR Ca load and diastolic cytoplasmic Ca increases, so that the mean time before an appropriately sized cluster forms to initiate a Ca wave (the idle period) becomes shorter with less variance. Thus, as the intracellular Ca load increases, latency period distribution becomes narrower with a shorter median time.

Limitations

Our model did not intrinsically generate Ca waves and DADs. Instead, we used commanded Ca waveforms that were specifically tailored to mimic experimentally obtained traces. Thus, during the commanded Ca transient, I_{NCX} did not feed back to affect the evolution of the Ca transient itself. However, since our goal was to reproduce the Ca transients and DADs measured directly from experiments, this was a practical way to achieve the desired realistic Ca transient waveform reflecting the net effects of a highly compartmentalized Ca cycling system in a real myocyte. The fact that the commanded Ca waveforms for the high and low Ca load cases produced corresponding DAD features in the model that fell within experimentally measured DAD amplitude and durations suggests that the approximation is reasonable. Similarly, when we altered the diastolic Ca-voltage coupling gain in the tissue simulations by changing $\overline{G}_{NCX}$ (Fig. 3-6 to 3-7), we made the alteration only from the onset of the commanded Ca transient so as not to affect the SR load independently of the experimentally-defined values.

Unfortunately, we could not directly analyze Ca loading conditions producing suprathreshold DADs, since the triggered AP interrupted the evolution of the Ca waves, precluding accurate measurement of the Ca transient and DAD peak, width, and latency. In order to study suprathreshold DADs capable of triggering an AP, we made the assumption that that the amplitude of the experimentally measured subthreshold DADs could be scaled proportionately for the low and high Ca load cases by increasing the Ca transient waveform amplitude. This is an approximation since as the total Ca load increases and the SR saturates, the differences between the “low” and “high” Ca load cases are likely to become smaller. If the corresponding differences between low and high Ca load DADs become smaller, however, this will minimize the influence of the cellular DAD characteristics (amplitude/duration) relative to the tissue DAD characteristics (determined by the latency distribution) on the ability of a DAD to trigger an AP in tissue, making our major conclusion even stronger.

We studied the characteristics of Ca waves and DADs induced by a single condition, namely the combination of ISO and modestly elevated $[Ca]_o$, and it is possible that other interventions may give different results. Cytoplasmic dialysis of the Ca-buffering fluorescent dye Fluo-4 as well as washout of other constituents could also have influenced the Ca wave features. We deliberately studied DADs with amplitudes that were below the threshold for eliciting an AP so that we could characterize the full time evolution of Ca waves and DADs uninterrupted by APs. However, further increasing ISO to 0.5 μmol/L and $[Ca]_o$ to 3.6 mmol/L consistently induced post-pacing triggered activity (unpublished observations).

Commanding DADs at the whole-cell level also does not account for the synchronizing effects of membrane depolarization on Ca wave onset in adjacent cells [26], effectively making the latency distribution somewhat narrower compared to that of isolated myocytes. We also did not account for intracellular Ca diffusion from myocyte-to-myocyte through gap junctions, which might have a cooperative effect on the timing of Ca wave initiation in nearby myocytes. Although Ca wave propagation from myocyte to myocyte has been observed in myocyte pairs [27], it is generally a slow process. Whether it would have much influence on latency periods in the range of 400 ms (Fig. 3-4) is unclear but can be investigated in future simulation studies. Finally, we simulated homogeneous tissue, in which all the myocytes had identical cellular properties except for the assigned latency period of the Ca transient, whereas real cardiac myocytes and tissue are heterogeneous. Future studies will be required to determine whether these cellular and tissue heterogeneities have important effects.

Conclusions

Our findings indicate that among subcellular, cellular, and tissue scale factors known to influence DAD amplitude in cardiac tissue, the latency period distribution of Ca waves (the tissue scale factor) and SR the Ca load (the cellular scale factor) are quantitatively the most influential in determining whether a DAD reaches the threshold to elicit a triggered AP. Thus, the narrowing of the latency period distribution as the intracellular Ca load increases during pacing plays a major role in shaping the rate dependence of DAD amplitude, coupling interval, and initiation of TA noted in previous experimental studies [16, 28]. By desynchronizing the timing of Ca waves in myocytes, the effect of a broad latency distribution is to attenuate the tissue DAD amplitude and prolong its duration in comparison to the DAD generated by the same Ca wave in an uncoupled myocyte. This effect protects normally-coupled 3D tissue from DAD-induced TA.

A novel finding is that reducing the diffusion coefficient four-fold (either isotropically or anisotropically), corresponding to two-fold decrease in conduction velocity, did not significantly affect the Ca-voltage coupling gain required for a DAD to trigger an AP (Fig. 3-7B). Even when the diffusion coefficient was decreased 100-fold (isotropically), corresponding to a 10-fold reduction in conduction velocity, the effect was relatively modest (<50%). Thus, gap junction remodeling that uniformly or anisotropically reduces conduction velocity does not by itself markedly enhance the probability of DAD-induced TA in tissue in which 100% of myocytes exhibit DADs. This is different from the case in which myocytes exhibiting DADs are coupled to myocytes without DADs, as in our previous simulation study [11]. In this case, reducing gap junction coupling dramatically promoted TA by decreasing the current sink effect of the myocytes without DADs. In our simulations, on the other hand, 100% of myocytes in the tissue were commanded to have Ca transients with resulting DADs, so that source-sink mismatches resulted solely from local DAD timing differences as determined by the latency distribution. This is the reason for the probabilistic occurrence of triggered APs near the critical Ca-voltage coupling gain in Fig. 3-6, i.e., not all spatially random distributions of DADs caused a triggered AP because of local source-sink effects.

Another interesting finding relates to the effects of tissue dimensionality. Although the Ca-voltage coupling gain required for a DAD to trigger an AP was only slightly lower in 2D (with 4 nearest neighbors) than 3D tissue (with 6 nearest neighbors), it was significantly reduced in 1D tissue (with 2 nearest neighbors) (Fig. 3-7B). This may be a factor explaining the increased susceptibility of fibrotic tissue to DAD-mediated TA, since fibrosis creates myocyte strands acting functionally as quasi-1D cables embedded in 2D or 3D tissue [29]. Similarly, other factors being equal, the Ca-voltage coupling gain required for a DAD to trigger an AP would be lower in Purkinje fibers (also quasi-1D cables) than in 3D myocardium. Once again, it should be noted that in our simulations, we commanded Ca waves/DADs to occur in 100% of myocytes. When only a region of the tissue exhibits Ca waves/DADs, the effects of tissue dimension on the threshold for TA are quantitatively much larger [11, 13]. We cannot exclude that the small differences in Ca-voltage coupling between 2D and 3D tissue (Fig. 3-7A) might have been larger had we used 11 nearest neighbors for 3D tissue, the average number estimated experimentally in real ventricular tissue [14], instead of the computationally more convenient 6 nearest neighbors. Given that previous simulations investigating the number of nearest neighbors in relation to conduction velocity showed little effect unless the diffusion coefficient was markedly reduced [30], we suspect that this may also be the case for the Ca-voltage threshold required for a DAD to trigger an AP (Fig. 3-7A).

Finally, since real cardiac tissue is heterogeneous both at the cellular and tissue levels, an important consequence of the randomness of latency period distributions is that regions with suprathreshold DADs and subthreshold DADs may coexist in the same tissue. As shown in a recent study [31], subthreshold DADs can locally reduce excitability by inactivating the Na current, leading to conduction block and initiation of reentry. Thus, the same DAD-mediated process can produce both the trigger and vulnerable substrate (due to dispersion of excitability) promoting initiation of reentry and cardiac fibrillation.

AUTHOR CONTRIBUTIONS

J.N.W. and C.Y.K. conceived the study, designed the experiments and wrote the manuscript. C.Y.K. performed the experiments and analyzed the data. M.B.L., Z.S., and Z.Q. designed, performed and analyzed the computer simulations. All authors edited and commented on the manuscript.

References

1. Sato, D., et al., *Synchronization of chaotic early afterdepolarizations in the genesis of cardiac arrhythmias.* Proc Natl Acad Sci U S A, 2009. **106**(9): p. 2983-8.
2. Weiss, J.N., et al., *Perspective: A dynamics-based classification of ventricular arrhythmias.* J Mol Cell Cardiol, 2015. **82**: p. 136-152.
3. Song, Z., et al., *Calcium-voltage coupling in the genesis of early and delayed afterdepolarizations in cardiac myocytes.* Biophys J, 2015. **108**(8): p. 1908-21.
4. Bers, D.M., *Excitation-Contraction Coupling and Cardiac Contractile Force*. 2nd ed. 2001, Dordrecht: Kluwer Academuc Publishers. 149-151.
5. O'Neill, S.C., P. Donoso, and D.A. Eisner, *The role of [Ca++]i and [Ca++] sensitization in the caffeine contracture of rat myocytes: measurement of [Ca++]i and [caffeine]i.* Journal of Physiology, 1990. **425**: p. 55-70.
6. Trafford, A.W., M.E. Diaz, and D.A. Eisner, *A novel, rapid and reversible method to measure Ca buffering and time-course of total sarcoplasmic reticulum Ca content in cardiac ventricular myocytes.* Pflugers Arch, 1999. **437**(3): p. 501-3.
7. Song, Z., Z. Qu, and A. Karma, *Stochastic initiation and termination of calcium-mediated triggered activity in cardiac myocytes.* Proc Natl Acad Sci U S A, 2017. **114**(3): p. E270-E279.
8. Liu, M.B., et al., *A Dynamical Threshold for Cardiac Delayed Afterdepolarization-Mediated Triggered Activity.* Biophys J, 2016. **111**(11): p. 2523-2533.
9. Maruyama, M., et al., *Diastolic intracellular calcium-membrane voltage coupling gain and postshock arrhythmias: role of purkinje fibers and triggered activity.* Circ Res, 2010. **106**(2): p. 399-408.
10. Joyner, R.W., et al., *A spontaneously active focus drives a model atrial sheet more easily than a model ventricular sheet.* Am J Physiol Heart Circ Physiol, 2000. **279**(2): p. H752-63.
11. Xie, Y., et al., *So little source, so much sink: requirements for afterdepolarizations to propagate in tissue.* Biophys J, 2010. **99**(5): p. 1408-15.
12. Myles, R.C., et al., *Local beta-Adrenergic Stimulation Overcomes Source-Sink Mismatch to Generate Focal Arrhythmia.* Circ Res, 2012. **110**(11): p. 1454-64.
13. Campos, F.O., et al., *Stochastic spontaneous calcium release events trigger premature ventricular complexes by overcoming electrotonic load.* Cardiovasc Res, 2015. **107**(1): p. 175-83.
14. Hoyt, R.H., M.L. Cohen, and J.E. Saffitz, *Distribution and three-dimensional structure of intercellular junctions in canine myocardium.* Circ Res, 1989. **64**(3): p. 563-74.

15. Fujiwara, K., et al., *Burst emergence of intracellular Ca2+ waves evokes arrhythmogenic oscillatory depolarization via the Na+-Ca2+ exchanger: simultaneous confocal recording of membrane potential and intracellular Ca2+ in the heart.* Circ Res, 2008. **103**(5): p. 509-18.

16. Wasserstrom, J.A., et al., *Variability in timing of spontaneous calcium release in the intact rat heart is determined by the time course of sarcoplasmic reticulum calcium load.* Circ Res, 2010. **107**(9): p. 1117-26.

17. Belevych, A.E., et al., *Shortened Ca2+ signaling refractoriness underlies cellular arrhythmogenesis in a postinfarction model of sudden cardiac death.* Circ Res, 2012. **110**(4): p. 569-77.

18. Xie, L.H., et al., *Oxidative stress-induced afterdepolarizations and calmodulin kinase II signaling.* Circ Res, 2009. **104**(1): p. 79-86.

19. Collins, T.J., *ImageJ for microscopy.* Biotechniques, 2007. **43**(1 Suppl): p. 25-30.

20. Scaringi, J.A., et al., *A new method to detect rapid oxygen changes around cells: how quickly do calcium channels sense oxygen in cardiomyocytes?* J Appl Physiol (1985), 2013. **115**(12): p. 1855-61.

21. Mahajan, A., et al., *A rabbit ventricular action potential model replicating cardiac dynamics at rapid heart rates.* Biophys J, 2008. **94**(2): p. 392-410.

22. Nakagawa, S. and I.C. Cuthill, *Effect size, confidence interval and statistical significance: a practical guide for biologists.* Biol Rev Camb Philos Soc, 2007. **82**(4): p. 591-605.

23. Efron, B. and R. Tibshirani, *Statistical data analysis in the computer age.* Science, 1995. **253**(5018): p. 390-395.

24. Calmettes, G., G.B. Drummond, and S.L. Vowler, *Making do with what we have: use your bootstraps.* J Physiol, 2012. **590**(Pt 15): p. 3403-6.

25. Nivala, M., et al., *Criticality in intracellular calcium signaling in cardiac myocytes.* Biophys J, 2012. **102**(11): p. 2433-42.

26. Sato, D., et al., *Depolarization of cardiac membrane potential synchronizes calcium sparks and waves in tissue.* Biophys J, 2014. **107**(6): p. 1313-7.

27. Miura, M., P.A. Boyden, and H.E. ter Keurs, *Ca2+ waves during triggered propagated contractions in intact trabeculae.* Am J Physiol, 1998. **274**(1 Pt 2): p. H266-76.

28. Moak, J.P. and M.R. Rosen, *Induction and termination of triggered activity by pacing in isolated canine Purkinje fibers.* Circulation, 1984. **69**(1): p. 149-62.

29. Nguyen, T.P., Z. Qu, and J.N. Weiss, *Cardiac fibrosis and arrhythmogenesis: the road to repair is paved with perils.* J Mol Cell Cardiol, 2014. **70**: p. 83-91.

30. Hubbard, M.L., W. Ying, and C.S. Henriquez, *Effect of gap junction distribution on impulse propagation in a monolayer of myocytes: a model study.* Europace, 2007. **9 Suppl 6**: p. vi20-8.

31. Liu, M.B., et al., *Delayed afterdepolarizations generate both triggers and a vulnerable substrate promoting reentry in cardiac tissue.* Heart Rhythm, 2015. **12**(10): p. 2115-24.

Supplemental Information

Table S1. Properties of Ca waves and DADs associated with low and high Ca loads Corresponding to 1 versus 4+ Ca wave initiation sites

Experimental CaT Properties	# Ca Waves Initiation Sites	SR Ca load (fmol/pF)	Median DAD Amplitude (mV)	Latency Period (ms)
Low Ca	1	0.0058 [0.0045, 0.0122]	0.97 [0.82, 2.41]	545 [409, 728]
High Ca	4-6	0.0130 [0.0105, 0.0175]	2.79 [2.58, 3.53]	384 [358, 412]
Idealized CaT Properties	**FWHM (ms)**	**Relative Ca Released**	**DAD Amplitude (mV)**	**Latency Period (ms)**
Low Ca	274	1.0	0.82	545 [409, 728]
High Ca	193	2.3	3.25	384 [358, 412]

Summary of experimental data in isolated rabbit myocytes (Experimental CaT Properties) from which properties of idealized Ca waves corresponding to low Ca load and high Ca load cases (Idealized CaT Properties) were derived. For the low Ca load case, experimental data corresponds to Ca waves initiated from 1 site, with a low SR Ca load and broad latency distribution. For the high Ca load case, experimental data corresponds to Ca waves which were initiated from 4-6 sites, with a 2.3-fold higher SR Ca load and narrow latency distribution. The NCX Multiplier value for DAD amplitudes produced in the model was 0.205. Values shown are the median and 95% CI. (CaT: Ca transient).

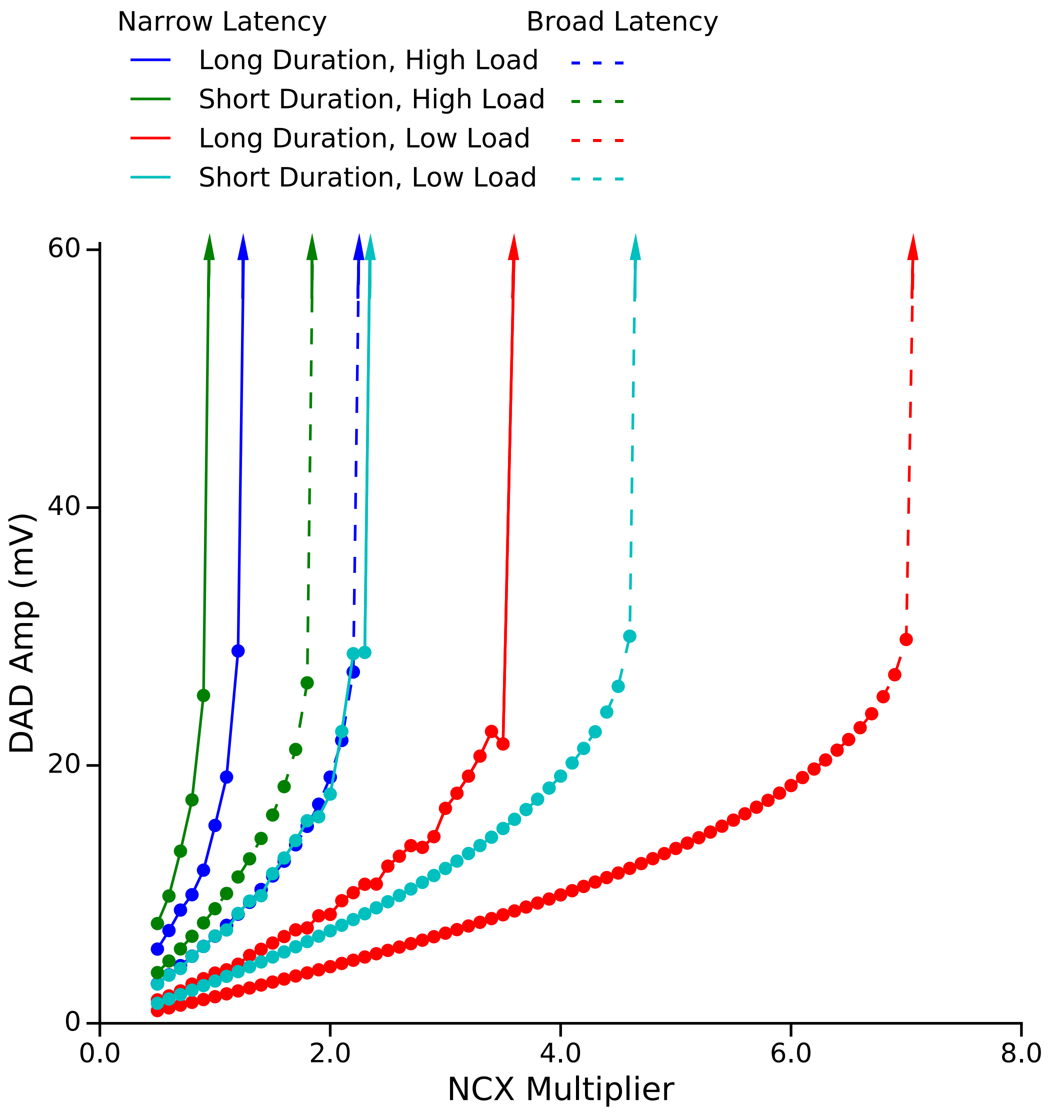

Figure 3-S1. DAD simulations in virtual 2D cardiac tissue. Maximum DAD amplitude in 2D tissue as a function of the fold-change in maximal Na-Ca exchange conductance (NCX Multiplier), which alters the diastolic Ca-voltage coupling gain for different combinations of Ca transient (CaT) amplitude (high or low), duration (short or long), and latency distributions (narrow or broad) corresponding to the high and low Ca load cases in Table 3-S1. Sudden jumps in DAD amplitude indicate the thresholds for triggering an AP. Each data point represents the maximum DAD amplitude measured in 10 simulations.

Table 3-S2. Properties of Ca waves and DADs associated with low and high Ca loads corresponding to 1-2 versus 3+ Ca wave initiation sites

Experimental CaT Properties	# Ca Waves Initiation Sites	SR Ca load (fmol/pF)	Median DAD Amplitude (mV)	Latency Period (ms)
Low Ca	1-2	0.0070 [0.0049, 0.0122]	2.41 [1.84, 3.23]	434 [394, 524]
High Ca	3-6	0.0120 [0.0105, 0.0141]	2.88 [2.58, 3.57]	387 [368, 414]
Idealized CaT Properties	**FWHM (ms)**	**Relative Ca Released**	**DAD Amplitude (mV)**	**Latency Period (ms)**
Low Ca	208	1.0	1.8	434 [394, 524]
High Ca	188	1.7	3.45	387 [368, 414]

Summary of experimental data in isolated rabbit myocytes (Experimental CaT Properties) from which properties of idealized Ca waves corresponding to low Ca load and high Ca load cases (Idealized CaT Properties) were derived. For the low Ca load case, experimental data corresponds to Ca waves initiated from 1 or 2 sites, with a low SR Ca load and broad latency distribution. For the high Ca load case, experimental data corresponds to Ca waves which were initiated from 3-6 sites, with a 1.7-fold higher SR Ca load and narrow latency distribution. The NCX Multiplier value for DAD amplitudes produced in the model was 0.210. Values shown are the median and 95% CI. (CaT: Ca transient).

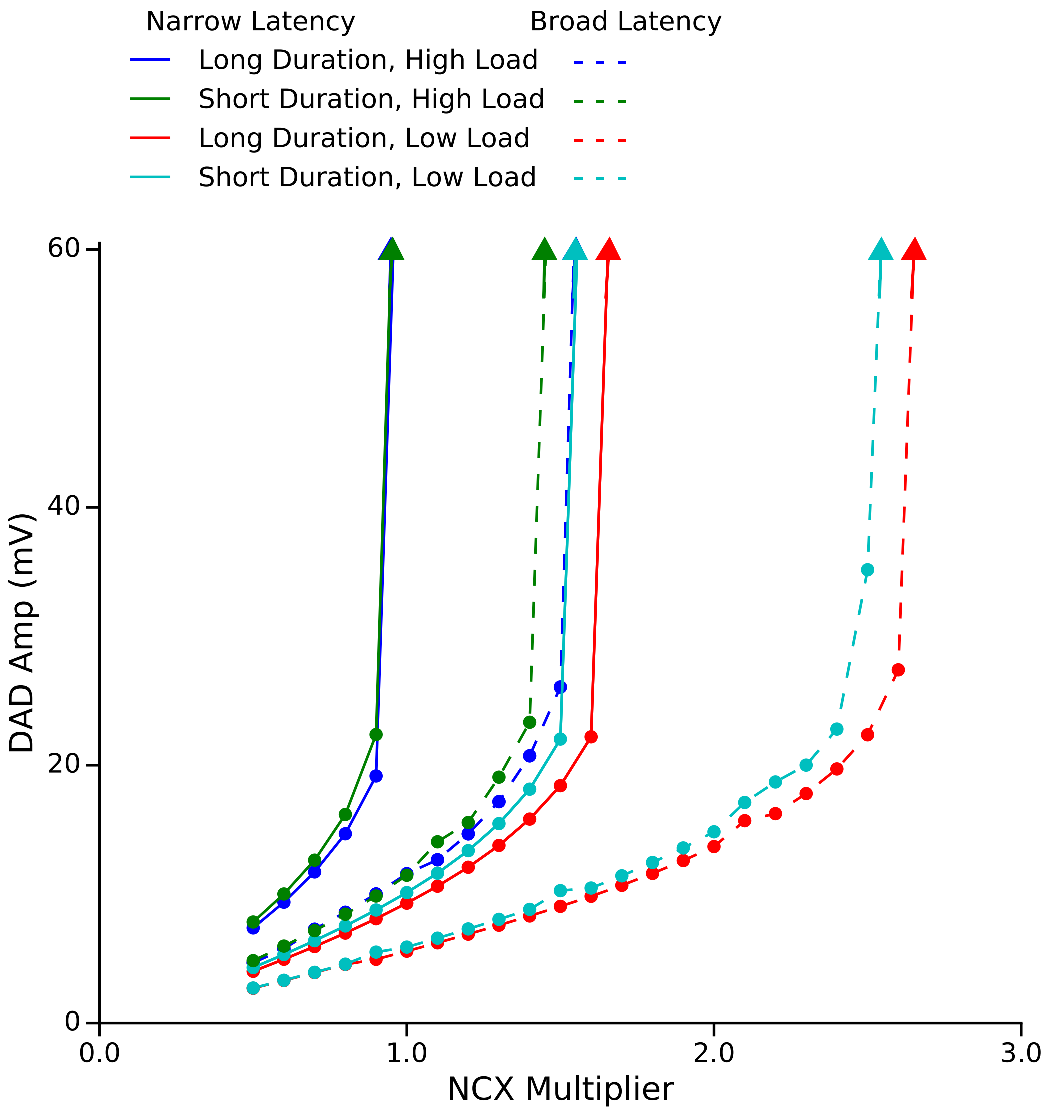

Figure 3-S2. DAD simulations in virtual 2D cardiac tissue. Maximum DAD amplitude in 2D tissue as a function of the fold-change in maximal Na-Ca exchange conductance (NCX Multiplier), which alters the diastolic Ca-voltage coupling gain for different combinations of Ca transient (CaT) amplitude (high or low), duration (short or long), and latency distributions (narrow or broad) corresponding to the high and low Ca load cases in Table 3-S2. Sudden jumps in DAD amplitude indicate the thresholds for triggering an AP. Each data point represents the maximum DAD amplitude measured in 10 simulations.

Table 3-S3. Ca-voltage coupling gain thresholds (NCX Multiplier) required to trigger an AP for different Ca transient waveform properties.

				NCX Multiplier for Triggered AP		
Simulated Combination	**CaT Duration**	**Ca load**	**Latency Distribution**	**1 vs 5 paced beats**	**1 vs 4+ initiation sites**	**1-2 vs 3+ initiation sites**
Low Ca load CaT	Long	Low	Broad	11.2	7.1	2.7
Hypothetical CaT #1	Short	Low	Broad	7.2	4.7	2.6
Hypothetical CaT #2	Long	Low	Narrow	3.8	3.6	1.7
Hypothetical CaT #3	Long	High	Broad	3.3	2.3	1.6
Hypothetical CaT #4	Short	High	Broad	2.8	1.9	1.5
Hypothetical CaT #5	Short	Low	Narrow	2.4	2.4	1.6
Hypothetical CaT #6	Long	High	Narrow	1.3	1.3	1.0
High Ca Load CaT	Short	High	Narrow	1.0	1.0	1.0

Three different analysis methods (1 vs 5 paced beats, 1 vs 4+ Ca wave initiation sites, and 1-2 vs 3+ initiation sites) based on the data summarized in Tables 3-1, 3-S1 and 3-S2 were used to construct idealized high and low Ca load cases (emboldened) and six additional hypothetical combinations corresponding to Ca transients (CaT) with high or low SR Ca load, short or long duration, and narrow or broad latency distribution. The NCX Multiplier (reflecting the diastolic Ca-voltage coupling gain required to trigger an AP in a virtual 2D tissue of 25x25 coupled myocytes) is listed for each case. Although the absolute values of the NCX Multiplier differed for the 3 analysis methods, the latency distribution and SR Ca load had the largest and roughly equivalent effects (see text) on the NCX Multiplier, with the CaT duration exerting a smaller effect.

Chapter 4: Delayed afterdepolarizations generate both triggers and a vulnerable substrate promoting reentry in cardiac tissue

Abstract

Background: Delayed afterdepolarizations (DADs) have been well-characterized as arrhythmia triggers but their role in generating a tissue substrate vulnerable to reentry is not well understood. **_Objective_**: To test the hypothesis that random DADs can self-organize to generate both an arrhythmia trigger and a vulnerable substrate simultaneously in cardiac tissue as a result of gap junction coupling. **_Methods:_** Computer simulations in one-dimensional cable and two-dimensional tissue models were carried out. The cellular DAD amplitude was varied by changing the strength of sarcoplasmic reticulum Ca release. Random DAD latency and amplitude in different cells were simulated using Gaussian distributions. **_Results_**: Depending on the strength of spontaneous sarcoplasmic reticulum Ca release and other conditions, random DADs in cardiac tissue resulted in the following behaviors: 1) triggered activity (TA); 2) a vulnerable tissue substrate causing unidirectional conduction block and reentry by inactivating Na channels; 3) both triggers and a vulnerable substrate simultaneously by generating TA in regions next to regions with subthreshold DADs susceptible to unidirectional conduction block and reentry. The probability of the latter two behaviors was enhanced by reduced Na channel availability, reduced gap junction coupling, increased tissue heterogeneity, and less synchronous DAD latency. **_Conclusions_**: DADs can self-organize in tissue to generate arrhythmia triggers, a vulnerable tissue substrate, and both simultaneously. Reduced Na channel availability and gap junction coupling potentiate this mechanism of arrhythmias, which are relevant to a variety of heart disease conditions.

Introduction

Delayed afterdepolarizations (DADs) are transient depolarizations in the diastolic phase following an action potential (AP) that have been linked to arrhythmogenesis in cardiac diseases [1-3]. Experimental studies have revealed that the primary cause of DADs is spontaneous sarcoplasmic reticulum (SR) calcium (Ca) release, which activates Ca-sensitive inward currents such as the Na-Ca exchange current to depolarize diastolic membrane potential. Ca waves are promoted under Ca overload conditions in normal myocytes [4, 5] or under diseased conditions, such as heart failure [6-8], ischemia [9], catecholaminergic polymorphic ventricular tachycardia (CPVT) [10], and long QT syndromes [11, 12].

The role of DADs in arrhythmogenesis is generally explained as follows: when the amplitude of a DAD is above a certain threshold (termed a *suprathreshold* DAD), it can trigger an AP, called triggered activity (TA), which can cause a premature ventricular contraction (PVC) to trigger reentrant or focal arrhythmias [3, 13]. However, not all DADs are large enough to trigger APs, and the role of these *subthreshold* DADs in arrhythmogenesis is not well understood. It is well known that elevation of resting membrane potential can cause conduction slowing and block [14]. Elevation of the resting membrane potential of a ventricular myocyte will first enhance conduction by moving the potential closer to the sodium (Na) channel activation threshold, but further elevation will slow conduction due to Na channel inactivation. In an experimental study, Rosen et al [15] showed that impulses occurring during a DAD in a Purkinje fiber did not propagate to the ventricles, whereas earlier or later impulses did, suggesting that DADs can cause conduction block in Purkinje fibers. However, to our knowledge, no other studies have been carried out to investigate the role of subthreshold DADs as causes of conduction block and/or reentry.

The amplitude and latency of diastolic Ca waves tend to vary irregularly from beat-to-beat due to random properties of spontaneous SR Ca release [5, 16, 17], which can be further enhanced because of cell-to-cell or regional heterogeneities in Ca cycling properties [3, 18]. However, myocytes in cardiac tissue are coupled via gap junctions which tends to smooth the voltage differences between adjacent cells, synchronizing their depolarizations locally. These two competing factors could interact to generate regions of tissue with suprathreshold DADs causing TA bordering on regions with subthreshold DADs susceptible to conduction block, initiating reentry.

Based on this reasoning, we hypothesized that depending on the SR Ca release strength and other conditions, random DADs can self-organize in tissue to cause: 1) arrhythmia triggers by generating PVCs; 2) a vulnerable tissue substrate causing unidirectional conduction block of a PVC; and 3) both simultaneously resulting in initiation of reentry. To test this hypothesis, we performed computer simulations in one-dimensional (1D) cables and two-dimensional (2D) tissue models. DADs were simulated by commanded SR Ca releases, similar to DADs induced in experiments by caffeine pulses [19] or local β-adrenergic agonist application [20]. Random DAD latency was simulated by randomly setting the SR Ca release time, and the amplitude of DAD was changed by varying the strength of the SR Ca release flux. The effects of Na channel availability, gap junction coupling, as well as other factors, were characterized.

Methods

Simulations were carried out in 1D cable and 2D tissue models. The partial differential equation governing voltage is

$$\frac{\partial V}{\partial t} = -I_{ion}/C_m + D(\frac{\partial^2 V}{\partial x^2} + \frac{\partial^2 V}{\partial y^2}) \qquad (1)$$

where V is the membrane voltage, C_m=1 μF/cm^2 is the membrane capacitance, and D is the diffusion constant (proportional to gap junction conductance) with its control value set as 0.0005 cm^2/ms. The AP model and generation of DADs were described previously by Xie et al [21]. The spontaneous SR Ca release strength is described by a parameter g_{spon} and the random latency of the release follows a Gaussian distribution of standard deviation σ. More details of the model and simulation methods were present in *Supplemental Materials*.

In the simulations, unless specified the maximum Na channel conductance (g_{Na}) was 12 pA/pF and the Na channel steady-state inactivation curve (h_∞) was left-shifted 5 mV, i.e., the $V_{1/2}$ was changed from -66 mV to -71 mV. Fig.4-1A shows example traces of DADs and TA for different g_{spon} values and Fig.4-1B shows the maximum voltage versus g_{spon}. The threshold for suprathreshold DADs or TA in a single cell was g_{spon}=0.066 ms^{-1} (arrow in Fig.4-1B) without the shift of h_∞ but with a 5 mV left-shift, it increased to 0.0695 ms^{-1}.

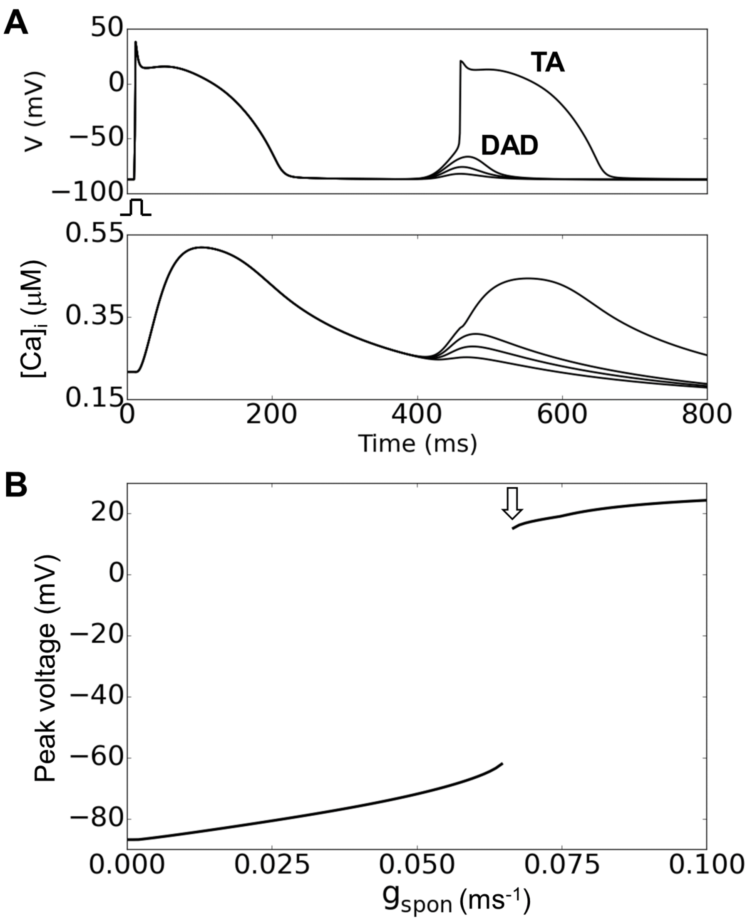

Figure 4-1. The DAD model

A. DADs and TA from a single isolated cell for different g_{spon} values. Upper traces show membrane potential and lower traces show the corresponding intracellular Ca concentrations. **B**. Maximum DAD voltage amplitude versus g_{spon}. The arrow indicates the g_{spon} threshold for a suprathreshold DAD eliciting TA.

Results

Effects of subthreshold DADs

Subthreshold DADs can cause conduction block when Na channel availability is reduced. We simulated a 1D cable in which the middle one-third of the cells exhibited DADs (Fig.4-2). We assumed that the spontaneous Ca releases causing DADs were identical and occurred at the same time in each cell (Fig.4-2A). A premature stimulus was applied to the first 10 cells at the end of the cable, and the ability of the AP to propagate to the other end of the cable was studied for different DAD amplitudes (adjusted by varying g_{spon}) and coupling intervals. For normal Na channel properties in our model, subthreshold DADs failed to cause conduction block, regardless of DAD amplitude or coupling interval. However, if Na channel availability was reduced by shifting the half-maximal voltage of steady-state inactivation (described by h_∞) in the negative direction, as might occur physiologically with PKA, PKC or CaMKII phosphorylation of Na channels [22] or in some Brugada syndrome mutations [23], conduction block occurred over a range of coupling intervals when DAD amplitude reached a critical range (Fig.4- 2B and C). In this range, the DAD-induced depolarization caused sufficient Na channel inactivation to result in conduction failure. Fig.4-2D illustrates the time course of Na channel availability (h*j) during a DAD with a peak voltage around -70 mV for control (solid) and for a 5 mV left-shift of h_∞ (dashed), showing that a 5 mV left-shift causes a large reduction in Na channel availability during the DAD. As the DAD amplitude was increased further (g_{spon}>0.0695 ms^{-1}), TA occurred in the DAD region, which propagated in both directions and collided retrogradely with the premature beat. Fig.4-2E plots

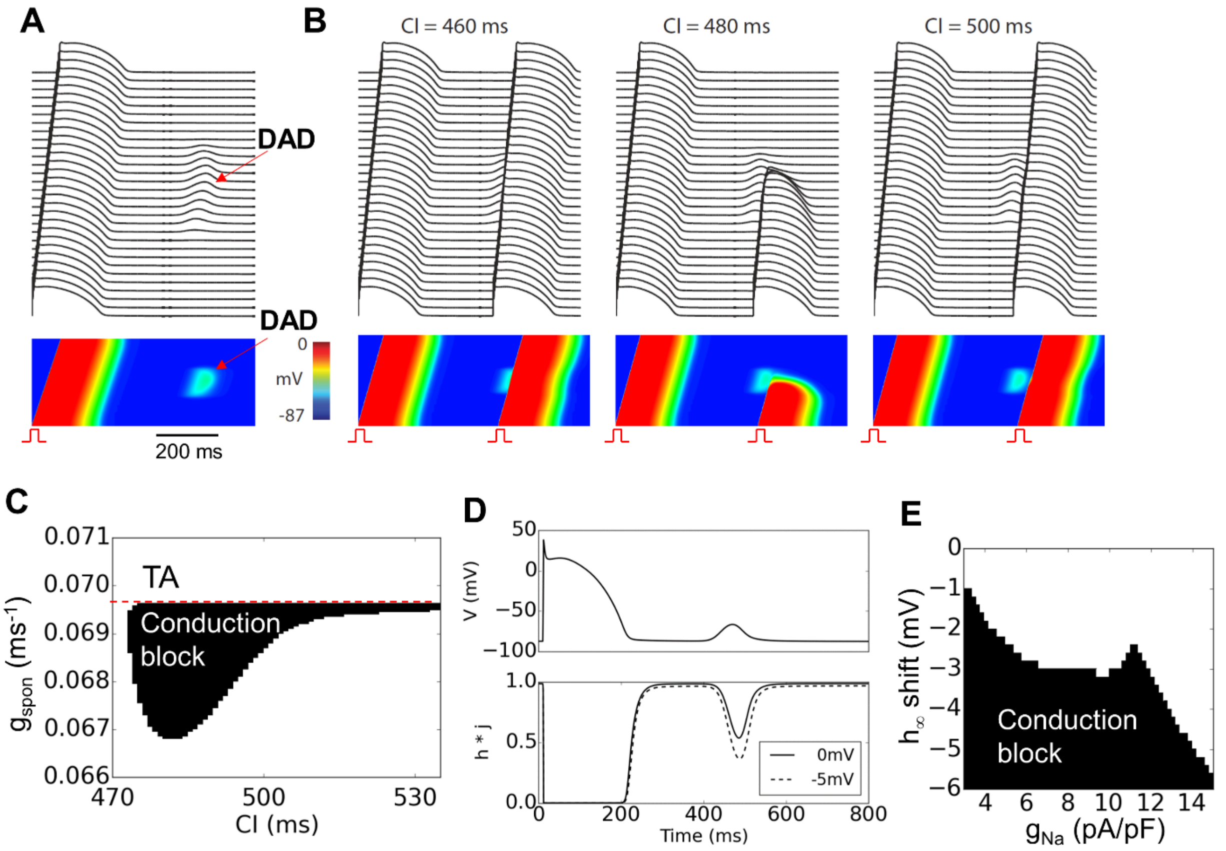

Figure 4-2. Conduction block due to a subthreshold DAD in a 1D cable.

A. A 300 cell cable is paced at a cycle length of 500 ms and a subthreshold DAD occurs in the middle 100 cells approximately 450 ms after the AP upstroke. Upper traces show membrane potential of every 10th cell, and lower trace shows a space-time plot of voltage along the cable. **B**. Under the same conditions, a premature stimulus elicited an AP (PVC) which propagated into the DAD region. When the coupling interval (CI) of the PVC was 460 ms (left panel) or 500 ms (right panel), the PVC propagated successfully to the other end of the cable. For the CI of 480 ms (middle panel), however, conduction block occurred in the DAD region. **C**. A parameter diagram showing conduction block (in black) as a function of CI and g_{spon}. Dashed line indicates the transition from a subthreshold to suprathreshold DAD causing TA at g_{spon}=0.0695 ms^{-1}. **D**. Voltage and Na channel availability (h*j) versus time for the un-shifted (solid) and 5 mV left-shifted (dashed) h_∞ during a DAD. **E**. Conduction block as a function of g_{Na} and left-shift of h_∞.

the region of conduction block versus the left-shift of h_∞ and g_{Na}, showing that reducing g_{Na} also promoted conduction block.

Effects of random DAD latency. In the simulations in Fig.4-2, the spontaneous Ca releases causing a DAD in the mid-region of the cable all occurred synchronously by design. To study the effects of random DAD latency, we simulated a 1D cable in which the latency of the spontaneous Ca release event for each cell was randomly assigned from a Gaussian distribution. Gap junction coupling naturally smoothed the resulting DAD in the tissue (Fig.4-3A). Unlike the non-random case in Fig.4-2, a premature beat with a fixed coupling interval could either block or propagate successfully through the DAD region depending on the particular randomization pattern of the trial (Fig.4-3B). In Figs.3C-E, we show the probability of conduction failure through the DAD region versus the strength of spontaneous Ca release (g_{spon}) for different standard deviations (σ) of the Gaussian distribution of latencies, g_{Na}, and gap junction coupling. Increasing σ caused conduction block to occur over a broader range of g_{spon}. Note that in the non-random case, TA occurred when $g_{spon}>0.0695$ ms^{-1} and no conduction block occurred. With random latency, a higher g_{spon} was required to trigger APs due to the source-sink effects, and conduction block still occurred when $g_{spon} >0.0695$ ms^{-1}. Reducing g_{Na} increased the probability of conduction block, while reducing gap junction coupling had a small effect.

If we applied the same deterministic or random DAD distribution as in the 1D cables (Figs. 2 and 3) to 2D tissue, reentry could be induced by a premature stimulus (see Movie 4-1 and Movie 4-2).

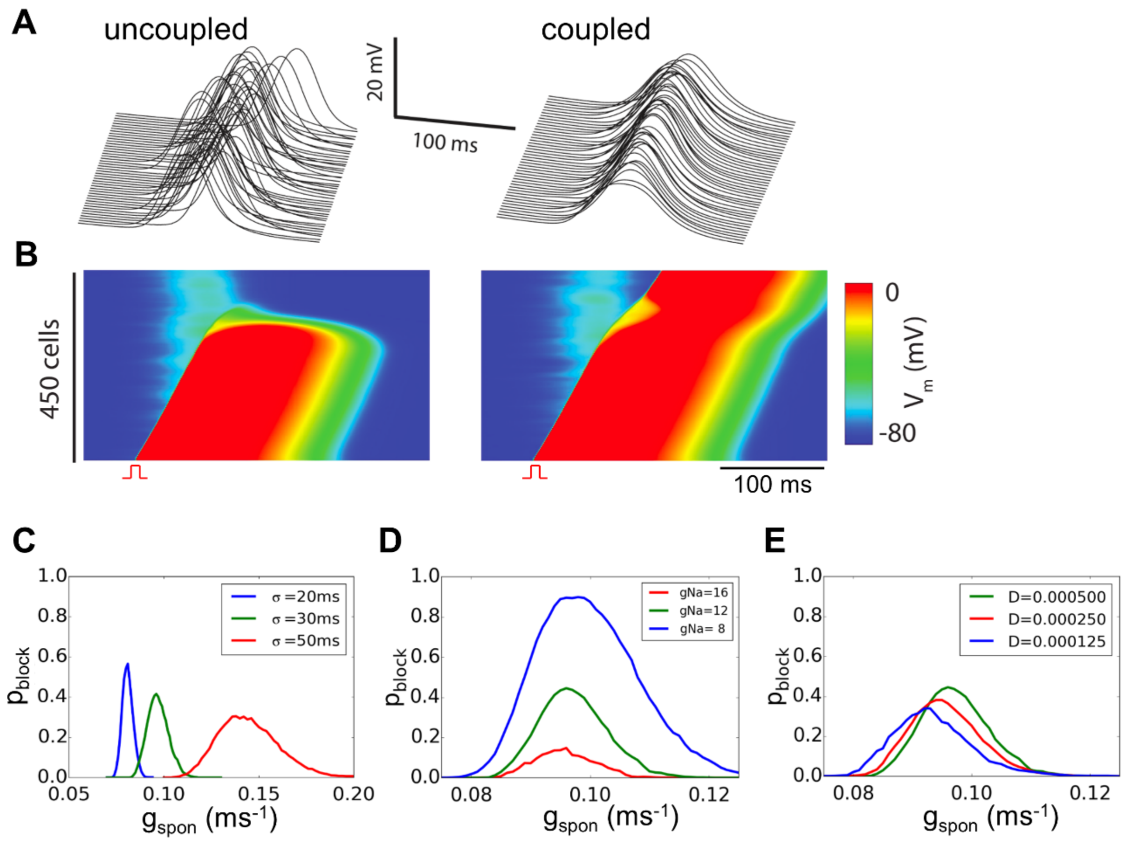

Figure 4-3. Effects of DAD synchronization on conduction block.

A. Random DAD latency when the cells in a 1D cable are electrically uncoupled (left) or coupled by gap junctions (right), illustrating the synchronizing effect of coupling on the tissue DAD. **B**. Voltage snapshots showing two different trials in which DAD latencies were randomly selected from a Gaussian distribution with a standard deviation (σ) of 20 ms. The resulting subthreshold tissue DADs were sufficiently different to cause an identically-timed PVC to block in one trial (left), but successfully propagate in the other trial (right). **C-E**. Probability of conduction block (p_{block}) versus g_{spon} for different σ (C), g_{Na} (D), and D (E) in a cable length of 450 cells. The probability of each parameter point was calculated from 1,000 random trials. The green curve in C-E is the control case with σ=30 ms, D=0.0005 cm^2/ms, g_{Na}=12 pA/pF, and a -5 mV shift of h_∞.

Combined effects of supra- and sub-threshold DADs

In the simulations shown above, external paced premature stimuli were used to illustrate how DADs can cause conduction block. We next examined whether TA self-generated by DADs could develop conduction block in the same cable due to random latency of DADs in different regions causing both subthreshold and suprathreshold DADs.

Complex excitation patterns in 1D cable. We carried out simulations in a homogeneous 1D cable with random DAD latency as in Fig.4-3 without externally paced premature stimuli. Complex excitation patterns occurred, which could be classified into three categories: 1) subthreshold DADs without TA (Fig.4-4A); 2) suprathreshold DADs causing TA which propagated successfully along the cable without conduction block (Fig.4-4B); and 3) suprathreshold DADs causing TA which propagated partway before developing conduction block (Fig.4-4C). Fig.4-4D shows the probability of the three behaviors as a function of DAD amplitude (g_{spon}). No TA occurred when g_{spon} was small, but as g_{spon} increased the incidence of TA also increased (dashed in Fig.4-4D). Due to random latency and cell coupling, the g_{spon} threshold for TA was higher in tissue than in a single cell (g_{spon}>0.0695 ms^{-1}). Figs.4E-H show that the probability of block increases with broadened latency distribution (Fig.4-4E), decreased cell coupling (Fig.4-4F), reduced g_{Na} (Fig.4-4G), and left-shifted h_∞ (Fig.4-4H).

Reentry initiation in 2D tissue. Unidirectional conduction block of DAD-mediated TA in the 1D cable raises the possibility that under similar conditions in 2D tissue, reentry may be induced when conduction block is appropriately localized. Analogous to the 1D simulations in Figs.3 and 4, we first simulated a homogeneous 2D tissue in which all cells were identical with the same

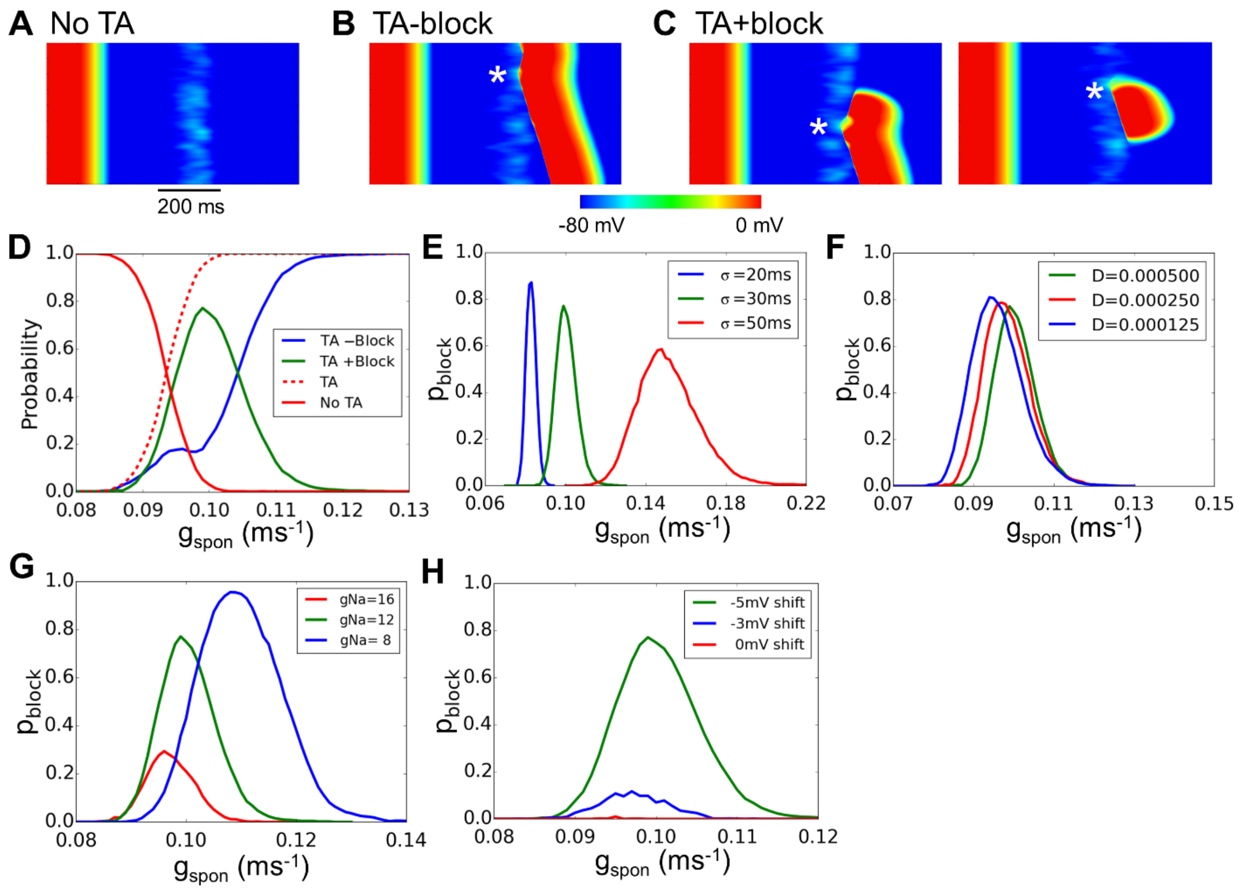

Figure 4-4. **Complex excitation patterns in a 1D cable**.

A-C. Space-time plots of membrane potential versus time in a 300 cell cable in which all cells exhibited DADs with randomly assigned latencies (σ=50 ms) following a paced AP. g_{spon}=0.15 ms^{-1}. **D**. Probability of no TA (red), a successfully propagating TA (blue) and a TA with conduction block (green) versus g_{spon} for σ=30 ms. Arrow indicates the g_{spon} threshold for TA. **E**. Probability of conduction block versus g_{spon} for different σ. **F**. Probability of conduction block versus g_{spon} for different diffusion coefficients (D) reflecting gap junction coupling. **G**. Probability of conduction block versus g_{spon} for different g_{Na}. **H**. Probability of conduction block versus g_{spon} for shifts in the half-maximal voltage of h_∞. The cable length in D-H was 450 cells. The probability of each parameter point was calculated from 1,000 random trials. The green curve in D-H is the control case with σ=30 ms, D=0.0005 cm^2/ms, g_{Na}=12 pA/pF, and a -5 mV shift of h_∞.

DAD amplitude (i.e., identical g_{spon}) but DAD latencies were randomly assigned following a Gaussian distribution. Both subthreshold DADs and TA were observed, but in over 10,000 simulations using different parameter settings, reentry was never observed, even when g_{Na} or gap junction coupling was reduced.

Since Ca release properties in real cardiac tissue are not homogeneous, we then performed simulations in which g_{spon} was varied in random checkerboard patterns, drawing from a Gaussian distribution, as illustrated in Fig.4-5A. Checker sizes ranged from 1x1 to 256x256 cells. The DAD latencies were still varied randomly from cell to cell as in the simulations above. We observed three behaviors (Fig.4-5B): all DADs are subthreshold (no TA); DADs induce TA without reentry formation (TA without reentry), and DADs induce TA with reentry formation (TA with reentry). Fig.4-5C shows the probability of these different behaviors versus the checker size for control parameters. For large checker sizes, the majority of the simulations exhibited TA without reentry (i.e., PVCs only), and a small number of the simulations exhibited reentry. As the checker size decreased, the probability of TA without reentry decreased, while that of subthreshold DADs increased. Interestingly, the probability of reentry first increased and then decreased to zero at small checker sizes. Reducing gap junction conductance selectively increased the probability of reentry at large and small checker sizes (Fig.4-5D), but suppressed reentry at intermediate checker sizes. Reducing Na channel conductance g_{Na} in steps from 16 to 8 pS/pF increased the probability of reentry particularly at large checker sizes, while further reduction to 6 pS/pF suppressed reentry due to low excitability (Fig.4-5E). Fig.4-5F compares the probability of TA with and without reentry versus g_{Na}. As g_{Na} was reduced, the probability of TA without reentry decreased while the probability of TA with reentry first increased then decreased. We also

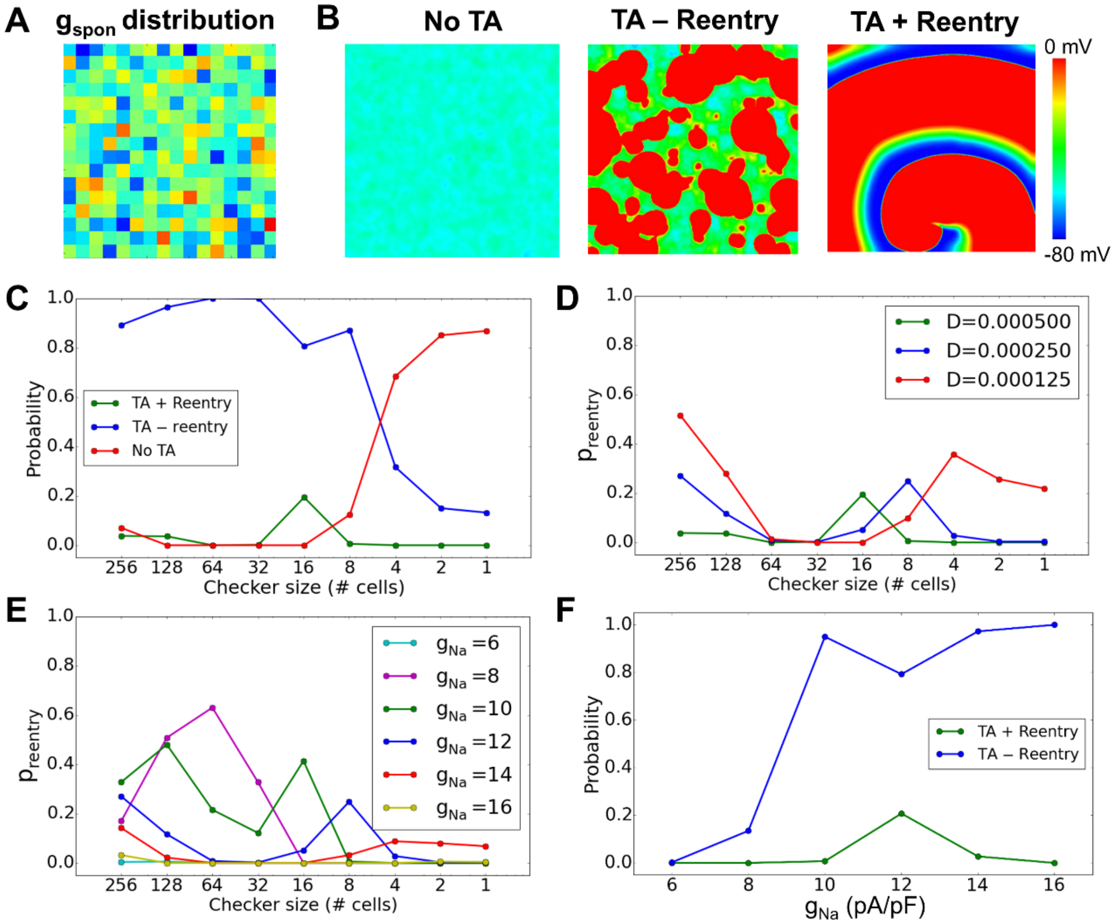

Figure 4-5. Summary data for reentry induction in heterogeneous 2D tissue.

A. An example of checkerboard g_{spon} distribution. g_{spon} in each checker was drawn from a random Gaussian distribution with an average value of 0.172 ms^{-1} and a standard deviation σ=0.03 ms^{-1}. **B**. Examples of voltage snapshots illustrating no TA, TA-reentry, and TA+reentry. **C**. Probability of TA+reentry (green), TA-reentry (blue), and no TA (red) versus checker size. The dashed line is the total probability of TA. **D**. Probability of reentry versus checker size for different diffusion coefficients (D, cm^2/ms). **E**. Probability of reentry for different g_{Na}. **F**. Probability of TA-reentry and TA+reentry versus g_{Na} for an 8x8 checker size. The standard deviation for random DAD latency of individual cells was σ=50 ms. The tissue size was 512 x 512 cells. The probability of each parameter point was calculated from 500 random trials.

performed simulations in which g_{spon} was varied randomly in checkerboard patterns, but DAD latency was fixed. We never observed reentry, indicating that the random DAD latency is a key property promoting reentry. This was also supported by simulations investigating the effect of DAD latency distribution on reentry in 2D tissue, which depended sensitively on σ (Fig.4-S1).

Finally, we examined how electrical remodeling in heart failure affects DAD-mediated arrhythmogenesis (Fig.4-6). Electrical remodeling decreased the threshold of g_{spon} required for conduction block (Fig.4-6A) and greatly decreased the g_{spon} required for TA with reentry (Fig.4-6B). Similar to Fig.4-5F, decreasing g_{Na} reduced the probability of TA without reentry and first increased then decreased the probability of TA with reentry (Fig.4-6C).

As shown in Figs.5 and 6, checker size had a non-monotonic effect on probability of reentry. A possible explanation is illustrated in Fig.4- 7, which shows voltage snapshots for three different checker sizes with reduced gap junction coupling. For the 256x256 case (Fig.4-7A and Movie 4-3), the randomness of DAD latency resulted in nonuniform DAD voltages in a single checker, allowing conduction in one direction but block in another direction at the borders of the individual checkers. Due to the large checker size, there was enough room for the broken wavefronts to turn and reenter the checker from another direction. For the 32x32 case (Fig.4-7B and Movie 4-4), TA that formed in the individual checkers tended to propagate neatly in all directions and fuse together, such that there was not enough unexcited tissue for a broken wavefront to form a spiral wave. For the 1x1 case (Fig.4-7C and Movie 4-5), the checkers with high g_{spon} values were not large enough to generate TA individually unless neighboring checkers also had randomly been assigned large enough g_{spon} values to overcome the source-sink mismatch. This effectively resulted in large heterogeneous regions with or without TA, increasing the probability of reentry. Note that when the gap junction coupling was normal, however, no reentry could occur for the 1x1 case (Fig.4-5C).

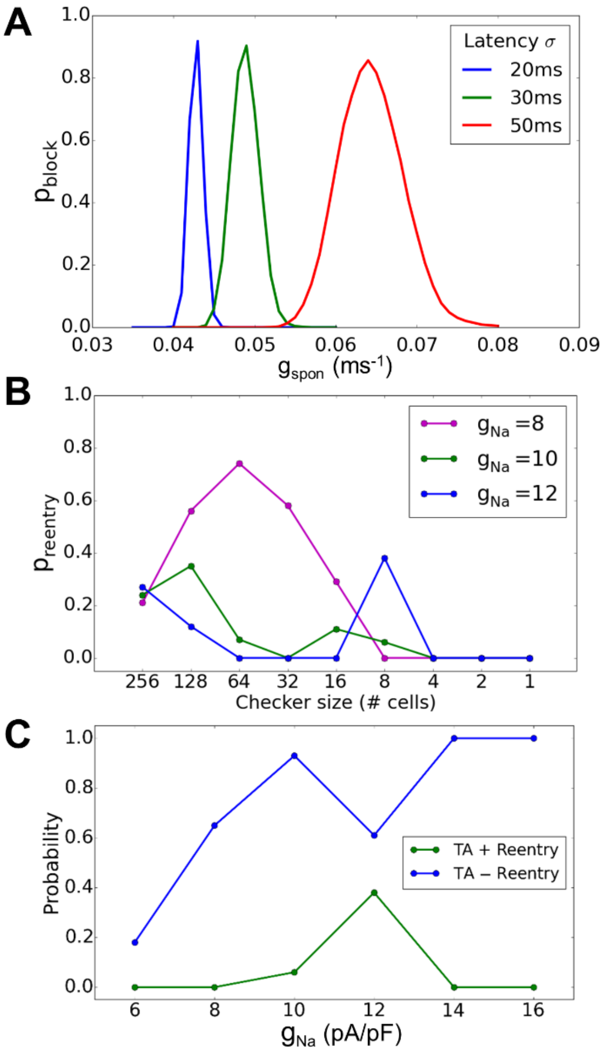

Figure 4-6. Conduction block and reentry in heart failure.

Heart failure was simulated as described in Xie et al [21]. **A.** Probability of conduction block in a 1D cable versus g_{spon} for different DAD latency σ. The g_{spon} range for conduction block is lower than in the non-failing condition (Fig.4E). **B.** Probability of TA+reentry (green) versus checker size in a 2D tissue of failing cells for different g_{Na}. g_{spon} was drawn from a Gaussian distribution with an average value of 0.065 ms^{-1} and a standard deviation of σ=0.02 ms^{-1}. The DAD latency standard deviation σ=50 ms. **C**. Probability of TA-reentry and TA+reentry versus g_{Na}.

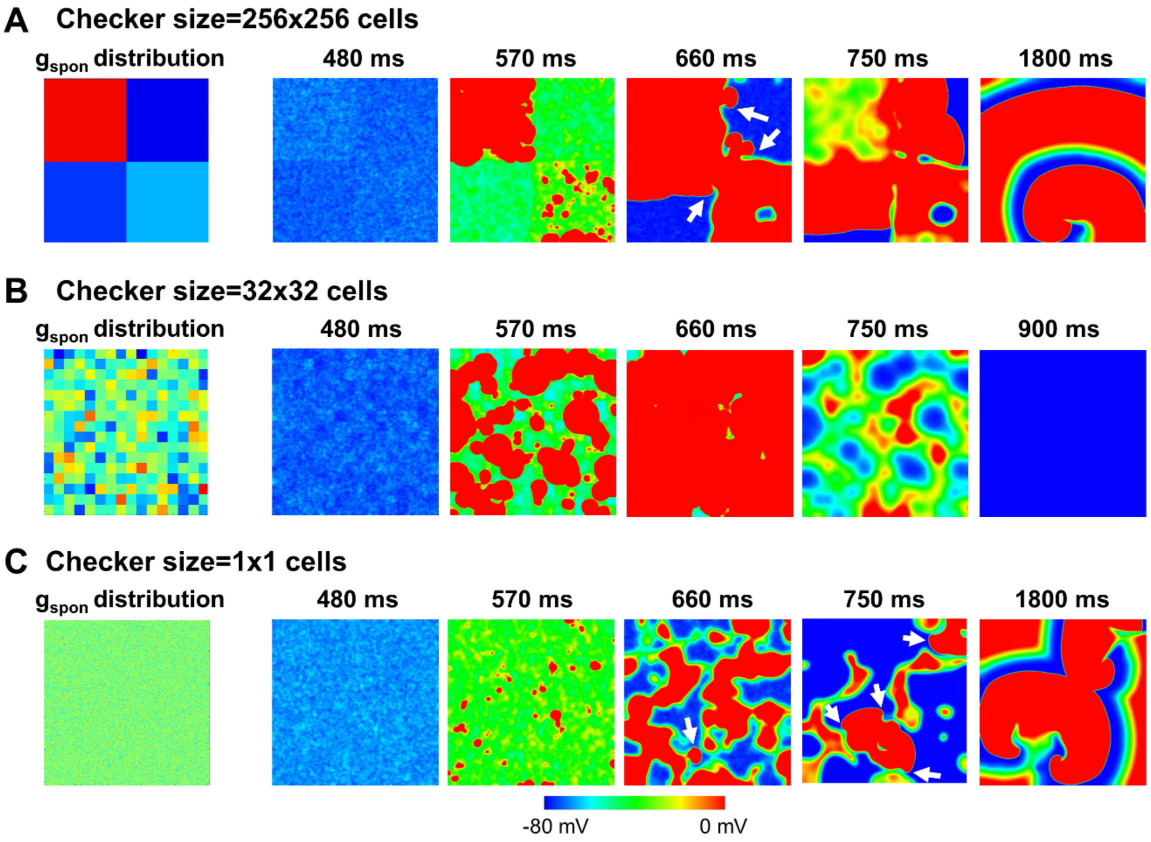

Figure 4-7. Voltage snapshots for three different checker sizes in heterogeneous 2D tissue.

Left panels show the g_{spon} distributions and right panels show corresponding voltage snapshots of DAD-mediated TA and conduction block at various times following a paced AP, with checker sizes of 256x256 (**A**), 32x32 (**B**), and 1x1 cells (**C**).

Discussion

DADs are classically recognized as triggers of PVCs that can initiate reentry when they encounter a vulnerable tissue substrate. Here we demonstrate that subthreshold DADs can also directly generate a tissue substrate vulnerable to unidirectional conduction block. Moreover, DAD-induced triggers and substrates can occur simultaneously in the same tissue to induce reentry. These effects are enhanced with reduced Na channel availability and gap junction coupling, with electrical remodeling changes in heart failure, and when regional differences in Ca cycling properties underlying DADs are accentuated, as occurs in the setting of heart diseases. Our observations thus provide novel insights into DAD-related arrhythmogenesis.

Roles of DADs in cardiac arrhythmogenesis

Based on observations in the present study, we can summarize the roles of DADs in cardiac arrhythmogenesis as follows:

DADs generate arrhythmia triggers. The well-known effect of suprathreshold DADs in cardiac arrhythmogenesis is their ability to trigger an AP and generate TA, which can cause focal (non-reentrant) arrhythmias or serve as PVCs to initiate reentrant arrhythmias [1-3, 24, 25].

DADs generate a vulnerable substrate. Traditionally, dispersion of excitability and/or refractoriness make a tissue vulnerable to initiation of reentry by a trigger such as a PVC [26]. Unidirectional conduction block initiating reentry occurs either because the Na current has not recovered sufficiently from inactivation to overcome the source-sink mismatch of neighboring repolarized cells (dispersion of excitability) or the neighboring cells are still in a refractory state (dispersion of refractoriness). In this study, we have demonstrated that subthreshold DADs can cause unidirectional conduction block via the former mechanism by elevating diastolic membrane potential and inactivating Na channels sufficiently to cause conduction block. The random distribution of DAD latency increases the probability of conduction block (Fig.4-3) because as DAD latency distribution becomes wider, DAD duration in the tissue prolongs, giving more time for more Na channels to inactivate.

Since subthreshold DADs can occur at any time during diastole, a very late diastolic subthreshold DAD could potentially cause regional conduction block of a subsequent sinus beat, initiating reentry directly from sinus rhythm in the absence of a PVC. In this case, the first beat of reentrant ventricular tachycardia would have the same QRS morphology as subsequent tachycardia beats, which is frequently observed in clinical studies [27]. Thus, unlike reentrant arrhythmias induced by dispersion of refractoriness in which an external PVC is usually required, DAD-mediated reentrant arrhythmias do not necessarily require an external PVC, as the next sinus beat can serve to initiate reentry.

DADs simultaneously generate triggers and a vulnerable substrate. Due to random [5, 16, 17] and heterogeneous [3, 18] Ca release, DADs in tissue can lead to complex depolarization patterns in which some regions generate suprathreshold DADs causing TA, while other regions generate subthreshold DADs promoting regional conduction block and initiation of reentry (Figs.4-7). TA generated in one region may propagate in all or only in one direction, or be blocked a distance away such that reentry can result if the broken wavefronts have enough available excitable tissue. Although the interactions among random latency, heterogeneity, gap junction coupling and Na channel availability are complex, the probability of conduction block and reentry increases for reduced gap junction coupling, Na current availability and electrical remodeling. Our simulations also show that both random latency and heterogeneous Ca release are needed for reentry to occur.

Clinical relevance

As shown in our simulations (Figs.4-6), a negative shift in the steady state inactivation curve and/or reduction of the maximal Na conductance increased the probability of conduction block and reentry in the presence of DADs. This condition is physiologically mimicked by PKA- and/or PKC-mediated phosphorylation of Na channels during sympathetic stimulation or CaMKII-mediated phosphorylation of Na channels in the setting of heart failure [22], Na channel remodeling in ischemic heart disease [28] or loss-of-function Na channel mutations in Brugada syndrome [23] and other diseases [29].

Since Class I antiarrhythmic agents not only reduce the Na channel open probability but also left-shift the steady-state inactivation curve [30], this may have been a contributing factor to the proarrhythmic effects of Na channel blockers observed in the CAST trial [31]. In the CAST trial, Na channel blockers effectively suppressed PVCs by more than 80%, but mortality nevertheless increased due to more frequent lethal arrhythmic events. Many later studies established that blocking the Na channel is proarrhythmic in ischemic and infarcted tissue, due to lowered excitability and increased post-repolarization refractoriness in the border zone [28, 30]. Our simulations suggest that an additional mechanism could also be important: if the PVCs in these patients originated from Ca wave-mediated DADs, then reducing excitability by blocking Na channels could have reduced the frequency of benign PVCs by converting suprathreshold DADs to subthreshold DADs, while at the same time paradoxically increasing the probability that the less frequent remaining suprathreshold DADs will initiate reentry. This phenomenon was illustrated in Figs.4-5F and 4-6C, in which reducing Na channel conductance reduced the incidence of TA without reentry (benign PVCs) but increased the probability of TA with reentry (malignant PVCs initiating VT/VF) over a certain range of g_{Na}.

Finally, PVCs can originate from either the His-Purkinje system or ventricular myocardium in patients, and may exhibit simple patterns in the ECG, such as fixed QRS morphology (unifocal PVCs) and fixed coupling interval, or complex patterns such as different QRS morphologies (multifocal PVCs) and varying coupling intervals (modulated parasystole). For the mechanisms described in this study, we can speculate that PVCs arising from an abnormal area in the His-Purkinje system would tend to produce unifocal PVCs with some degree of variation in coupling intervals. In ventricular tissue, on the other hand, the random process by which Ca waves in individual myocytes self-organize to generate suprathreshold vs. subthreshold DADs in different regions of tissue would likely produce multifocal PVCs with variable coupling intervals. Another potential insight from the current study relates to the hypothesis subthreshold DADs occurring in ventricles may be one of the mechanisms underlying U-waves in the ECG [32], as supported by recent experimental studies [13]. Based on our finding that subthreshold DADs also can create vulnerable substrate for reentry, it is intriguing to speculate that PVCs accompanying U-waves in the ECG may confer a higher arrhythmia risk than when U-waves are absent.

Limitations

A limitation of this study is that the DADs in our model were caused by commanded SR Ca releases with randomly distributed amplitude and/or latency following Gaussian distributions, which allowed us to readily control DAD amplitude and latency. To realistically simulate spontaneous Ca release via the mechanism of Ca-induced Ca release and the feedback between Ca and voltage requires a detailed Ca cycling model incorporating random RyR openings [5, 33, 34]. However, since we studied only the effects of voltage depolarization on conduction block and not the feedback between Ca and voltage or other excitation-contraction dynamics, the simulation results from the present study still provides important mechanistic insights into arrhythmias caused by DADs. We altered DAD amplitude by increasing spontaneous SR Ca release, but DAD amplitude can also be regulated by the diastolic Ca-voltage coupling gain [35], which we did not study except in the context of heart failure electrical remodeling (Fig.4- 6). We also did not explicitly study the effects of altering DAD duration at the cellular level, which in real cells is sensitive to the subcellular location and numbers of sites from which Ca waves originate. Our 1D and 2D tissue models are relatively simple compared to real tissue, and the results may influenced by specific structural features of the tissue. For example, as shown in Fig.4-5, the proarrhythmic effects of blocking Na channels or reducing gap junction conductance depended on the specific spatial characteristics of heterogeneities. Nevertheless, the insights from computer modeling in this study have uncovered novel mechanisms for DAD-mediated arrhythmogenesis that provide testable hypotheses for future experimental studies.

Conclusions

Whereas suprathreshold DADs in cardiac tissue generate triggers for reentrant arrhythmias, subthreshold DADs can create regions susceptible to unidirectional conduction block, directly increasing the probability that the triggers will induce reentry. This scenario is unlikely when Na channel properties are normal, but becomes increasingly probable as Na channel availability is reduced by sympathetic stimulation, disease-related remodeling, loss-of-function genetic defects, or Class I antiarrhythmic drugs, and as gap junction coupling is reduced by gap junction remodeling or fibrosis. These dynamics provide novel mechanistic insights into DAD-mediated arrhythmogenesis potentially relevant to a spectrum of cardiac diseases such as chronic ischemia, heart failure, Brugada syndrome and CPVT, as well as the proarrhythmic effects of Na channel blockers.

References

1. Rosen, M.R., J.P. Moak, and B. Damiano, *The clinical relevance of afterdepolarizations.* Ann N Y Acad Sci, 1984. **427**: p. 84-93.
2. January, C.T. and H.A. Fozzard, *Delayed afterdepolarizations in heart muscle: mechanisms and relevance.* Pharmacol Rev, 1988. **40**(3): p. 219-27.
3. Katra, R.P. and K.R. Laurita, *Cellular mechanism of calcium-mediated triggered activity in the heart.* Circ Res, 2005. **96**(5): p. 535-42.
4. Cheng, H., et al., *Calcium sparks and [Ca2+]i waves in cardiac myocytes.* Am J Physiol, 1996. **270**(1 Pt 1): p. C148-59.
5. Nivala, M., et al., *Criticality in intracellular calcium signaling in cardiac myocytes.* Biophys J, 2012. **102**(11): p. 2433-42.
6. Yeh, Y.H., et al., *Calcium-handling abnormalities underlying atrial arrhythmogenesis and contractile dysfunction in dogs with congestive heart failure.* Circ Arrhythm Electrophysiol, 2008. **1**(2): p. 93-102.
7. Pogwizd, S.M. and D.M. Bers, *Calcium cycling in heart failure: the arrhythmia connection.* J Cardiovasc Electrophysiol, 2002. **13**(1): p. 88-91.
8. Hoeker, G.S., et al., *Spontaneous calcium release in tissue from the failing canine heart.* Am J Physiol Heart Circ Physiol, 2009. **297**(4): p. H1235-42.
9. Ross, J.L. and S.E. Howlett, *ß-adrenoceptor stimulation exacerbates detrimental effects of ischemia and reperfusion in isolated guinea pig ventricular myocytes.* European Journal of Pharmacology, 2009. **602**(2–3): p. 364-372.
10. Watanabe, H., et al., *Flecainide prevents catecholaminergic polymorphic ventricular tachycardia in mice and humans.* Nat Med, 2009. **15**(4): p. 380-3.
11. Mohler, P.J., et al., *Ankyrin-B mutation causes type 4 long-QT cardiac arrhythmia and sudden cardiac death.* Nature, 2003. **421**(6923): p. 634-639.
12. Burashnikov, A. and C. Antzelevitch, *Acceleration-induced action potential prolongation and early afterdepolarizations.* Journal of Cardiovascular Electrophysiology, 1998. **9**(9): p. 934-48.
13. Morita, H., et al., *Mechanism of U wave and polymorphic ventricular tachycardia in a canine tissue model of Andersen-Tawil syndrome.* Cardiovasc Res, 2007. **75**(3): p. 510-8.
14. Singer, D.H., R. Lazzara, and B.F. Hoffman, *Interrelationship between automaticity and conduction in Purkinje fibers.* Circ Res, 1967. **21**(4): p. 537-58.
15. Rosen, M.R., A.L. Wit, and B.F. Hoffman, *Electrophysiology and pharmacology of cardiac arrhythmias. IV. Cardiac antiarrhythmic and toxic effects of digitalis.* Am Heart J, 1975. **89**(3): p. 391-9.

16. Wasserstrom, J.A., et al., *Variability in timing of spontaneous calcium release in the intact rat heart is determined by the time course of sarcoplasmic reticulum calcium load.* Circ Res, 2010. **107**(9): p. 1117-26.

17. Fujiwara, K., et al., *Burst Emergence of Intracellular Ca2+ Waves Evokes Arrhythmogenic Oscillatory Depolarization via the Na+-Ca2+ Exchanger: Simultaneous Confocal Recording of Membrane Potential and Intracellular Ca2+ in the Heart.* Circ Res, 2008. **103**(5): p. 509-518.

18. Plummer, B.N., et al., *Spontaneous calcium oscillations during diastole in the whole heart: the influence of ryanodine reception function and gap junction coupling.* Am J Physiol Heart Circ Physiol, 2011. **300**(5): p. H1822-H1828.

19. Schlotthauer, K. and D.M. Bers, *Sarcoplasmic reticulum Ca(2+) release causes myocyte depolarization. Underlying mechanism and threshold for triggered action potentials.* Circ Res, 2000. **87**(9): p. 774-80.

20. Myles, R.C., et al., *Local β-Adrenergic Stimulation Overcomes Source-Sink Mismatch to Generate Focal Arrhythmia.* Circulation Research, 2012. **110**(11): p. 1454-1464.

21. Xie, Y., et al., *So little source, so much sink: requirements for afterdepolarizations to propagate in tissue.* Biophys J, 2010. **99**(5): p. 1408-15.

22. Herren, A.W., D.M. Bers, and E. Grandi, *Post-translational modifications of the cardiac Na channel: contribution of CaMKII-dependent phosphorylation to acquired arrhythmias.* Am J Physiol Heart Circ Physiol, 2013. **305**(4): p. H431-45.

23. Hu, D., et al., *A Mutation in the β3 Subunit of the Cardiac Sodium Channel Associated With Brugada ECG Phenotype.* Circulation: Cardiovascular Genetics, 2009. **2**(3): p. 270-278.

24. Pogwizd, S.M. and D.M. Bers, *Cellular basis of triggered arrhythmias in heart failure.* Trends Cardiovasc Med, 2004. **14**(2): p. 61-6.

25. Rubart, M. and D.P. Zipes, *Mechanisms of sudden cardiac death.* J Clin Invest, 2005. **115**(9): p. 2305-15.

26. Qu, Z. and J.N. Weiss, *Mechanisms of Ventricular Arrhythmias: From Molecular Fluctuations to Electrical Turbulence.* Annual Review of Physiology, 2015. **77**(1): p. 29-55.

27. Saeed, M., et al., *Analysis of intracardiac electrograms showing monomorphic ventricular tachycardia in patients with implantable cardioverter-defibrillators.* Am J Cardiol, 2000. **85**(5): p. 580-7.

28. Pu, J. and P.A. Boyden, *Alterations of Na+ currents in myocytes from epicardial border zone of the infarct heart: A possible ionic mechanism for reduced excitability and postrepolarization refractoriness.* Circ. Res., 1997. **81**(1): p. 110-119.

29. Grant, A.O., et al., *Long QT syndrome, Brugada syndrome, and conduction system disease are linked to a single sodium channel mutation.* The Journal of Clinical Investigation, 2002. **110**(8): p. 1201-1209.

30. Pu, J.L., J.R. Balser, and P.A. Boyden, *Lidocaine action on Na+ currents in ventricular myocytes from the epicardial border zone of the infarcted heart.* Circulation Research, 1998. **83**(4): p. 431-440.

31. Echt, D.S., et al., *Mortality and morbidity in patients receiving encainide, flecainide, or placebo. The Cardiac Arrhythmia Suppression Trial.* N Engl J Med, 1991. **324**(12): p. 781-8.

32. Surawicz, B., *U wave: facts, hypotheses, misconceptions, and misnomers.* J Cardiovasc Electrophysiol, 1998. **9**(10): p. 1117-28.

33. Chen, W., M. Asfaw, and Y. Shiferaw, *The Statistics of Calcium-Mediated Focal Excitations on a One-Dimensional Cable.* Biophysical journal, 2012. **102**(3): p. 461-471.

34. Song, Z., et al., *Calcium-Voltage Coupling in the Genesis of Early and Delayed Afterdepolarizations in Cardiac Myocytes.* Biophysical Journal, 2015. **108**(8): p. 1908-1921.

35. Maruyama, M., et al., *Diastolic intracellular calcium-membrane voltage coupling gain and postshock arrhythmias: role of purkinje fibers and triggered activity.* Circ Res, 2010. **106**(2): p. 399-408.

Supplemental Information

Supplemental Methods

Simulations were carried out in 1D cable and 2D tissue models. The partial differential equation governing voltage for the 1D cable is

$$\frac{\partial V}{\partial t} = -I_{ion}/C_m + D\frac{\partial^2 V}{\partial x^2} \qquad (1)$$

Where V is the membrane voltage, C_m=1 μF/cm^2 is the membrane capacitance, D is the diffusion constant (proportional to gap junction conductance) with its control value set as 0.0005 cm^2/ms. For 2D tissue, the equation for voltage is

$$\frac{\partial V}{\partial t} = -I_{ion}/C_m + D\left(\frac{\partial^2 V}{\partial x^2} + \frac{\partial^2 V}{\partial y^2}\right) \qquad (2)$$

The AP model and generation of DADs were described previously by Xie et al [1]. A spontaneous Ca release flux was formulated as $J_{spon}=g_{spon}g_1g_2(\beta c_j-c_s)$, where g_{spon} is the maximum conductance, β is the sub-membrane space/SR volume ratio, c_j and c_s are the Ca concentrations in the junctional SR and sub-membrane space, respectively. g_1 and g_2 are sigmoidal functions of time formulated as $g_1=1/(1+\exp(-(t-t_0)/\tau_1))$ and $g_2=1/(1+\exp((t-t_0)/\tau_2))$, where τ_1=10 ms and τ_2=30 ms, and t_0 determines the timing (latency) of the DAD. For suprathreshold DADs, J_{spon} was turned off at the onset of the TA upstroke and the L-type Ca current caused the SR Ca release during the TA as in a normal AP. For random latency, we used a Gaussian distribution as:

$$p(t_0) = \frac{1}{\sigma\sqrt{2\pi}}e^{-(t_0-\bar{t}_0)^2/2\sigma^2} \qquad (3)$$

In the simulations, unless specified the maximum Na channel conductance (g_{Na}) was 12 pA/pF and the Na channel steady-state inactivation curve (h_∞) was left-shifted 5 mV, i.e., the $V_{1/2}$ was changed from -66 mV to -71 mV. Fig.4-1A shows example traces of DADs and TA for different g_{spon} values and Fig.4-1B shows the maximum voltage versus g_{spon}. The threshold for suprathreshold DADs or TA in a single cell is g_{spon}=0.066 ms^{-1} (arrow in Fig.4-1B) without the shift of h_∞ but with a 5 mV left-shift, it becomes 0.0695 ms^{-1}(dashed line in Fig.4-2C).

Numerical simulations were carried out in workstations using computing graphics processing units (Tesla K20c, NVIDIA Corporation). Δx=Δy=0.015 cm, and an operator splitting and time adaptive algorithm [2] was used with time step (Δt) varying between 0.01 ms and 0.1 ms.

References

1. Xie, Y., et al., *So little source, so much sink: requirements for afterdepolarizations to propagate in tissue.* Biophys J, 2010. **99**(5): p. 1408-15.
2. Qu, Z. and A. Garfinkel, *An advanced numerical algorithm for solving partial differential equation in cardiac conduction.* IEEE Trans. Biomed. Eng., 1999. **49**(9): p. 1166-1168.

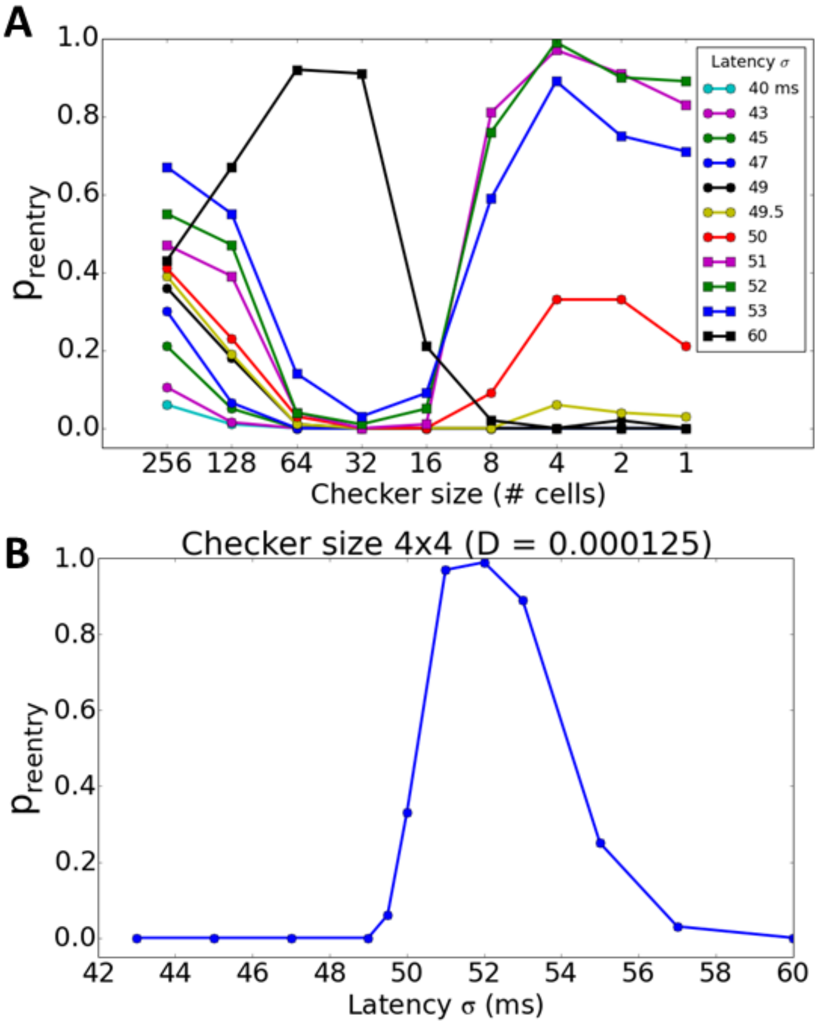

Figure 4-S1. Reentry dependence on DAD latency distribution.

A. Probability of reentry versus checker size for different latency standard deviations (σ). There is a different optimal σ for reentry at each checker size, which is related to the relative ease of TA propagation. When TA propagation is too difficult, there will be no suprathreshold DADs to trigger reentry; when TA propagation is too easy, there will be no subthreshold DADs to provide a substrate for reentry. A mixture is required for reentry, resulting in an optimal value.

B. Probability of reentry versus latency standard deviation (σ) for a single checker size 4x4cells. There is a narrow optimal range at this checker size for reentry.

Chapter 5: “R-from-T” as a common mechanism of arrhythmia initiation in long QT syndromes

Abstract

Background: Long QT syndromes (LQTS) arise from many genetic and non-genetic causes. Certain characteristic ECG features have been shown to precede polymorphic ventricular tachyarrhythmias (PVT) in patients of LQTS. However, how the many molecular causes result in these characteristic ECG patterns, and how these patterns are then mechanistically linked to the spontaneous initiation of PVT remain poorly understood.

Methods and Results: We used an anatomical human ventricle model to simulate spontaneous initiation of PVT in different LQTS genotypes. Spontaneous initiation of PVT was elicited by gradually ramping up $I_{Ca,L}$ or by changing the heart rate. In LQT2 and LQT3, as $I_{Ca,L}$ gradually ramped up, T-wave alternans was observed followed by premature ventricular complexes (PVCs). Compensatory pauses occurred via retrograde block of the sinus beats, resulting in short-long-short sequences. As $I_{Ca,L}$ increased further, episodes of PVT occurred, always preceded by a short-long-short sequence. However, in LQT1, once a PVC occurred it always immediately led to an episode of PVT without being preceded by T-wave alternans or short-long-short sequences. Arrhythmias in LQT2 and LQT3 were bradycardia-dependent while LQT1 was not. At high enough $I_{Ca,L}$ levels, PVT could be induced in LQT2 and LQT3 by suddenly slowing the heart rate, and in LQT1 by speeding up the heart rate. In all three genotypes, the PVCs always originated spontaneously from the steep repolarization gradient region and manifested on ECG as R-on-T. We call this mechanism “R-from-T”, to distinguish it from the classic explanation of R-on-T arrhythmogenesis in which an exogenous PVC coincidentally encounters

a repolarizing region resulting in conduction block and reentry. In R-from-T, the PVC and the T-wave are causally related, where QT prolongation results in steeper repolarization gradients which combined with enhanced $I_{Ca,L}$ leads to PVCs emerging from the T-wave. Since enhanced $I_{Ca,L}$ was required for R-from-T to occur, suppressing window $I_{Ca,L}$ effectively prevented arrhythmias in all three genotypes.

Conclusions: Despite the complex molecular causes of LQTS, R-from-T may be a common mechanism for PVT initiation in LQTS. Targeting $I_{Ca,L}$ properties, such as suppressing window $I_{Ca,L}$ or preventing excessive $I_{Ca,L}$ increase, could be an effective unified therapy for arrhythmia prevention in LQTS.

Introduction

QT prolongation is a major risk factor of ventricular arrhythmias and sudden cardiac death in congenital and acquired long QT syndromes (LQTS) [1-5], heart failure [6], as well as ischemia [7]. Over the last two decades, genetic sequencing and molecular studies have revealed a diverse taxonomy of congenital LQTS subtypes, classified by both the specific genetic mutations and the ion channels they affect. Since the discovery of LQT1, 16 distinct subtypes of LQTS have been classified [8], with the major subtypes being LQT1, LQT2, and LQT3. In addition, many drugs have been identified to prolong QT interval resulting in acquired LQTS [9].

While the molecular causes of LQTS are complex, clinical studies have shown that polymorphic ventricular tachyarrhythmias (PVT) or *Torsade de Pointes* in LQTS patients are usually preceded by several characteristic electrocardiogram (ECG) features (Fig.5-1):

> *Pause-dependent and non-pause-dependent initiation of PVT*—The onset of PVT in LQTS patients are mainly (~70%) pause-dependent [10, 11], i.e., PVT occurs after a prolonged RR interval. A ubiquitous ECG pattern preceding PVT is the so-called short-long-short (SLS) sequence (center top in Fig.5-1) [4, 9]. A smaller portion (~30%) are non-pause dependent [10, 11], i.e., PVT occurs spontaneously without a preceding pause or SLS sequence (center middle in Fig.5-1). Tan et al [12] showed that the onset of PVT is mainly pause-dependent in LQT2 and LQT3, but non-pause dependent in LQT1.
>
> *T-wave alternans (TWA)*—Macro-volt TWA occurs frequently in LQTS [4, 13-15]. TWA can either directly precede PVT without a pause (center bottom in Fig.5-1), or occur much earlier with the onset of PVT preceded by a pause or SLS sequence [4, 15].

R-on-T—In all modes of PVT initiation above, the PVCs or first beat of PVT (marked by "*" in Fig.5-1) occur on the down-slope of the T-wave, a well-known ECG phenomenon called R-on-T.

Reducing the many complex molecular causes to these several characteristic ECG features considerably simplifies our understanding of arrhythmogenesis in LQTS. However, how these molecular causes result in these characteristic ECG features, and how these features are then mechanistically linked to the initiation of PVT remain incompletely understood.

In this study, we seek to bridge the gaps between molecular cause, ECG features, and arrhythmia initiation using *in silico* models of human LQTS. The ECG patterns from our anatomical ventricle simulations well captured the clinical ECG patterns and their genotype specificities. From our anatomical ventricle and simplified tissue simulations of LQT1, LQT2, and LQT3, we obtained the following mechanistic insight: regional action potential duration (APD) prolongation (and thus QT prolongation) increases repolarization gradients, which when combined with enhanced $I_{Ca,L}$ causes the spontaneous genesis of PVCs. Since these PVCs emerge from the repolarization gradient that gives rise to the T-wave, we call this mechanism "*R-from-T*", in contrast with the classic explanation of R-on-T mechanism in which an exogenous PVC coincidentally encounters a vulnerable repolarizing region during the T-wave, which we call *"R-to-T".* In other words, in R-from-T, the PVC and the T-wave are not coincidental but causally related. We further distinguish these two mechanisms in detail in the

Discussion section. Since enhanced $I_{Ca,L}$ is required for the R-from-T mechanism, targeting the properties of $I_{Ca,L}$ could prevent PVT regardless of the specific subtype of LQTS.

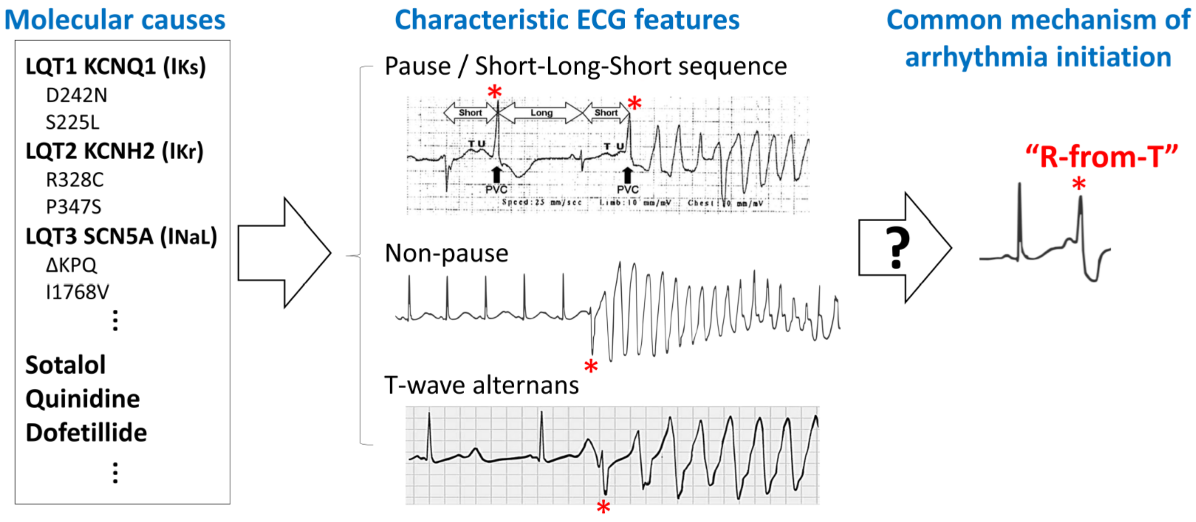

Figure 5-1. Schematic diagram linking the different molecular causes of LQTS to characteristic ECG features, and a hypothetical common mechanism of spontaneous arrhythmia initiation.

Left column: Genetic and non-genetic causes of LQTS at the molecular scale. **Middle column**: Characteristics ECG features of spontaneous arrhythmogenesis in LQTS patients. *Top ECG—Pause-dependent initiation of PVT*. An ECG from a patient with acquired LQTS showing SLS sequence preceding PVT, in which a first PVC (*) occurring on the downslope of the T-U wave causes a compensatory pause, resulting in a second PVC (*) leading to PVT. Modified from Fig.1 in Drew et al [4]. *Middle ECG—Non-pause-dependent initiation of PVT*. A representative ECG from a LQT1 patient with ischemia showing PVT initiation without a preceding pause. Modified from Fig.8B in Morita et al [3]. *Bottom ECG—TWA-dependent initiation of PVT*. An ECG recording from a young boy with congenital LQTS. The two sinus beats show prolonged QT intervals (>600 ms) and TWA. A PVC (*) then occurred on the downslope of the larger T-wave, which then immediately initiated ventricular tachycardia. Modified from Fig.37-33 B from *Braunwald's Heart Disease*, by Mann et al [16]. **Right column**: A hypothetical common mechanism of arrhythmia initiation in LQTS investigated in the current study, termed "R-from-T".

Methods

Computer models.

The human anatomical ventricle model was adapted from one previously developed by Ten Tusscher et al [17, 18]. We added a Purkinje network to the ventricle model generated using a method developed by Sahli Costabal et al [19]. 1D cable and 2D tissue models were used for mechanistic investigations. All computer simulations were performed on Tesla and GeForce GPUs (NVIDIA corporation) with software written in the CUDA programing language. Pseudo-ECGs were computed [20, 21] with the V5 lead shown unless otherwise specified.

The human ventricular action potential model by O'Hara et al [22] was used for the ventricular myocytes. The $I_{Ca,L}$ steady-state activation and inactivation curves were taken from either O'Hara et al [22] or Li et al [23]. The human Purkinje action potential model by Stewart et al [24] was used for the Purkinje network cells. We modeled LQT1 by removing I_{Ks}, LQT2 by removing I_{Kr}, and LQT3 by increasing I_{NaL} in the ventricles. Parameters are detailed in *Online SI* for each type of LQTS. A bulk heterogeneity in the right ventricle was created by adjusting a non-mutated current for each LQTS subtype, resulting in an APD map agreeing with the ECG-imaging studies of LQTS patients from Vijayakumar et al [25].

Further details of the mathematical models, the fiber structure in the ventricles, the Purkinje network, Purkinje cell-myocyte coupling, and ECG computation are presented in *Online SI*.

Arrhythmia initiation protocols. We used three protocols to elicit spontaneous initiation of arrhythmias:

1) *P_{Ca} ramp protocol:* Constant heart rate with a 20-sec $I_{Ca,L}$ conductance (P_{Ca}) ramp (1st panel Fig.5-2A). The ramp begins at the control value ($P_{Ca,control}$=0.0001 cm/s=1 µm/s) to a specified high value ($P_{Ca,H}$). The heart rate is fixed. This protocol simulates the initial phase of a β-adrenergic surge, when $I_{Ca,L}$ is quickly activated but I_{Ks} is not yet [26].

2) *Pause protocol (LQT2 and LQT3):* Constant P_{Ca} with a pause in the heart rate by a sudden change from 120 bpm to 60 bpm.

3) *Increasing heart rate protocol (LQT1):* Constant P_{Ca} with the RR interval gradually decreasing from 1000 ms (60 bpm) to 500 ms (120 bpm) in increments of 10 ms per beat.

Results

Initiation of arrhythmias in LQT2

Simulation of the anatomical ventricle model

We first used the P_{Ca} ramp protocol (Figs.2 A and B) to elicit spontaneous initiation of PVT. Fig.5-2A shows ECGs in the time interval from 10 s to 50 s for different $P_{Ca,H}$ values and Fig.5-2B shows voltage snapshots for $P_{Ca,H}$=2.8 µm/s. Fig.5-2C shows the ECGs for the pause protocol in which P_{Ca} was held at 2.8 µm/s for the whole simulation period. The ECG dynamics from these simulations are summarized as follows:

TWA and PVCs—Up to $P_{Ca,H}$=1.5 µm/s, the ECG remained in normal sinus rhythm (1st ECG). When $P_{Ca,H}$ was increased to 1.7 µm/s, TWA appeared (marked as "ABAB" on the 2nd ECG). When $P_{Ca,H}$ was increased to 1.8 µm/s, PVCs occurred (marked by "*", 3rd ECG). These PVCs were always superimposed on the T-wave, manifesting as R-on-T. TWA still preceded the appearance of PVCs (marked as "ABA" on the 3rd ECG panel), with the first PVC occurring on the larger of the alternating T-waves.

SLS sequence—At $P_{Ca,H}$=1.8 µm/s, the first PVC blocks next sinus beat, resulting in a compensatory pause. After this pause and the next sinus beat, a second PVC occurs resulting in a classic *SLS* sequence. This ECG pattern repeated as P_{Ca} was held at 1.8 µm/s. When $P_{Ca,H}$ was increased to 2.0 µm/s (4th ECG), after the first compensatory pause, an alternating interpolated PVCs pattern (occurring every other sinus beat) without compensatory pauses formed, a behavior we call PVC alternans.

PVT preceding SLS sequence—When $P_{Ca,H}$ was raised to above 2.5 µm/s, multiple episodes of non-sustained PVT (5th ECG) and sustained PVT (6th ECG) occurred. These episodes of PVT were always preceded by a SLS sequence. To reveal how PVCs and PVT occur spontaneously in the heart, we show selected snapshots in a 3-view sequence (Purkinje network voltage, ventricular myocardium voltage, and ventricular excitation wavefronts) for the initiation episode in the $P_{Ca,H}$=2.8 µm/s case (Fig.5-2B). Focal excitations repeatedly originate from the right ventricle heterogeneity and eventually evolve into a focal-reentrant mixture (see *Online Movie 5-1* for the entire episode).

PVT preceding a pause—We were also able to initiate arrhythmias using the pause protocol. Fig.5-2C shows an ECG for P_{Ca} held at 2.8 μm/s, in which the heart rate was suddenly decreased from 120 bpm to 60 bpm. When the heart rate was 120 bpm, no TWA or PVCs occurred. After the heart rate was changed to 60 bpm, PVT was initiated immediately.

Mechanistic insights of arrhythmogenesis from 1D and 2D tissue simulations

To better understand the underlying mechanism of arrhythmia initiation in the anatomical ventricle, we carried out additional simulations using 1D cable and 2D tissue models.

In the 1D cable, a region of longer APD was placed in the center by using a smaller I_{Ks} conductance (G_{Ks}), paced from the upper end. When P_{Ca} = 1 μm/s (Fig.5-3A), the APD was stable in the entire pacing cycle length (PCL) range from 400 ms to 1600 ms. For P_{Ca} = 2.0 μm/s (Fig.5-3B), when PCL was increased to 1000 ms, APD alternans occurred in the center region of the cable but did not generate PVCs (corresponding to TWA in the 2nd ECG in Fig.5-2A). At PCLs longer than 1150 ms, APD dynamics became more complex and PVCs occurred. For P_{Ca} = 2.3 μm/s (Fig.5-3C), when PCL was increased to a value where APD alternans occurred, PVCs also occurred. These APD alternans lead to PVC alternans (corresponding to the PVC pattern seen in the 4th ECG in Fig.5-2A). At slower PCLs, PVCs occur on every beat. Importantly, these PVCs emerge spontaneously from the repolarization gradient region and propagate only in one direction, a process we call *spontaneous unidirectional propagation*.

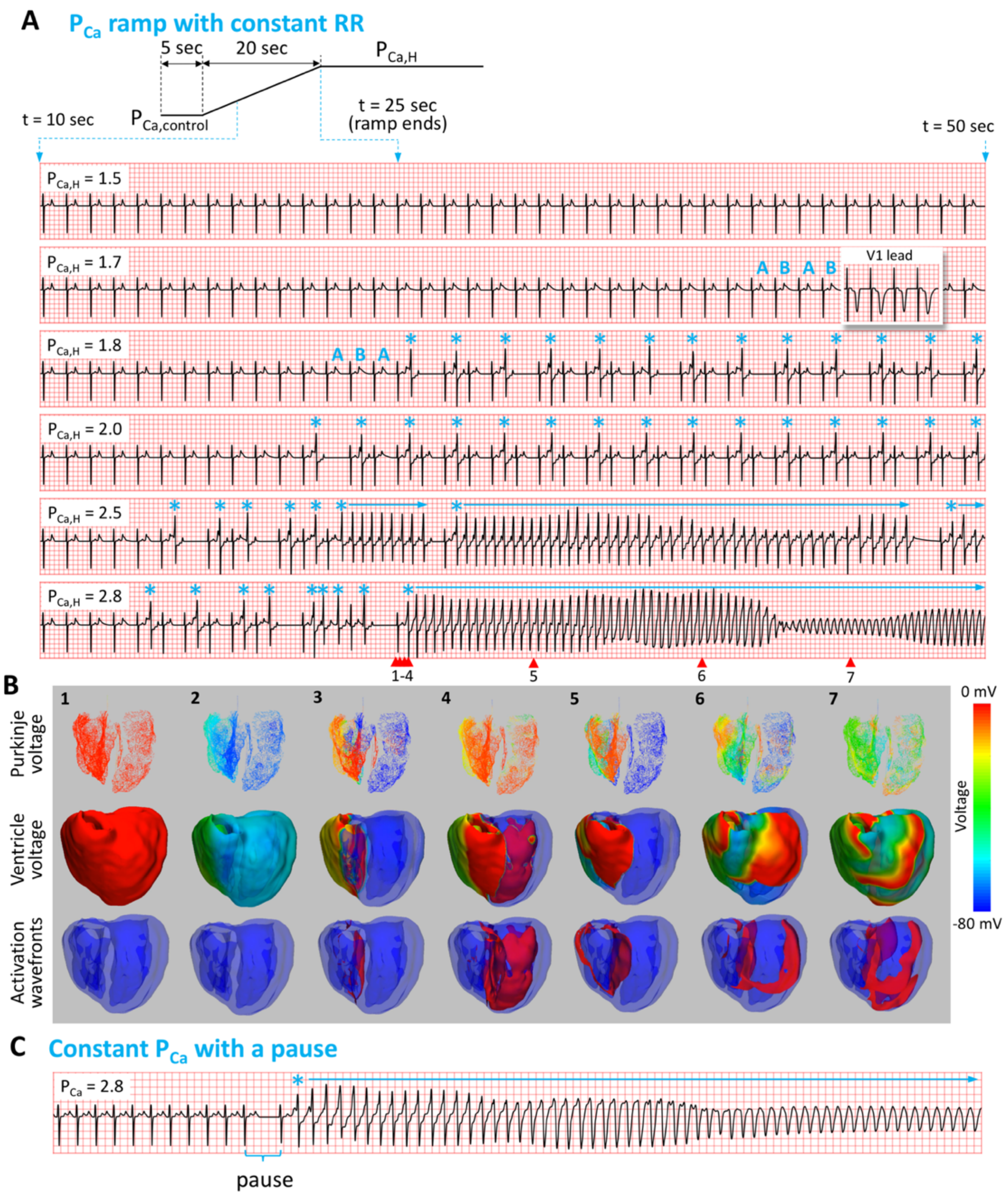

Figure 5-2. Spontaneous initiation of arrhythmias in LQT2.

A. Top panel: Schematic of the P_{Ca} ramp protocol. The ramp starts at t=5 s and ends at t=25 s. ECG traces: ECG traces from t=10 s to 50 s for 6 $P_{Ca,H}$ values (in units of µm/s) as indicated on each ECG. Heart rate was 60 bpm. "ABAB" marks TWA. "*" marks the PVCs and horizontal arrows indicate episodes of PVT. In the 2nd ECG we also show the V1 lead (inset) for TWA. **B**. Numbered snapshots of voltage maps (1st and 2nd row) and wavefronts (colored red, 3rd row) from the time points marked by corresponding red arrows on the last ECG in A ($P_{Ca,H}$=2.8 µm/s). See *Online Movie 5-1* for full episode. **C**. PVT induced by the pause protocol, changing the heart rate from 120 bpm to 60 bpm with a constant P_{Ca} =2.8 µm/s.

In the 2D tissue, a longer APD region is similarly placed in the center of the tissue (Figs.3 D and E). The tissue was paced from the left edge and the PCL was maintained at 700 ms for 20 beats and then suddenly increased to 1000 ms. In the first case, the long APD region is circular (Fig.5-3D, *Online Movie 5-2*). At PCL = 700 ms, no PVCs occurred. After PCL was increased to 1000 ms, focal excitations began to emerge from the APD gradient region. The excitations propagated unidirectionally (indicated by the white arrows), first to the right, then around the longer APD region before finally colliding and annihilating at the left side, forming a target-like pattern. This repeated to generate a focal train of multiple PVCs. As the PCL was maintained at 1000 ms, multiple such episodes occurred. However, when we changed the shape of the longer APD region into a larger and more elongated geometry (Fig.5-3E, *Online Movie 5-3*), the initial focal excitation directly evolved into sustained reentry instead, forming a figure-of-eight reentry since the region was large enough that the tips did not collide and annihilate. This reentry arose directly from spontaneous unidirectional propagation of the PVC itself, and was not the result of another exogeneous PVC encountering conduction block.

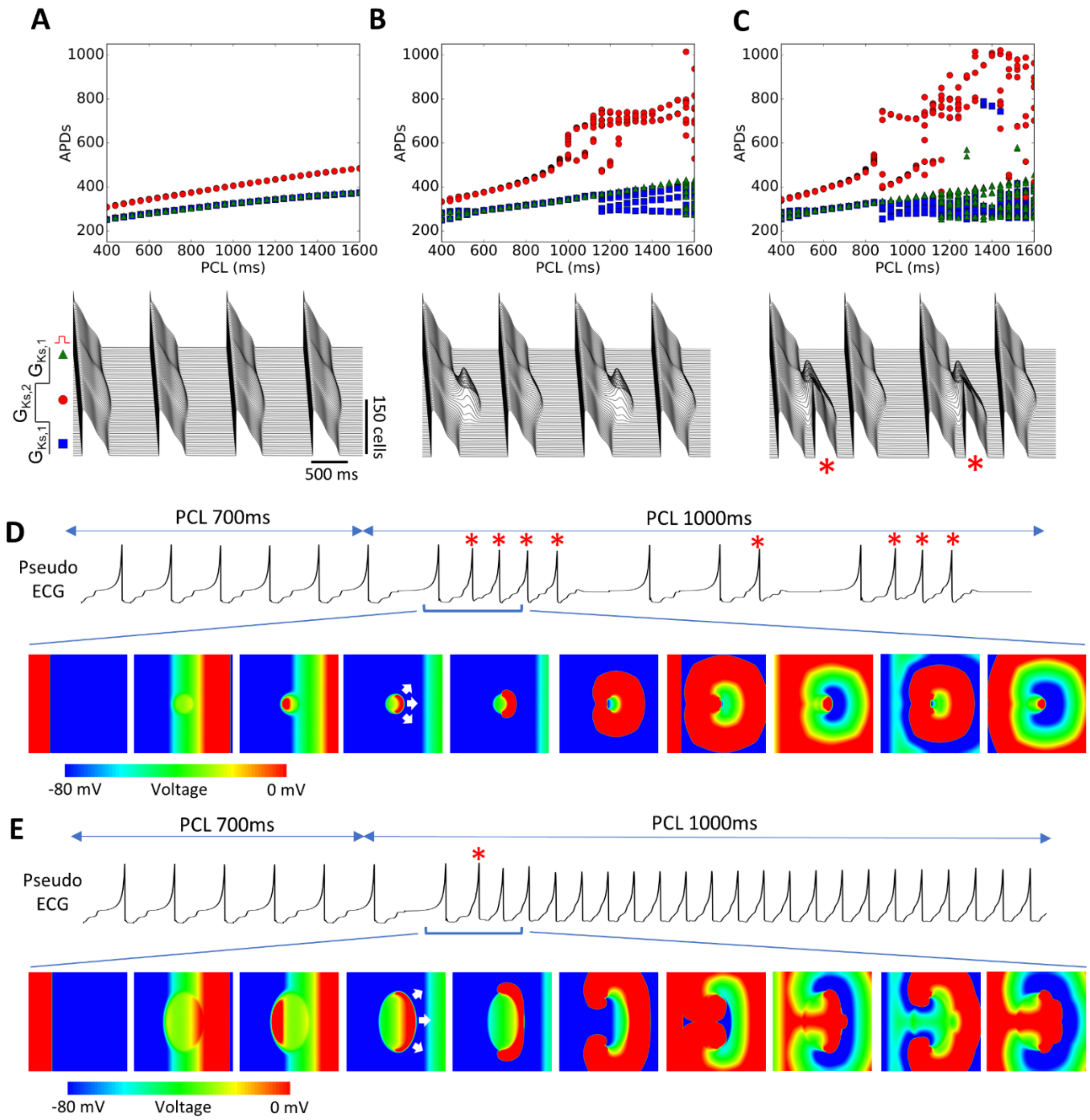

Figure 5-3. Mechanistic insights of arrhythmogenesis from 1D cable and 2D tissue simulations.

A. Upper: APD versus PCL recorded from the three locations indicated in the lower panel. Lower: Space-time plot of voltage in the 1D cable (300 cells) for 4 beats at PCL=1000 ms. P_{Ca}=1.0 μm/s. $G_{Ks,1}$=0.05 mS/μF, $G_{Ks,2}$=0.03 mS/μF. **B**. Same as A but for P_{Ca}=2.0 μm/s. APD alternans without PVCs occurred from PCL=1000 ms to 1150 ms. **C**. Same as A but for P_{Ca}=2.3 μm/s. APD alternans occurred from PCL=900 ms to 1050 ms, in which PVC alternans (marked with "*" in lower panel) occurred simultaneously. **D**. Pseudo-ECG and voltage snapshots from a 2D tissue (500x500 cells) simulation with a circular region of lower G_{Ks}. G_{Ks}=0.03 mS/μF in the center circular region (diameter = 100 cells), G_{Ks}=0.05 mS/μF elsewhere. The tissue was paced from the left side with 20 beats at PCL=700 ms and then changed to 1000 ms. White arrows in the 4th voltage panel indicate the direction of spontaneous unidirectional propagation of the PVC. See *Online Movie 5-2* for full episode. **E**. Same as D but the long APD region was changed to an oval (long axis = 300 cells, short axis = 200 cells). See *Online Movie 5-3* for full episode.

Initiation of arrhythmias in LQT3

We used the same two protocols as in LQT2 to elicit arrhythmias. Fig.5-4A shows the ECGs for the P_{Ca} ramp protocol. Similar to in LQT2, TWA preceded R-on-T PVCs (marked by "*"), and the first PVC always occurred on the larger of the alternating T-wave. Most of the time, episodes of PVT followed SLS sequences (i.e., a pause), but in some cases PVT also occurred immediately following TWA without a pause (3rd ECG). This case of TWA immediately preceding PVT is similar to the clinical example shown in Fig.5-1. Sustained ventricular tachycardia occurred at $P_{Ca,H}$ = 3.2 µm/s (6th ECG). In Fig.5-4B, we show selected snapshots in a 3-view mode for the initiation episode in the $P_{Ca,H}$ = 3.2 µm/s case (see *Online Movie 5-4* for the entire episode). The PVCs again emerged spontaneously and propagated out unidirectionally from the repolarization gradient region. In this case, the focal excitation traveled around the longer APD region and was able to quickly evolve into a stable reentry, manifesting as a monomorphic ventricular tachycardia. Using other parameters, the resulting arrhythmia could be either monomorphic or polymorphic.

We also elicited arrhythmias using the pause protocol (Fig.5-4C). With a heart rate of 120 bpm, no PVCs or arrhythmias occurred even at $P_{Ca,H}$ = 3.6 µm/s, but arrhythmias occurred immediately after a sudden decrease in heart rate to 60 bpm.

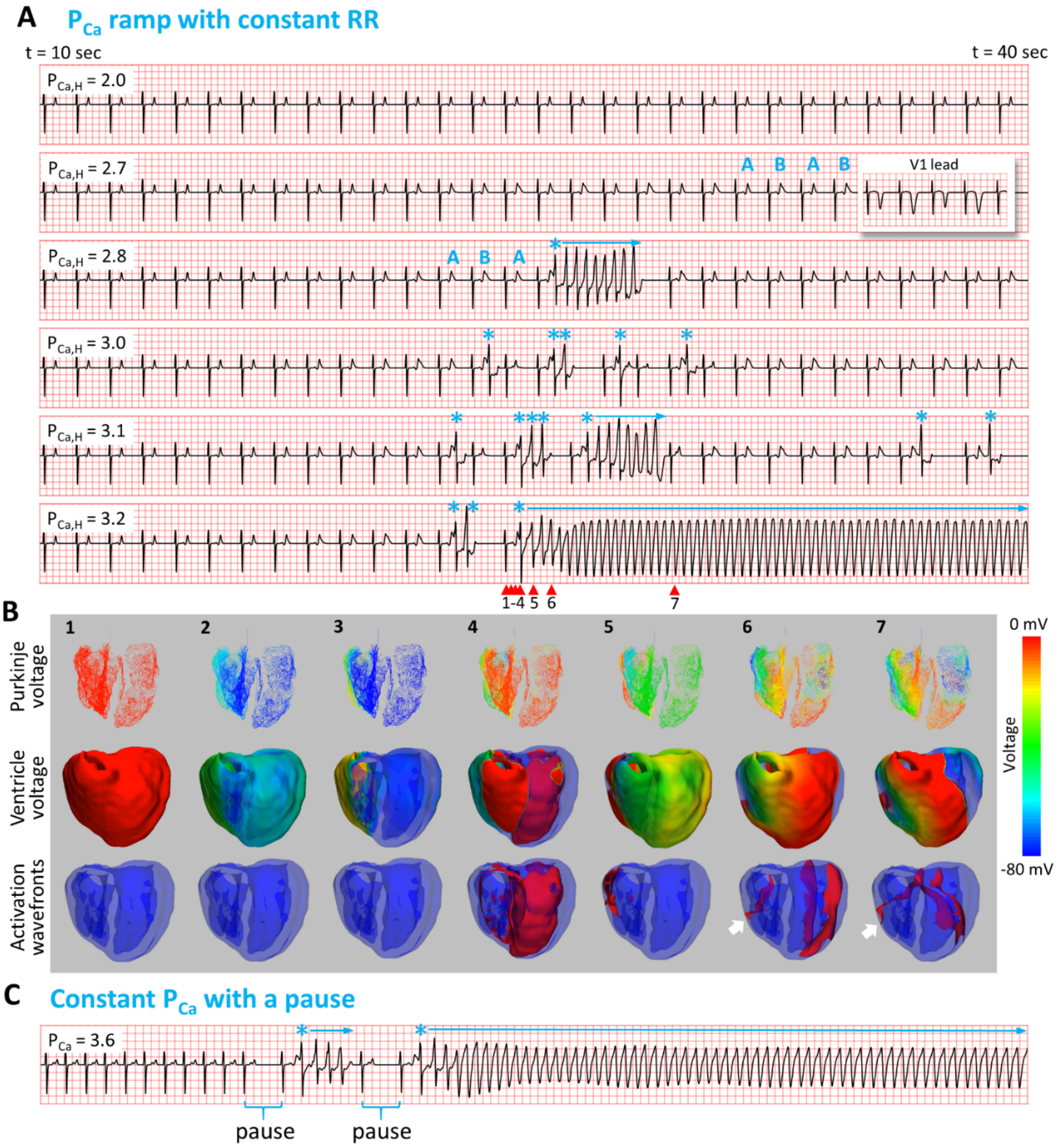

Figure 5-4. Spontaneous initiation of arrhythmias in LQT3.

A. ECG traces from t=10 s to 50 s for 6 $P_{Ca,H}$ values as indicated on each ECG, using the same P_{Ca} ramp protocol in LQT2 (top panel in Fig. 5-2A). Heart rate was 60 bpm. "ABAB" marks TWA. "*" marks the PVCs and horizontal arrows indicate episodes of PVT. In the 2nd ECG we also show the V1 lead (inset) for TWA. **B**. Numbered snapshots of voltage maps (1st and 2nd row) and wavefronts (colored red, 3rd row) from the time points marked by corresponding red arrows on the last ECG in A ($P_{Ca,H}$=3.2 μm/s). See *Online Movie 5-4* for full episode. **C**. PVT induced by the pause protocol, changing the heart rate from 120 bpm to 60 bpm with a constant P_{Ca} =3.6 μm/s.

Initiation of arrhythmias in LQT1

Spontaneous initiation of PVT in LQT1 manifests differently than in LQT2 and LQT3. We first used the P_{Ca} ramp protocol with heart rates of 60 bpm and 120 bpm. Fig.5-5A shows ECGs at three $P_{Ca,H}$ values for both heart rates. At $P_{Ca,H}$ = 2.1 μm/s, both ECGs show normal sinus rhythm. When $P_{Ca,H}$ was increased to 3.1 μm/s, arrhythmias occurred at 120 bpm but not at 60 bpm. When $P_{Ca,H}$ was increased further to 4.1 μm/s, arrhythmias occurred at both heart rates. Note that in either heart rate, arrhythmias always occurred without a preceding pause or SLS sequence. In addition, no TWA was observed at any $P_{Ca,H}$. Despite these differences from LQT2 and LQT3, the arrhythmias were still initiated with an R-on-T (marked by "*"). The 3-view snapshots also show focal excitations emerging from the repolarization gradient region, resulting in PVT (Fig.5-5B and *Online Movie 5-5*). PVT was also able to be elicited using the increasing heart rate protocol for certain $P_{Ca,H}$ values between 3.1 and 4.1 μm/s, with an example shown at $P_{Ca,H}$=4.0 μm/s (Fig.5-5C).

While the presence of I_{Ks} can explain why arrhythmias tend to occur at slower heart rates in LQT2 and LQT3 [27], it is not clear why a unique SLS sequence occurs in LQT2 and LQT3 but not in LQT1. To understand the underlying mechanism, we carried out single cell and 1D cable simulations comparing LQT1 and LQT2. Fig.5-6A shows APD versus P_{Ca} for LQT1 and LQT2. In the case of LQT1, increasing P_{Ca} causes APD to increase suddenly to repolarization failure. However, in the case of LQT2, APD increases as a staircase with incremental transitions. The sudden repolarization failure in LQT1 is due to the fact that peak I_{Kr} does not change with increasing APD since I_{Kr} has already saturated (upper panels in Fig.5-6B), and therefore there is not enough outward current to oppose the increase of $I_{Ca,L}$. On the other hand, when I_{Ks} is

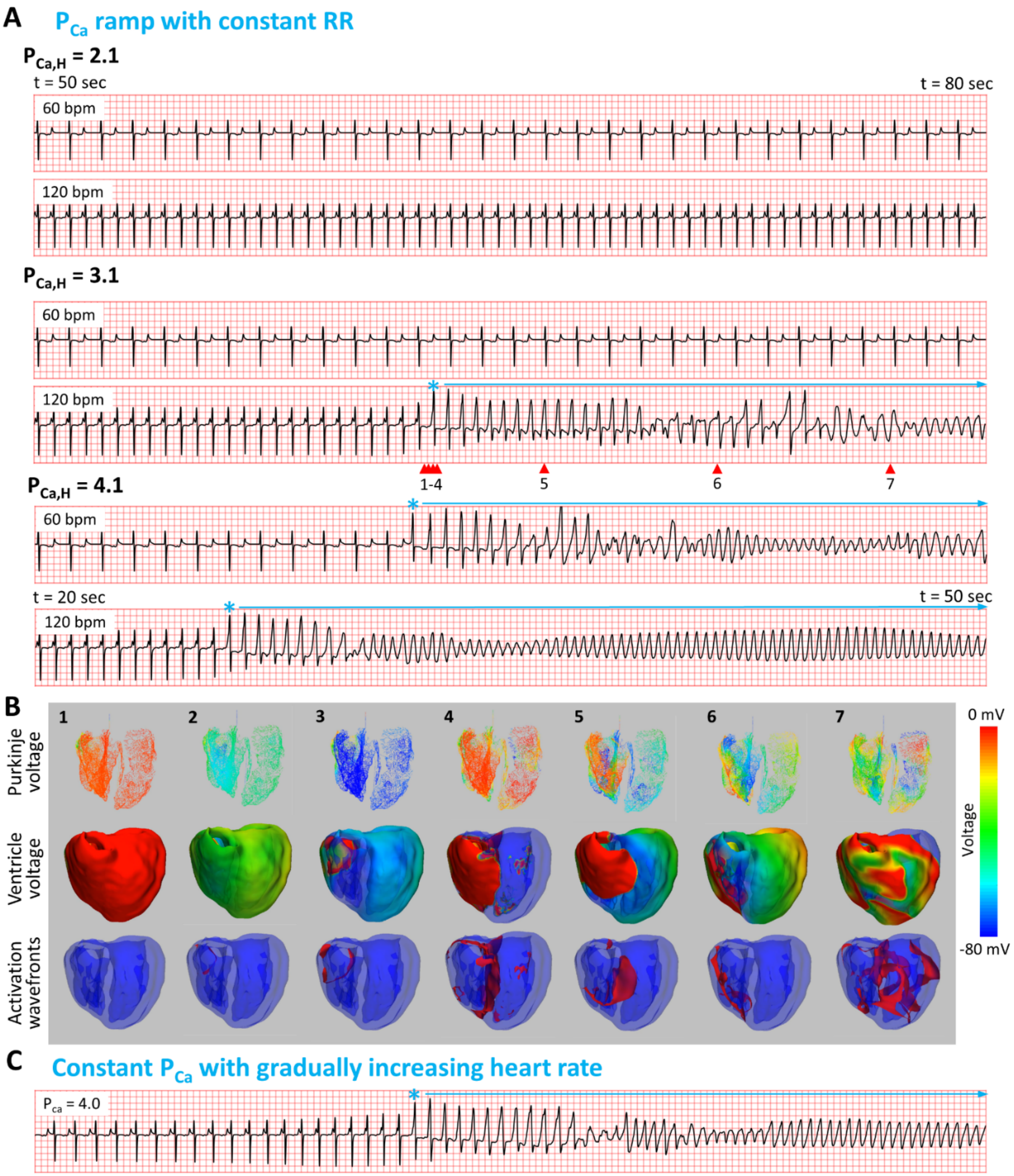

Figure 5-5. Spontaneous initiation of arrhythmias in LQT1.

A. ECG traces at 2 heart rates (60 bpm and 120 bpm) for 3 $P_{Ca,H}$ values, using the same P_{Ca} ramp protocol in LQT2 (top panel in Fig. 5-2A). "*" marks the PVCs and horizontal arrows indicate the PVT episodes. **B**. Numbered snapshots of voltage maps (1st and 2nd row) and wavefronts (colored red, 3rd row) from the time points marked by corresponding red arrows on the 4th ECG in A (120 bpm, $P_{Ca,H}$=3.1 µm/s). See *Online Movie 5-5* for full episode. **C**. PVT induced by the increasing heart rate protocol. Heart rate was gradually increased from 60 bpm to 120 bpm for a constant P_{Ca}=4.0 µm/s.

present as in LQT2, it does increase with increasing APD due to its slow activation (lower panels in Fig.5-6B), supplying enough outward current to oppose $I_{Ca,L}$ for repolarization. At the tissue scale, repolarization failure in the long APD region causes repetitive firings at both fast and slow heart rates (Fig.5-6C). Therefore, in LQT1, the sudden transition from a normal action potential to repolarization failure causes the transition from sinus rhythm to repetitive focal firings. Single PVCs with a compensatory pause or SLS sequences do not have a chance to develop, since full blown arrhythmias occur immediately from the first PVC onward.

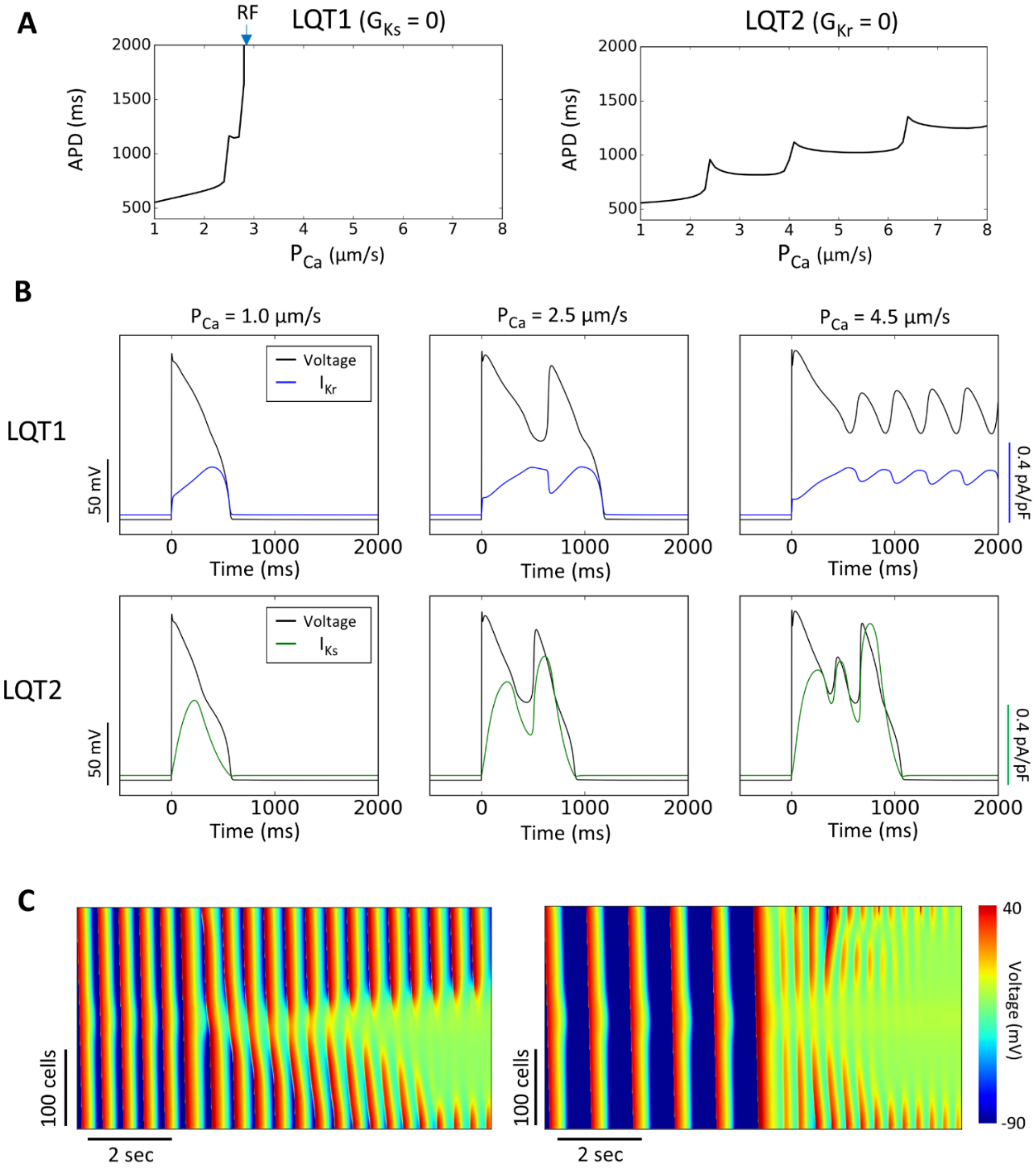

Figure 5-6. Cellular and tissue mechanisms of arrhythmogenesis in LQT1.

A. Single cell APD versus P_{Ca} for LQT1 (left) and LQT2 (right). Arrow marks P_{Ca} where repolarization failure occurs. **B**. Single cell voltage, I_{Kr}, and I_{Ks} versus time for LQT1 (upper panels) and LQT2 (lower panels) at three P_{Ca} values. **C**. Linescans of voltage in a 1D cable for P_{Ca} = 3.1 µm/s at PCL=500 ms (left, corresponding to the 4th ECG in Fig. 5-5A) and P_{Ca} = 4.1 µm/s at PCL=1000 ms (right, corresponding to the 5th ECG in Fig. 5-5A) in LQT1, showing repolarization failure in the center of the cable generating new PVCs.

Reducing window $I_{Ca,L}$ prevents arrhythmogenesis in LQTS

Although the modes of spontaneous arrhythmia initiation are genotype-dependent, one common requirement is the enhancement of $I_{Ca,L}$. Moreover, the R-on-T focal excitations that initiate the arrhythmias always originate from the repolarization gradient regions, resulting in focal, reentrant, or mixed focal-reentrant arrhythmias. Based on our understanding of the role window $I_{Ca,L}$ plays in both EAD-genesis in single cells [28, 29] and PVC formation in heterogeneous tissue [30], we hypothesized that reducing the window $I_{Ca,L}$ can prevent arrhythmias in LQTS. We reduced the window $I_{Ca,L}$ by shifting the steady-state inactivation curve (f_∞) as indicated in Fig.5-7A. The advantage of shifting f_∞ (in contrast to $I_{Ca,L}$ blockade) is that it does not affect $I_{Ca,L}$ in the normal action potential (Fig.5-7B left), but can effectively suppress EADs (Fig.5-7B right) and PVCs [30]. Left-shifting f_∞ by 5 mV prevented the arrhythmias that were induced by the P_{Ca} ramp protocol in LQT1, LQT2, and LQT3 (Fig.5-7C). To systematically evaluate the efficacy of this therapeutic strategy, we carried out 1D cable simulations to identify the P_{Ca} threshold for PVCs versus the amount of f_∞ shift (Fig.5-7D). In all three subtypes of LQTS, a 5 mV shift almost doubled the threshold for arrhythmias. At 8 mV shift, no PVCs were seen even at 6 times the control P_{Ca} for any LQTS subtype.

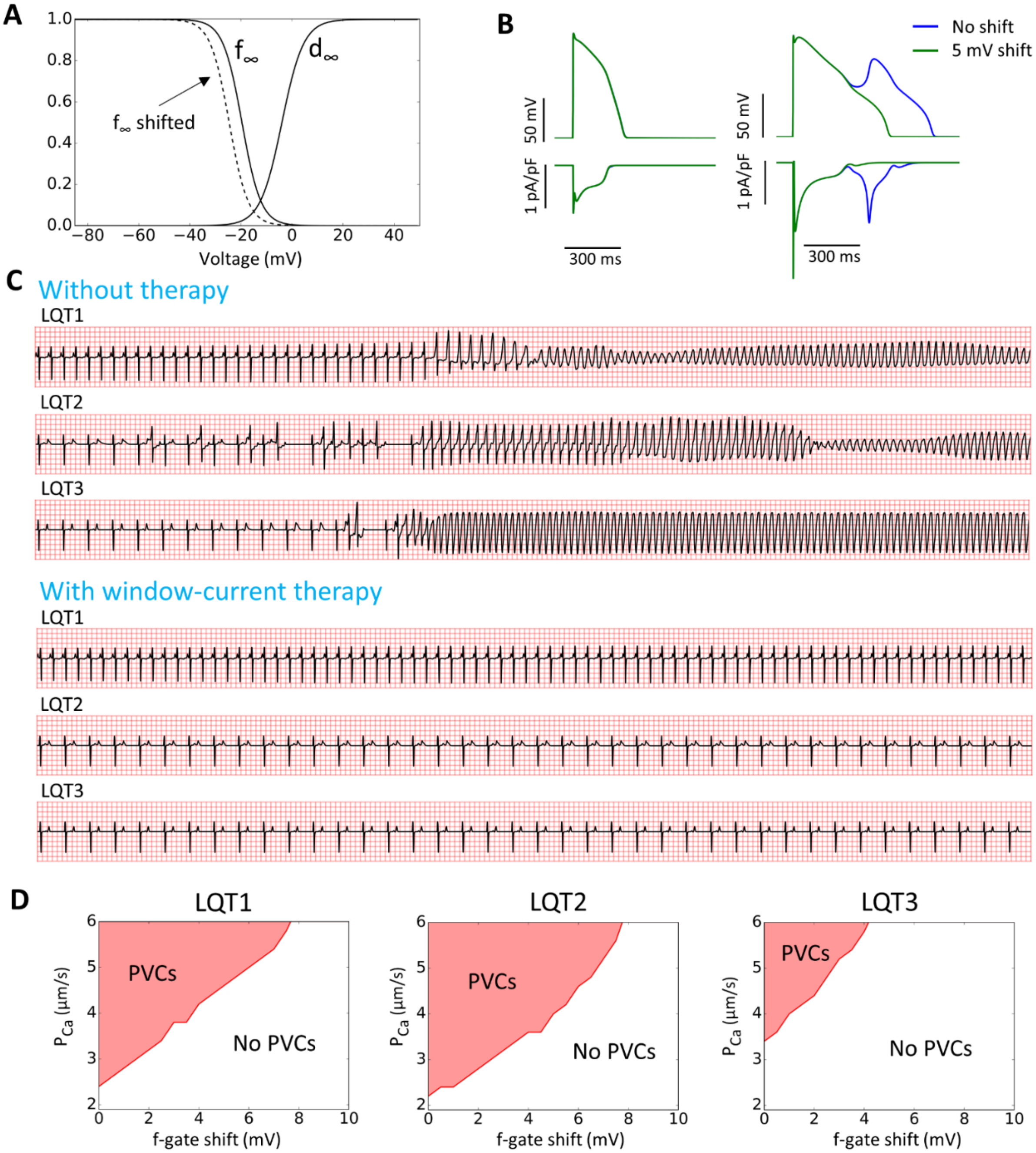

Figure 5-7. A unified genotype-independent therapy for LQT1, LQT2, and LQT3.

A. Steady-state activation (d_∞) and inactivation (f_∞) curves for $I_{Ca,L}$. Dashed curve is f_∞ with a 5 mV shift. **B**. Action potential and $I_{Ca,L}$ before and after 5 mV shift of f_∞. Left: Normal action potential in which the shift causes no change (the green and blue curves are superimposed). Right: The EAD was suppressed by the 5 mV shift, but with no change in peak $I_{Ca,L}$. **C**. ECG before (reproduced from Fig. 5-2, 5-4, 5-5) and after a 5 mV f_∞ shift in LQT1, LQT2, and LQT3. **D**. P_{Ca} threshold for PVCs in 1D cable simulations versus voltage shift of f_∞ for LQT1, LQT2, and LQT3.

Discussion

In this study, we used anatomical human ventricle and simplified tissue models to systematically investigate the mechanisms of spontaneous arrhythmia initiation in LQTS. Our simulations reproduced the characteristic ECG features commonly seen in LQTS patients, including TWA, R-on-T, and SLS sequences leading to PVT in LQT2 and LQT3, and non-pause-dependent initiation of PVT in LQT1. 1D and 2D models further explored the detailed mechanisms of TWA, PVC formation, and initiation of arrhythmias. We showed that although the characteristic ECG features preceding the onset of PVT may vary between the different LQTS genotypes, a common mechanism for PVT initiation may exist which we call "R-from-T". In this R-from-T mechanism, PVCs are generated from increased repolarization gradients (as a result of QT prolongation) with an enhanced $I_{Ca,L}$ (such as during a β-adrenergic surge), which then propagate unidirectionally away from the repolarization gradient region. This can generate either target-like excitation patterns resulting in focal arrhythmias or evolve into reentrant arrhythmias depending on the geometry of the tissue heterogeneity. This new understanding leads to a unified therapeutic strategy in which a single intervention of suppressing window $I_{Ca,L}$ effectively prevented arrhythmias in multiple LQTS subtypes. Detailed mechanistic insights and implications for clinical arrhythmia prevention are discussed in detail below.

R-from-T as a common mechanism of arrhythmia initiation in LQTS: R-on-T revisited

"*R-on-T*" is a descriptive term denoting the ECG appearance of an R-wave superimposed on a T-wave. R-waves that occur during the downslope of a T-wave have been widely associated with increased arrhythmia risk in a variety of conditions [31]. Here we discuss our current understanding of the different possible mechanisms by which arrhythmias can spontaneously initiate with the R-on-T phenomenon (Fig.5-8).

The classical mechanistic explanation for arrhythmias initiating as an R-on-T is as follows: When an ectopic PVC from somewhere either in the Purkinje network or ventricular myocardium encounters a refractory region with right timing, *unidirectional conduction block* can occur which may then develop into figure-of-eight reentry (Fig.5-8 left). Since in this scenario the PVC travels and encounters a repolarizing T-wave by chance, we call this classic mechanism the "*R-to-T*" mechanism.

In the current and our previous studies [18, 30, 32, 33], we have shown that PVCs can also spontaneously arise from a repolarization gradient via a dynamical instability when $I_{Ca,L}$ is significantly enhanced. The PVCs from this mechanism will always appear and coincide during the T-wave, also manifesting as R-on-T on ECG. Because these PVCs arise from the repolarization gradient and thus are causally linked with the T-wave, we call this new mechanism the "*R-from-T*" mechanism (Fig.5-8 middle and right). Note that in R-to-T, the R wave and T wave are two independent events, while in R-from-T, the R-wave is caused by the T-wave.

In R-from-T, after the PVCs emerge spontaneously from the repolarization gradient region, they propagate unidirectionally away from the gradient, a behavior we call *spontaneous unidirectional propagation*. Evidence of this type of PVC behavior has been shown in optical mapping experiments of rabbit and canine hearts [30, 34-36], where spontaneous PVCs would emerge from the steep repolarization gradient region and propagate unidirectionally. This behavior results in distinctly different mechanisms of arrhythmogenesis compared to the classical R-to-T mechanism. First, repeated PVCs can occur by R-from-T [30], manifesting as singlets, couplets, or a long train of PVCs, resulting in sustained or non-sustained focal arrhythmias. Second, since the PVC only propagates unidirectionally, it can also evolve directly into reentrant arrhythmias without requiring an additional region of heterogeneity to cause conduction block. Thus, depending on the properties of the heterogeneity, these PVCs can result in focal, reentrant, or mixed focal/reentrant arrhythmias all from the same R-from-T mechanism.

Since the R-from-T PVCs and the subsequent arrhythmias are caused by the same mechanism, a single PVC in this case can be considered as just the shortest possible run of an arrhythmia. Couplets, triplets, trains of PVCs, and the subsequent PVT are just longer runs of arrhythmias from the same underlying instability, which depends on the cellular and tissue properties as well as the interactions of PVCs with the sinus beats. In this sense, the R-from-T mechanism blurs the line between the usual notions of a distinct trigger and substrate in arrhythmia initiation.

While the R-to-T mechanism is widely considered as the prototypical mechanism of arrhythmogenesis in cardiac diseases in general [37, 38], it is unknown whether such a mechanism is indeed responsible for the spontaneous initiation of arrhythmias in LQTS. Although the R-to-T mechanism has been reproduced in computer simulations of LQTS using an externally-applied premature stimulus (so-called S1S2 protocol) [39], to our knowledge there is no clear experimental evidence of spontaneous arrhythmias caused by R-to-T in LQTS. On the other hand, several optical mapping experiments of LQTS do show spontaneous unidirectional propagation from the steep repolarization gradient region [30, 34-36], consistent with the R-from-T mechanism. Other recent simulation studies [18, 30, 32, 40, 41] have also shown spontaneous initiation of arrhythmias without an external stimulus, while our current study is able to reproduce the characteristic ECG features seen LQTS patients and reveals how R-from-T serves as a common mechanism of arrhythmia initiation in different LQTS subtypes.

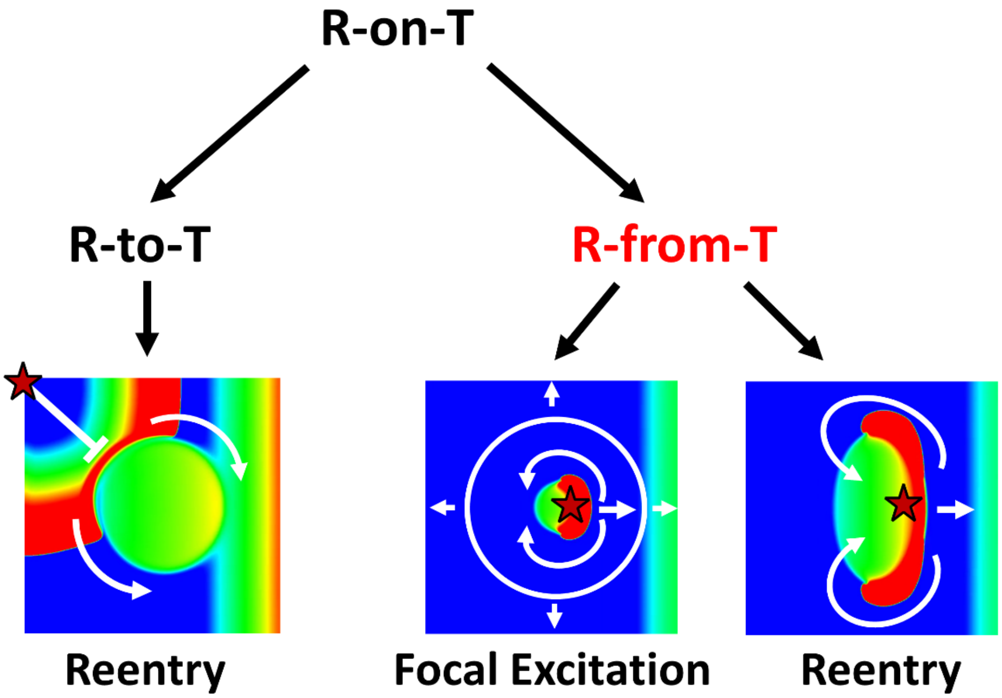

Figure 5-8. Schematic diagram distinguishing the “R-to-T” and “R-from-T” mechanisms of arrhythmia initiation.

Spontaneous arrhythmias that initiate with an R-on-T phenomenon on ECG can arise from two different underlying mechanisms which we call “R-to-T” and “R-from-T”. **Left:** R-to-T is the mechanism in which a PVC encounters a repolarizing region, undergoing *unidirectional conduction block* and causing figure-of-eight reentry. The R-wave and T-wave are two independent events, and the arrhythmias are only reentry. **Middle and Right:** R-from-T is the mechanism investigated in this study, where a PVC emerges from a repolarization gradient resulting in *spontaneous unidirectional propagation*. The R-wave is caused by the T-wave, and the arrhythmias can be either focal excitations (middle) or reentry (right) depending on the properties of the heterogeneity.

Mechanistic links between the characteristic ECG features and spontaneous PVT initiation in LQTS

TWA and SLS sequences are the major characteristic ECG features known to precede PVT in LQTS but their detailed relationship is not well understood. Our results from this study offer a deeper explanation through the R-from-T mechanism.

TWA has been widely observed in LQTS [4, 13-15], and often precedes the initiation of PVT, either immediately (e.g., center bottom in Fig.5-1) [16] or many hours before a pause-induced arrhythmia [4, 15]. In our $I_{Ca,L}$ ramp protocol simulations of LQT2 (Fig.5-2) and LQT3 (Fig.5-4), TWA was observed just before the appearance of PVCs and PVT. The first PVC during the $I_{Ca,L}$ ramp always occurred on the larger of the alternating T-waves. In most of the cases, PVT initiation was still preceded by a SLS sequence, but could also occur immediately following TWA without a SLS sequence (3rd ECG in Fig.5-4A). These simulated ECG behaviors agree well with the clinical ECG features seen in LQTS patients [4, 15, 16]. The role of TWA in the genesis of PVCs and arrhythmias has been investigated in our recent study [32]. We demonstrated that TWA can further exacerbate the repolarization gradient causing PVCs and PVT. However, TWA itself is an intermediate behavior, also caused by enhanced $I_{Ca,L}$ (Figs. 2-4) and slow heart rates (Fig.5-3), or simply by QT prolongation [32]. PVCs and initiation of PVT also result from enhanced $I_{Ca,L}$ and slow heart rates, but do not necessarily require TWA to occur. The $I_{Ca,L}$ threshold or the heart rate threshold for TWA is lower than that for PVCs and arrhythmias, which may explain why TWA occurs frequently in LQTS without arrhythmias or can occur long before arrhythmia onset. These insights agree well with the clinical observation that LQTS patients with TWA have a higher incidence of arrhythmias, but QT prolongation is still the primary risk factor [14].

The SLS sequence or a pause immediately preceding PVT initiation is a unique ECG feature in LQTS, accounting for the majority of PVT initiation patterns [4, 9-12, 42]. In our anatomical ventricle simulations, almost all PVT episodes were preceded by a SLS sequence in LQT2 and LQT3, but not in LQT1, agreeing with clinical observations [12]. In our $I_{Ca,L}$ ramp protocol simulations, the SLS sequence appeared naturally as $I_{Ca,L}$ was ramped up. When the first PVC occurs (short), it propagates retrogradely through the Purkinje network, blocking the next sinus beat and resulting in a longer RR interval (long). This increased RR interval further exacerbates the repolarization gradient, leading to another PVC on the next beat (short). Since this pause is longer than the normal sinus RR interval, the repolarization gradient becomes more severe, which can lead to repetitive PVCs or reentrant PVT. The role of the first PVC, whether it arises from R-from-T or any additional mechanisms including DADs, Purkinje automaticity, or even heart rate variability (for example in Fig.5-2C, Fig.5-4C), is to simply set up the long compensatory pause.

Note that our anatomical ventricle simulations capture the wide range of ECG phenomenon in LQTS, including TWA, PVCs, SLS, R-on-T, and PVTs with only a single intervention, i.e., ramping up $I_{Ca,L}$. This suggests that the R-from-T mechanism is a likely candidate for spontaneous arrhythmogenesis in LQTS.

Genotype-dependent onset of PVT: Role of I_{Ks}

Different LQTS subtypes are known to exhibit different genotype-dependent triggers [43] and characteristic ECG features preceding PVT [12]. For example, LQT2 and LQT3 arrhythmias tend to be more bradycardia-dependent, while in LQT1 this rate-dependence is much less sensitive and can even be tachycardia-dependent, a feature well captured by our simulations. This can be explained by the well-known effect of the slow transition to the deeper closed-states of I_{Ks} [27]: a longer diastolic interval will cause fewer channels to be available for immediate opening in the next action potential, and thus results in a lower repolarization reserve. However, it is not clearly understood why SLS sequences occur frequently in LQT2 and LQT3, but not in LQT1. This study offers further mechanistic insight.

The effects of slow activation of I_{Ks} on APD have been investigated in general in our previous study [44] and in a recent study by Varshneya et al [45]. As shown in our single cell and 1D cable results (Fig.5-6), in the absence of I_{Ks}, the action potential tends to exhibit an all-or-none response to increasing $I_{Ca,L}$, i.e., the action potential either repolarizes normally or fails to repolarize. But in the presence of I_{Ks}, the APD exhibits a more graded response to increasing $I_{Ca,L}$ due to the slow activation of I_{Ks}. Therefore, in LQT1 repolarization failure will occur abruptly in the longer APD region once $I_{Ca,L}$ reaches the threshold, directly generating repetitive focal PVCs and causing a sudden transition from sinus rhythm to PVT. In LQT2 and LQT3 however, the APD increases gradually in response to the $I_{Ca,L}$ ramp. When $I_{Ca,L}$ reaches the threshold, only a single PVC is generated, which can result in a compensatory pause and potentiates R-from-T arrhythmogenesis in a pause-dependent manner with a SLS sequence.

Although these genotype-dependent features leading up to PVT appear very different, the mechanism of arrhythmia initiation is still the same, i.e. R-from-T. Therefore, this study provides important insights that mechanistically link the molecular causes of LQTS to the characteristic ECG features, and then these ECG features to a common R-from-T mechanism for spontaneous PVT initiation.

Implications for developing a unified therapy for PVT prevention in LQTS

A major insight from our study is that the R-from-T mechanism may be the final common pathway leading to PVT initiation, regardless of the LQTS genotype. One critical factor for R-from-T was an enhanced $I_{Ca,L}$. It is well-known that blocking Ca^{2+} channels has adverse effects of weakening contraction [46], and thus Ca^{2+} channel blockers are typically not appropriate for clinical use. In this study, we showed that R-from-T arrhythmogenesis does not occur until $I_{Ca,L}$ is significantly increased above baseline (a two to four-fold increase). Therefore, instead of blocking $I_{Ca,L}$ overall, preventing excessive increase of $I_{Ca,L}$ over baseline can still be effective in preventing R-from-T arrhythmias. This observation agrees with current clinical practice where β-blockers are used as the mainstay arrhythmia prevention therapy in LQTS [43], since β-blockers can prevent the excessive $I_{Ca,L}$ increase during a sympathetic event, albeit still with notable side effects on heart rate, exercise tolerance, and blood pressure.

In this study, we demonstrated another potential therapy, treating different LQTS subtypes using only a single intervention by reducing the $I_{Ca,L}$ window current with a simple shift in the steady-state inactivation curve (f_∞). In other words, we were able to prevent arrhythmias in LQT1, LQT2, and LQT3, only by targeting the $I_{Ca,L}$ window current. The advantages of this therapeutic strategy include: 1) it avoids affecting the normal calcium transient required for contractility as calcium channel blockers would; 2) it does not affect the APD (and thus QT interval) during sinus rhythm, differing from many of the ion channel blockers; and 3) it avoids affecting the heart rate as with β-blockers. Our results demonstrate that this approach was effective, as only a small 5mV shift in f_∞ doubled the arrhythmia threshold for all LQTS subtypes.

Limitations

For the sake of mechanistic clarity and data availability, some aspects of our models were simplified in as reasonable a manner as possible. The anatomical ventricle model tissue heterogeneity was simulated as a simplified single bulk region to elicit a clearly interpretable initiation of arrythmias, which may result in T-wave morphologies that differ from real patients [47]. More complicated heterogeneities may result in more mixed cases with different or multiple initiation sites. In addition, inter-patient ionic current variability can play important roles in the mode of arrhythmia initiation, which may require population modeling approaches [48-50]. We also simulated the β-adrenergic surge by only ramping up $I_{Ca,L}$ without any other effects, focusing on the initial phase of sympathetic simulation. In this study the most extreme congenital LQT1 and LQT2 mutations of zero I_{Ks} and I_{Kr} were simulated, but there are many other possible mutations with partial reduction or trafficking defects instead of complete deficiency, which may result in further mixed or intermediate behaviors. Finally, this study focused on congenital LQT1, LQT2, and LQT3, but the insights into PVT initiation and prevention by targeting $I_{Ca,L}$ could also be applicable to other congenital LQTS and acquired LQTS since the R-from-T mechanism seems invariant to the particular cause of QT prolongation, as long as a repolarization gradient and sufficiently elevated $I_{Ca,L}$ exists. This needs to be verified in other types of congenital LQTS as well as acquired LQTS in future modeling studies, and eventually verified in future experimental and clinical studies.

Conclusions

Despite the complex genetic and non-genetic causes of LQTS and genotype-dependent clinical features, R-from-T offers a promising common mechanism for PVT initiation in LQTS. Since R-from-T arrhythmogenesis is promoted by a steep repolarization gradient and requires an enhanced $I_{Ca,L}$ to occur, targeting $I_{Ca,L}$ properties, such as suppressing window $I_{Ca,L}$ or preventing excessive increase of $I_{Ca,L}$, can be an effective unified therapy for arrhythmia prevention in LQTS.

References

1. Napolitano, C., et al., *Sudden Cardiac Death and Genetic Ion Channelopathies.* Circulation, 2012. **125**(16): p. 2027-2034.
2. Roden , D.M., *Long-QT Syndrome.* New England Journal of Medicine, 2008. **358**(2): p. 169-176.
3. Morita, H., J. Wu, and D.P. Zipes, *The QT syndromes: long and short.* The Lancet, 2008. **372**(9640): p. 750-763.
4. Drew, B.J., et al., *Prevention of torsade de pointes in hospital settings: a scientific statement from the American Heart Association and the American College of Cardiology Foundation.* Circulation, 2010. **121**(8): p. 1047-60.
5. Bezzina, C.R., N. Lahrouchi, and S.G. Priori, *Genetics of Sudden Cardiac Death.* Circulation Research, 2015. **116**(12): p. 1919-1936.
6. Tomaselli, G.F. and D.P. Zipes, *What causes sudden death in heart failure?* Circ Res, 2004. **95**(8): p. 754-63.
7. Halkin, A., et al., *Pause-dependent torsade de pointes following acute myocardial infarction: a variant of the acquired long QT syndrome.* J Am Coll Cardiol, 2001. **38**(4): p. 1168-74.
8. Giudicessi, J.R., A.A.M. Wilde, and M.J. Ackerman, *The genetic architecture of long QT syndrome: A critical reappraisal.* Trends in Cardiovascular Medicine, 2018. **28**(7): p. 453-464.
9. Roden, D.M., *Drug-induced prolongation of the QT interval.* N Engl J Med, 2004. **350**(10): p. 1013-22.
10. Viskin, S., et al., *Arrhythmias in the congenital long QT syndrome: how often is torsade de pointes pause dependent?* Heart, 2000. **83**(6): p. 661-6.
11. Noda, T., et al., *Classification and mechanism of Torsade de Pointes initiation in patients with congenital long QT syndrome.* Eur Heart J, 2004. **25**(23): p. 2149-54.
12. Tan, H.L., et al., *Genotype-Specific Onset of Arrhythmias in Congenital Long-QT Syndrome: Possible Therapy Implications.* Circulation, 2006. **114**(20): p. 2096-2103.
13. Narayan, S.M., *T-wave alternans and the susceptibility to ventricular arrhythmias.* J Am Coll Cardiol, 2006. **47**(2): p. 269-81.
14. Zareba, W., et al., *T wave alternans in idiopathic long QT syndrome.* Journal of the American College of Cardiology, 1994. **23**(7): p. 1541-1546.
15. Wegener, F.T., J.R. Ehrlich, and S.H. Hohnloser, *Amiodarone-associated macroscopic T-wave alternans and torsade de pointes unmasking the inherited long QT syndrome.* Europace, 2008. **10**(1): p. 112-3.

16. Mann, D.L., et al., *Braunwald's Heart Disease: A Textbook of Cardiovascular Medicine*. 10th ed. 2015, Philadelphia: Elsevier Saunders.

17. Ten Tusscher, K.H., R. Hren, and A.V. Panfilov, *Organization of ventricular fibrillation in the human heart.* Circ Res, 2007. **100**(12): p. e87-101.

18. Vandersickel, N., et al., *Perpetuation of torsade de pointes in heterogeneous hearts: competing foci or re-entry?* The Journal of Physiology, 2016. **594**(23): p. 6865-6878.

19. Sahli Costabal, F., D.E. Hurtado, and E. Kuhl, *Generating Purkinje networks in the human heart.* Journal of Biomechanics, 2016. **49**(12): p. 2455-2465.

20. Xie, F., et al., *A simulation study of the effects of cardiac anatomy in ventricular fibrillation.* J Clin Invest, 2004. **113**(5): p. 686-93.

21. Sadrieh, A., et al., *Multiscale cardiac modelling reveals the origins of notched T waves in long QT syndrome type 2.* Nat Commun, 2014. **5**: p. 5069.

22. O'Hara, T., et al., *Simulation of the undiseased human cardiac ventricular action potential: model formulation and experimental validation.* PLoS Comput Biol, 2011. **7**(5): p. e1002061.

23. Li, G.R., et al., *Transmembrane ICa contributes to rate-dependent changes of action potentials in human ventricular myocytes.* Am J Physiol, 1999. **276**(1 Pt 2): p. H98-H106.

24. Stewart, P., et al., *Mathematical models of the electrical action potential of Purkinje fibre cells.* Philos Trans A Math Phys Eng Sci, 2009. **367**(1896): p. 2225-55.

25. Vijayakumar, R., et al., *Electrophysiologic Substrate in Congenital Long QT Syndrome: Noninvasive Mapping With Electrocardiographic Imaging (ECGI).* Circulation, 2014. **130**(22): p. 1936-1943.

26. Liu, G.X., et al., *Differential conditions for early after-depolarizations and triggered activity in cardiomyocytes derived from transgenic LQT1 and LQT2 rabbits.* J Physiol, 2012. **590**(Pt 5): p. 1171-80.

27. Silva, J. and Y. Rudy, *Subunit interaction determines IKs participation in cardiac repolarization and repolarization reserve.* Circulation, 2005. **112**(10): p. 1384-91.

28. Qu, Z., et al., *Early afterdepolarizations in cardiac myocytes: beyond reduced repolarization reserve.* Cardiovascular Research, 2013. **99**(1): p. 6-15.

29. Madhvani, R.V., et al., *Targeting the late component of the cardiac L-type Ca2+ current to suppress early afterdepolarizations.* Journal of General Physiology, 2015. **145**(5): p. 395-404.

30. Huang, X., et al., *Spontaneous initiation of premature ventricular complexes and arrhythmias in type 2 long QT syndrome.* American Journal of Physiology - Heart and Circulatory Physiology, 2016. **311**(6): p. H1470-H1484.

31. Engel, T.R., S.G. Meister, and W.S. Frankl, *The "R-on-T" Phenomenon: An Update and Critical Review.* Annals of Internal Medicine, 1978. **88**(2): p. 221-225.

32. Liu, W., et al., *Mechanisms linking T-wave alternans to spontaneous initiation of ventricular arrhythmias in rabbit models of long QT syndrome.* The Journal of Physiology, 2018. **596**(8): p. 1341-55.

33. Teplenin, A.S., et al., *Paradoxical Onset of Arrhythmic Waves from Depolarized Areas in Cardiac Tissue Due to Curvature-Dependent Instability.* Physical Review X, 2018. **8**(2): p. 021077.

34. Liu, J. and K.R. Laurita, *The mechanism of pause-induced torsade de pointes in long QT syndrome.* J Cardiovasc Electrophysiol, 2005. **16**(9): p. 981-7.

35. Maruyama, M., et al., *Genesis of phase 3 early afterdepolarizations and triggered activity in acquired long-QT syndrome.* Circ Arrhythm Electrophysiol, 2011. **4**(1): p. 103-11.

36. Kim, T.Y., et al., *Complex excitation dynamics underlie polymorphic ventricular tachycardia in a transgenic rabbit model of long QT syndrome type 1.* Heart Rhythm, 2015. **12**(1): p. 220-8.

37. Waldo, A.L. and A.L. Wit, *Mechanisms of cardiac arrhythmias.* Lancet, 1993. **341**(8854): p. 1189-93.

38. Qu, Z. and J.N. Weiss, *Mechanisms of Ventricular Arrhythmias: From Molecular Fluctuations to Electrical Turbulence.* Annual Review of Physiology, 2015. **77**(1): p. 29-55.

39. Bai, J., et al., *Pro-arrhythmogenic effects of CACNA1C G1911R mutation in human ventricular tachycardia: insights from cardiac multi-scale models.* Scientific Reports, 2016. **6**: p. 31262.

40. Yang, P.-C., et al., *A multiscale computational modelling approach predicts mechanisms of female sex risk in the setting of arousal-induced arrhythmias.* The Journal of Physiology, 2017. **595**(14): p. 4695-4723.

41. Dutta, S., et al., *Early afterdepolarizations promote transmural reentry in ischemic human ventricles with reduced repolarization reserve.* Progress in Biophysics and Molecular Biology, 2016. **120**(1–3): p. 236-248.

42. Neal Kay, G., et al., *Torsade de pointes: The long-short initiating sequence and other clinical features: observations in 32 patients.* Journal of the American College of Cardiology, 1983. **2**(5): p. 806-817.

43. Schwartz, P.J., L. Crotti, and R. Insolia, *Long-QT syndrome: from genetics to management.* Circ Arrhythm Electrophysiol, 2012. **5**(4): p. 868-77.

44. Qu, Z. and D. Chung, *Mechanisms and determinants of ultralong action potential duration and slow rate-dependence in cardiac myocytes.* PLoS One, 2012. **7**(8): p. e43587.

45. Varshneya, M., R.A. Devenyi, and E.A. Sobie, *Slow Delayed Rectifier Current Protects Ventricular Myocytes From Arrhythmic Dynamics Across Multiple Species.* Circulation: Arrhythmia and Electrophysiology, 2018. **11**(10): p. e006558.

46. Bourgonje, V.J.A., et al., *Combined Na+/Ca2+ Exchanger and L-Type Calcium Channel Block as a Potential Strategy to Suppress Arrhythmias and Maintain Ventricular Function.* Circulation: Arrhythmia and Electrophysiology, 2013. **6**(2): p. 371-379.

47. Immanuel, S.A., et al., *T-wave morphology can distinguish healthy controls from LQTS patients.* Physiological Measurement, 2016. **37**(9): p. 1456-1473.

48. Britton, O.J., et al., *Experimentally calibrated population of models predicts and explains intersubject variability in cardiac cellular electrophysiology.* Proc Natl Acad Sci U S A, 2013. **110**(23): p. E2098-105.

49. Ni, H., S. Morotti, and E. Grandi, *A Heart for Diversity: Simulating Variability in Cardiac Arrhythmia Research.* Frontiers in Physiology, 2018. **9**(958).

50. Sarkar, A.X., D.J. Christini, and E.A. Sobie, *Exploiting mathematical models to illuminate electrophysiological variability between individuals.* J Physiol, 2012. **590**(Pt 11): p. 2555-67.

Supplemental Information

Ventricular myocyte cell model

The base cell model used was the human ventricular myocyte model by O'Hara et al [1] with the endocardial control parameters. To address a well-known tissue propagation issue, the I_{Na} m-gate steady-state activation curve was left-shifted by 10 mV. To simulate the different congenital LQTS subtypes, the conductance of I_{Ks} or I_{Kr} was completely blocked in the case of LQT1 and LQT2 respectively, and the conductance of I_{NaL} was increased in LQT3. To simulate the bulk heterogeneity, the conductances of I_{Kr} in LQT1, I_{Ks} in LQT2, and I_{NaL} in LQT3 were adjusted to create a repolarization gradient. The $I_{Ca,L}$ steady-state activation and inactivation curves were taken from either the original O'Hara et al formulation or another human measurement from Li et al [2], parameterized in the form of $\mathrm{d}_\infty = 1/(1 + \exp\left[\frac{-(V+\mathrm{d}_{\infty,\mathrm{V}})}{\mathrm{d}_{\infty,\mathrm{k}}}\right])$ and $\mathrm{f}_\infty = 1/(1 + \exp\left[\frac{V+\mathrm{f}_{\infty,\mathrm{V}}}{\mathrm{f}_{\infty,\mathrm{k}}}\right])$.

The parameters for LQT1 were: G_{Ks} = 0 mS/μF, $G_{Kr,1}$ = 0.025 mS/μF, $G_{Kr,2}$ = 0.017 mS/μF, $d_{\infty,V}$ = 3.940 mV, $d_{\infty,k}$ = 4.230 mV, $f_{\infty,V}$ = 19.58 mV, $f_{\infty,k}$ = 3.696 mV.

The parameters for LQT2 were: G_{Kr} = 0 mS/μF, $G_{Ks,1}$ = 0.050 mS/μF, $G_{Ks,2}$ = 0.030 mS/μF, $d_{\infty,V}$ = 4.8 mV, $d_{\infty,k}$ = 6.2 mV, $f_{\infty,V}$ = 28.5 mV, $f_{\infty,k}$ = 7.8 mV.

The parameters for LQT3 were: $G_{NaL,1}$ = 0.050 mS/μF, $G_{NaL,2}$ = 0.066 mS/μF, $d_{\infty,V}$ = 4.8 mV, $d_{\infty,k}$ = 6.2 mV, $f_{\infty,V}$ = 28.5 mV, $f_{\infty,k}$ = 7.8 mV.

Anatomical ventricle modeling

The anatomical geometry of the ventricle model and fiber direction field were obtained from previous work by Ten Tusscher et al [3], consisting of ~1.7 million voxels of 0.5 mm size, incorporating a Purkinje network (Fig.5-S1).

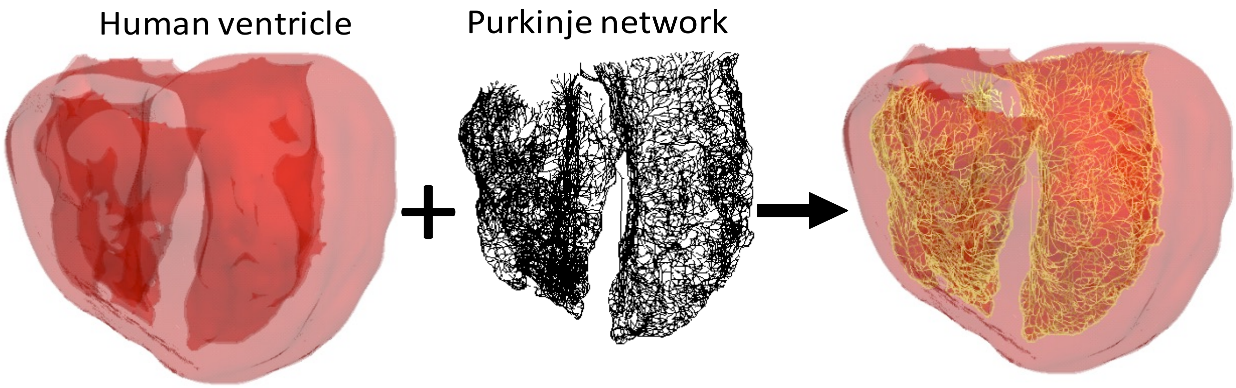

Figure 5-S1. Human ventricle myocardium model coupled with the Purkinje network model. The Purkinje network starts at the simulated AV node where sinus beats are initiated, is grown onto the endocardial surface.

The partial differential equation governing membrane voltage *V* in the anatomical model is:

$$\frac{\partial V}{\partial t} = -I_{ion}/C_m + \sum_i \sum_j \frac{\partial}{\partial x_i} D_{ij} \frac{\partial}{\partial x_j} V$$

where C_m = 1 μF/cm^2 is the membrane capacitance, I_{ion} is the total ionic currents of the cell, and D_{ij} is the 3D conductivity tensor describing the anisotropy of voltage propagation corresponding to the fiber direction field, with *i,j* as indices for the 3 cartesian dimensions. Numerical integration was performed using with a finite difference forward Euler method and an operating splitting and time adaptive algorithm [4] with the time step (Δt) varying between 0.01 ms and 0.1 ms. A bulk heterogeneity in the RV was set using the parameters described above (Fig.5-S2).

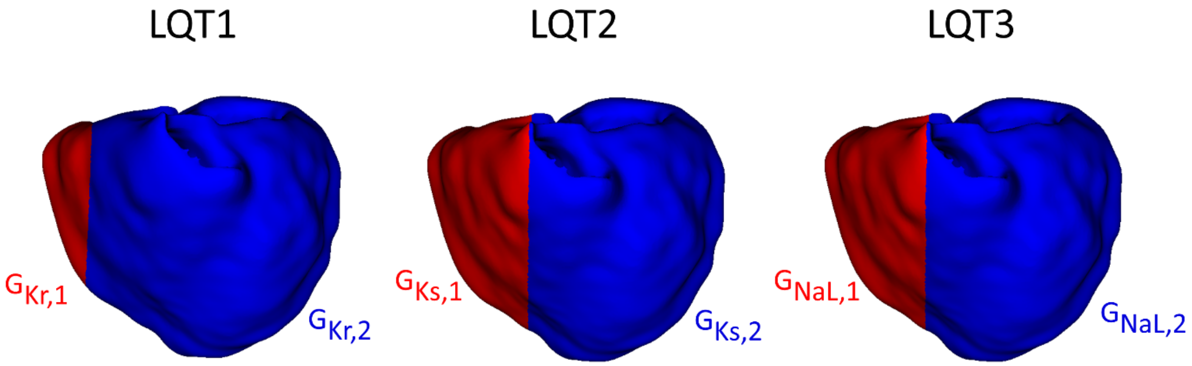

Figure 5-S2. Bulk heterogeneities for each LQTS subtype. The spatial heterogeneity is created using two different conductance regions in G_{Kr} for LQT1, G_{Ks} for LQT2, and G_{NaL} for LQT3. All other parameters are homogeneous across the ventricle for each subtype.

Purkinje network modeling

We tailored our model to provide for a physiological activation sequence, ECG properties, and robust forward and retrograde conduction at the Purkinje-myocyte junctions (PMJs). The human Purkinje action potential model by Stewart et al [5] was used for our Purkinje network. The Purkinje network was modeled as a connected set of 1D cables with the diffusion constant set to result in a conduction velocity of ~4 m/s. The primary tree of the Purkinje network began at a straight His-bundle which then branched into the right bundle branch and the left bundle branch (including the left anterior and posterior fascicles). An AV-node delay was simulated by a very slow diffusion constant at the beginning of the His-bundle. The rest of the network was generated using a fractal surface mapping method developed by Sahli Costabal et al [6], mapped to the RV and LV endocardial surfaces. The terminal Purkinje fibers were allowed to form loops as consistent with experimental data [7, 8]. The final full structure (Fig.5-S1) consisted of 58,705 computational cell nodes with Δx = 0.5 mm. A PMJ was created between each Purkinje cell node to the closest ventricular myocyte cell node, modeled as a passive Ohm's law conductance. The relative capacitance ratio between the Purkinje and ventricular myocyte computational nodes was set to 1.0 which allowed for robust forward and retrograde conduction across the PMJ.

The differential equation governing Purkinje cell voltage V_P is:

$$\frac{dV_P}{dt} = -\frac{I_{ion,P}}{C_{m,P}} + \sum_i D_P \frac{V_i - V_p}{\Delta x^2} + I_{PMJ}/C_{m,P}$$

with

$$I_{PMJ} = \begin{cases} G_{PMJ}(V - V_P), & \text{cells with a PMJ} \\ 0, & \text{cells without a PMJ} \end{cases}$$

where $C_{m,Purkinje}$ is the capacitance of the Purkinje cell node, $I_{ion,Purkinje}$ is the total ionic currents of the Purkinje cell, $D_{Purkinje}$ = 0.0300 cm^2/ms is the diffusion constant, G_{PMJ} = 0.05 mS/µF. The ventricular myocyte that belongs to the PMJ also receives an equal and opposite I_{PMJ}. Numerical integration was performed using a finite difference forward Euler method with operator splitting and a fixed time step of Δt = 0.01 ms.

1D and 2D tissue models

The partial differential equation governing voltage for the 1D cable is

$$\frac{\partial V}{\partial t} = -I_{ion}/C_m + D\frac{\partial^2 V}{\partial x^2}$$

where V is the membrane voltage, C_m=1 μF/cm^2 is the membrane capacitance, D = 0.0005 cm^2/ms is the diffusion constant (proportional to gap junction conductance), and Δx = 0.15 mm.

For 2D tissue, the equation for voltage is

$$\frac{\partial V}{\partial t} = -I_{ion}/C_m + D(\frac{\partial^2 V}{\partial x^2} + \frac{\partial^2 V}{\partial y^2})$$

where V is the membrane voltage, C_m=1 μF/cm^2 is the membrane capacitance, D = 0.0001 cm^2/ms is the diffusion constant (proportional to gap junction conductance), and Δx = 0.15 mm.

Numerical integration was performed using a finite difference forward Euler method and an operating splitting and time adaptive algorithm with the time step (Δt) varying between 0.01 ms and 0.1 ms.

Pseudo-ECG computation

Pseudo ECGs were computed using the following formula [9, 10]

$$\boldsymbol{\Phi}_{\boldsymbol{e}}(x', y', z') \sim \iiint (-\boldsymbol{\nabla} V) \cdot \left[\boldsymbol{\nabla}\frac{1}{r}\right] dxdydz$$

where $\boldsymbol{\nabla} V$ is the spatial gradient of the membrane voltage and $r = [(x - x')^2 + (y - y)^2 + (y - y')^2]^{1/2}$ represents the distance from a source point (*x,y,z*) to a field point (*x',y',z'*), with the integral performed over all heart cells.

For the human ventricle simulations, we calculated a pseudo-ECG for V1 to V6 (see Fig.5-S3 for lead placement). A bandpass filter of 0.1-150 Hz was applied to each recording.

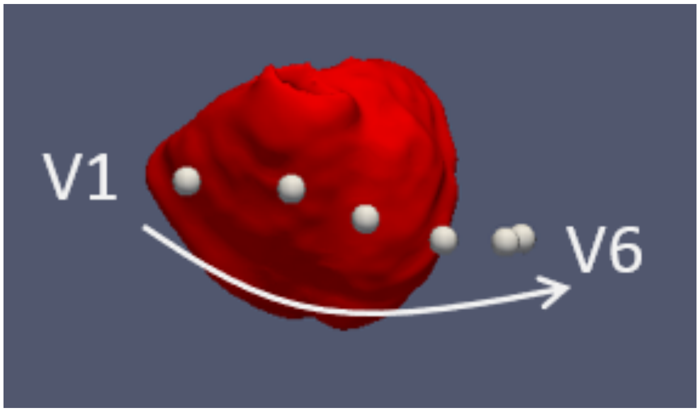

Figure 5-S3. Lead placement for pseudo-ECG computation.

Visualization methods

Single cell, 1D, and 2D results were visualized in Python using the Matplotlib library [11]. ECGs were also plotted in Python using the Matplotlib library. Anatomical heart results were visualized in 3D using the VisIt software tool (Lawrence Livermore National Laboratory) [12].

Online Movie Captions

Online Movie 5-1. Spontaneous initiation of arrhythmia in LQT2. Three view movie including ventricle voltage maps (left), wavefronts (colored red, middle), and Purkinje network voltage maps (right). The ECG strip and time marker are shown below. P_{Ca} ramp protocol simulation with $P_{Ca,H}$ = 2.8 μm/s (corresponding to the 6th ECG trace in Fig.5-2).

Online Movie 5-2. 2D simulation of spontaneous focal arrhythmias from the R-from-T mechanism. Voltage map from the 2D tissue corresponding to Fig.5-3D.

Online Movie 5-3. 2D simulation of spontaneous reentrant arrhythmias from the R-from-T mechanism. Voltage map from the 2D tissue corresponding to Fig.5-3E.

Online Movie 5-4. Spontaneous initiation of arrhythmia in LQT3. Three view movie including ventricle voltage maps (left), wavefronts (colored red, middle), and Purkinje network voltage maps (right). The ECG strip and time marker are shown below. P_{Ca} ramp protocol simulation with $P_{Ca,H}$ = 3.2 μm/s (corresponding to the 6th ECG trace in Fig.5-4).

Online Movie 5-5. Spontaneous initiation of arrhythmia in LQT1. Three view movie including ventricle voltage maps (left), wavefronts (colored red, middle), and Purkinje network voltage maps (right). The ECG strip and time marker are shown below. P_{Ca} ramp protocol simulation with $P_{Ca,H}$ = 3.1 μm/s at 60 bpm (corresponding to the 4th ECG trace in Fig.5-5).

References

1. O'Hara T, Virág L, Varró A, Rudy Y. Simulation of the undiseased human cardiac ventricular action potential: model formulation and experimental validation. PLoS Comput Biol. 2011;7(5):e1002061.

2. Li GR, Yang B, Feng J, Bosch RF, Carrier M, Nattel S. Transmembrane ICa contributes to rate-dependent changes of action potentials in human ventricular myocytes. Am J Physiol. 1999;276(1 Pt 2):H98-H106.

3. Ten Tusscher KH, Mourad A, Nash MP, et al. Organization of ventricular fibrillation in the human heart: experiments and models. Exp Physiol. 2009;94(5):553-62.

4. Qu Z, Garfinkel A, An advanced algorithm for solving partial differential equation in cardiac conduction. IEEE Transactions on Biomedical Engineering, vol. 46, no. 9, pp. 1166-1168, Sept. 1999.

5. Stewart P, Aslanidi OV, Noble D, Noble PJ, Boyett MR, Zhang H. Mathematical models of the electrical action potential of Purkinje fibre cells. Philos Trans A Math Phys Eng Sci. 2009;367(1896):2225-55.

6. Sahli Costabal F, Hurtado DE, Kuhl E. Generating Purkinje networks in the human heart. J Biomech. 2016;49(12):2455-65.

7. De almeida MC, Lopes F, Fontes P, Barra F, Guimaraes R, Vilhena V. Ungulates heart model: a study of the Purkinje network using India ink injection, transparent specimens and computer tomography. Anat Sci Int. 2015;90(4):240-50.

8. Ijiri T, Ashihara T, Yamaguchi T, et al. A procedural method for modeling the purkinje fibers of the heart. J Physiol Sci. 2008;58(7):481-6.

9. Xie F, Qu Z, Yang J, Baher A, Weiss JN and Garfinkel A. A simulation study of the effects of cardiac anatomy in ventricular fibrillation. *J Clin Invest*. 2004;113:686-93.

10. Sadrieh A, Domanski L, Pitt-Francis J, Mann SA, Hodkinson EC, Ng CA, Perry MD, Taylor JA, Gavaghan D, Subbiah RN, Vandenberg JI and Hill AP. Multiscale cardiac modelling reveals the origins of notched T waves in long QT syndrome type 2. *Nature communications*. 2014;5:5069.

11. Hunter JD. Matplotlib: A 2D Graphics Environment. Computing in Science & Engineering. 2007;9(3):90-95. doi:10.1109/mcse.2007.55

12. Childs H, Brugger E, Whitlock B, et al. VisIt: An End-User Tool For Visualizing and Analyzing Very Large Data. High Performance Visualization Chapman & Hall/CRC Computational Science. 2012. doi:10.1201/b12985-21

Chapter 6: Conclusion

Cardiac arrhythmias and sudden cardiac death remain a leading cause of death in the U.S. and worldwide, with the over 80% of SCD caused by ventricular tachyarrhythmias. Although our understanding of spiral wave dynamics and arrhythmia maintenance and transitions mechanisms have greatly improved over the last few decades, the implantable cardioverter-defibrillator still remains the most reliable intervention for the prevention of SCD in those without a clearly identifiable ablation target, despite the adverse side effects and cost inefficiency. The basic principles behind the ICD are virtually unchanged from when the phenomenon of defibrillation was discovered over 100 years ago, and it remains a purely reactive intervention to terminate existing arrhythmias, crudely resetting the entire heart before too much damage is done. The ideal goal of arrhythmia therapy is to prevent the arrhythmia from initiating in the first place instead. The work presented in this dissertation represents our efforts to better understand the mechanisms underpinning the initiation process in spontaneous arrhythmias, at multiple scales of cardiac electrophysiology, in order to provide a basis for future anti-arrhythmic strategies.

Arrhythmogenic triggers and substrates: beyond the traditional paradigm

The trigger and substrate paradigm of reentrant arrhythmia initiation has been a useful framework for evaluating arrhythmia risk under different conditions. However, it has not always led to the correct conclusion, such as the failure of sodium channel blockers in CAST with increased mortality despite a reduction in triggers. Therefore, it is important to examine both triggers and substrates in multiple contexts and to also evaluate them as non-independent entities to accurately determine their arrhythmogenic potential.

In Chapter 2, we revealed a novel understanding of the threshold for DAD-mediated triggered activity. In normokalemic conditions, the voltage threshold for TA was observed to be at the sodium channel threshold around -60 mV as expected. In hypokalemia however, not only the voltage threshold but also the calcium release threshold were found to be much lower. Thus, despite having the resting membrane potential be hyperpolarized and further away from the sodium channel threshold, in hypokalemia it was easier to elicit a TA. Using non-linear dynamics and nullcline analysis, we demonstrated that this dynamical threshold arose from the interplay between I_{K1} and I_{NCX} with a “cusp-catastrophe” determining both the calcium and voltage threshold for TA. This effect had previously been masked because it only manifests if the system is given enough time to approach steady-state. While most stimulation pacing experiments are performed with very short stimuli, the relatively slow Ca^{2+} release over hundreds of milliseconds during a DAD allows the phenomenon to occur, thus highlighting the importance to study arrhythmia triggers in a broad context.

Chapter 3 also investigates the factors that influence the ability for DADs to generate triggers at the cardiac tissue level. In this study, we experimentally measured multiple DAD properties including DAD amplitude, width, and latency at different calcium loads using patch clamp and calcium imaging. These properties were then characterized and the used as inputs into a cardiac tissue model, and the different factors of amplitude, width, and latency distribution were systematically analyzed in simulation to determine their individual effects on TA generation. We found that among all the factors, latency distribution and calcium load were by far the most important, and that surprisingly gap junction conductance played a relatively minor role, pinpointing the critical factors needed for DADs to produce triggers in tissue.

Chapter 4, on the other hand, investigated whether DADs could also play the role of an arrhythmogenic substrate instead. DADs until now have traditionally been considered only as potential triggers in arrhythmogenesis, with the possibility of causing focal arrhythmias with repetitive firings or reentry if it encountered a different appropriate substrate. To this end, previous work including ours in Chapter 2 focused mainly on whether the DADs would be sufficiently large enough, i.e. super-threshold, to trigger an AP. In this chapter, we demonstrated instead that sub-threshold DADs still can play an important role, acting as an arrhythmogenic substrate due to the partial inactivation of sodium channels when the membrane voltage is raised to near but under -60 mV. When an external trigger PVC encounters a region of subthreshold DADs with a certain coupling interval, they can cause unidirectional conduction block and initiate reentry.

This study then takes this concept one step further: since super-threshold DADs can produce triggers and sub-threshold DADs can act as a substrate, could DADs act as both trigger and substrate simultaneously? Indeed, we demonstrate that a region of random DADs with no external triggers can spontaneous generate a reentrant arrhythmia by itself, a phenomenon that is exacerbated with sodium channel blockade. We then relate this fact to the paradoxical results of CAST, where while sodium channel blockers can convert benign PVCs into dangerous reentry by changing super-threshold DADs into a sub-threshold DAD substrate. This chapter adds an important conceptually novel contribution to the field, where the arrhythmogenic trigger and substrate can simultaneously both arise from the same source, and therefore must be treated together instead of independently.

Finally, in Chapter 5 we used whole heart modeling to investigate arrhythmogenesis in different genotypes of LQTS. We found that while different subtypes of LQTS can manifest with different ECG patterns before PVT, they all initiated arrhythmias through a common mechanism which we call “R-from-T”. We highlight the differences between the classical explanation of LQTS arrhythmogenesis which we call “R-to-T” in which the R-wave trigger and T-wave function substrate randomly meet as consistent with the traditional paradigm, and this novel R-from-T mechanism where the R-wave arises from the T-wave itself, and can immediately evolve into a focal or reentrant arrhythmia without the need for an additional substrate for reentry. The R-from-T excitation itself is caused by the same instability as the subsequent arrhythmias, thus can be considered as just the shortest possible run of a PVT that self-terminates after a single rotation. In this sense, the traditional notions of a distinct trigger and substrate are blurred with no clear distinction in the R-from-T mechanism and cannot be targeted separately.

Improved mechanistic understanding informs future anti-arrhythmic therapy

Preventing arrhythmogenesis will always be a preferred strategy if possible compared to terminating existing arrhythmias with an ICD after the fact. Our work here demonstrates the power of computational modeling used in conjunction with experimental validation to elucidate the conditions and mechanisms governing arrhythmogenesis in DAD-mediated arrhythmias and LQTS. With this new understanding, we are able to identify the critical factors required for arrhythmia initiation and use this information to propose new anti-arrhythmic targets to pursue. In the case of DADs, it is clear that suppressing super-threshold DAD triggers is insufficient, and the formation of Ca^{2+} waves themselves must be targeted to avoid the potential arrhythmogenic effect of sub-threshold DADs as well. For LQTS, understanding that the common R-from-T mechanism applies across different genotypes allows us to devise a unified therapeutic strategy for arrhythmia prevention in LQTS by targeting critical $I_{Ca,L}$ properties. Without this framework, this strategy would be otherwise unintuitive as we propose treating an I_{Ks}, an I_{Kr}, and an I_{NaL} mutation all using a single intervention in $I_{Ca,L}$ window current. In this manner, the novel mechanistic insights obtained from these studies inform the development of future anti-arrhythmic therapies.